

CO($J = 1-0$) Observations toward the Filamentary Cloud in the Galactic Region of $153^{\circ}60 \leq l \leq 156^{\circ}50$ and $1^{\circ}85 \leq b \leq 3^{\circ}50$

WEIHUA GUO,^{1,2} XUEPENG CHEN,^{1,2} JIANCHENG FENG,^{1,2} LI SUN,^{1,2} SHIYU ZHANG,^{1,2} CHEN WANG,¹ YANG SU,^{1,2} YAN SUN,^{1,2} QINGZENG YAN,¹ SHAOBO ZHANG,¹ XIN ZHOU,¹ MIAOMIAO ZHANG,¹ MIN FANG,¹ AND JI YANG^{1,2}

¹*Purple Mountain Observatory and Key Laboratory of Radio Astronomy, Chinese Academy of Sciences, 10 Yuanhua Road, Nanjing 210034, China*

²*School of Astronomy and Space Science, University of Science and Technology of China, Hefei, Anhui 230026, China*

ABSTRACT

We present observations of $J=1-0$ transition lines of ^{12}CO , ^{13}CO , and C^{18}O towards the Galactic region of $153^{\circ}60 \leq l \leq 156^{\circ}50$ and $1^{\circ}85 \leq b \leq 3^{\circ}50$, using the Purple Mountain Observatory (PMO) 13.7 m millimeter telescope. Based on the ^{13}CO data, one main filament and five sub-filaments are found together as a network structure in the velocity interval of $[-42.5, -30.0] \text{ km s}^{-1}$. The kinematic distance of this molecular cloud (MC) is estimated to be $\sim 4.5 \text{ kpc}$. The median length, width, excitation temperature, line mass of these filaments are $\sim 49 \text{ pc}$, $\sim 2.9 \text{ pc}$, $\sim 8.9 \text{ K}$, and $\sim 39 M_{\odot} \text{ pc}^{-1}$, respectively. The velocity structures along these filaments exhibit oscillatory patterns, which are likely caused by the fragmentation or accretion process along these filaments. The maximum accretion rate is estimated to be as high as $\sim 700 M_{\odot} \text{ pc}^{-1}$. A total of ~ 162 ^{13}CO clumps and ~ 103 young stellar objects (YSOs) are identified in this region. Most of the clumps are in gravitationally bound states. Three H II regions (G154.359+2.606, SH2-211, SH2-212) are found to be located in the apexes of the filaments. Intense star forming activities are found along the entire filamentary cloud. The observed results may help us to better understand the link between filaments and massive star formation.

Keywords: Molecular clouds(1072) — Interstellar filaments(842) — Star forming regions(1565) — Young stellar objects(1834)

1. INTRODUCTION

Surveys at multi-wavelengths, e.g., infrared surveys (André et al. 2010, 2014), high-resolution HI surveys (Soler et al. 2020), and CO surveys (Colombo et al. 2021; Yuan et al. 2021), have revealed that filamentary structures are ubiquitous in cold Galactic interstellar medium (ISM). The filaments are found to have lengths ranging from 0.1 pc to 1 kpc, containing gas mass of $\sim 10^3 - 10^5 M_{\odot}$ (Ragan et al. 2014; Hacar et al. 2018; Syed et al. 2021). As part of the ISM cycle, dense molecular filament plays a key role as it connects several important processes, such as the compression of diffuse gas, the fragmentation of cloud structures, and the formation of dense cores. For example, about 75% pre- and proto-stellar cores are found to be located in filaments in the *Herschel* Gould Belt Survey (e.g., André et al. 2014; Könyves et al. 2015). Large-scale filaments containing dense molecular gas appear to form massive stars and clusters, e.g., Nessie (Jackson et al. 2010, 2019; Mattern et al. 2018), Orion (Bally 1981; Johnstone & Bally 1999; Tatematsu et al. 2008), California (Lada et al. 2009, 2017; Guo et al. 2021), and NGC 6334 (Russeil et al. 2013; Fukui et al. 2018), though the relevant mechanisms are still in study. Motte et al. (2018) suggested an evolutionary picture for the formation of high-mass stars, which involves scenarios of a global hierarchical collapse and clump-fed accretion. A typical example is the DR21 ridge, the most massive cloud structure in the Cygnus-X region (e.g., Schneider et al. 2010). Compared to the Taurus filament B211/B213 (Palmeirim et al. 2013), it has a more spherical/elliptical geometry with a few sub-filaments connected to the hub ridge. The mass-flows transported along sub-filaments toward the hub ridge are considered to account for the mass growth of the massive clumps and cores therein (Hennemann et al. 2012).

The observations toward other filamentary clouds, e.g., Monoceros R2 (Treviño-Morales et al. 2019), G22 (Yuan et al. 2018), and W33 (Liu et al. 2021), support this scenario. In the hub ridges, with the material convergence, the mass accumulates and density increases, mini-starburst activities, with $\Sigma_{\text{SFR}} > 1 M_{\odot} \text{yr}^{-1} \text{kpc}^{-2}$ and $\Sigma_{M_{\text{gas}}} > 100 M_{\odot} \text{pc}^{-2}$ (Nguyen-Luong et al. 2016), can even take place. The filaments IRDC G035.39–00.33 (Nguyen Luong et al. 2011) and W43-MM1 ridge (Louvet et al. 2014) were found to have a SFE of $\sim 15\%$ within an area of $\sim 8 \text{pc}^2$ and a SFE of $\sim 6\%$ within an area of $\sim 8 \text{pc}^3$, respectively. Thus the two regions were suggested to form starburst clusters.

Investigating the multiscale kinematics will provide crucial clues to understand the relation between filamentary structures and high-mass star formation. It is necessary to search for more filamentary clouds to reveal their gas dynamics in terms of filaments fragmentation, cores accretion, high-mass star formation. The Milky Way Imaging Scroll Painting (MWISP) project¹ is an unbiased, high sensitivity CO multi-line survey towards the northern Galactic plane (Su et al. 2019; Sun et al. 2021), which provides us a good opportunity to study large-scale filamentary clouds (e.g., Guo et al. 2021; Yuan et al. 2021). In this work, we present the observations of the three CO isotope lines towards the Galactic region of $153^{\circ}6 \leq l \leq 156^{\circ}5$ and $1^{\circ}85 \leq b \leq 3^{\circ}5$. The observations are described in Section 2. Section 3 presents the main results including the basic physical parameters of the MC, the process of the discrimination of the filaments, the physical properties and kinematic structures of the filaments, and the star formation activities therein. Section 4 discuss these results and a summary is made in Section 5.

2. OBSERVATIONS AND DATA REDUCTION

As part of the MWISP, the observations were performed with the PMO 13.7 m millimeter telescope from April 2012 to February 2017. The three isotope emission lines of ^{12}CO at 115.271 GHz, ^{13}CO at 110.201 GHz, and C^{18}O at 109.782 GHz were simultaneously observed with the 3×3 beams Superconducting Spectroscopic Array Receiver (SSAR) system in the sideband separation mode (Shan et al. 2012). The ^{12}CO was at the upper sideband (USB), and ^{13}CO and C^{18}O were at the lower sideband (LSB). Typical system temperatures were around $\sim 270 \text{K}$ for the USB and around 175K for the LSB, respectively.

In the position-switch On-The-Fly (OTF) mode, the telescope scanned the sky along both the longitude and latitude directions at a constant rate of $50'' \text{s}^{-1}$. The half-power beamwidth (HPBW) is approximately $52''$ at 115.2 GHz and $55''$ at 110.2 GHz. The beam efficiencies (η_{MB}) are 44% for 115.2 GHz and 48% for 110.2 GHz, respectively. The pointing uncertainty is approximately within $5''$. The total 1GHz bandwidth is separated into 16384 channels, resulting in a resolution of 61 kHz in frequency, which is corresponding to $\sim 0.16 \text{km s}^{-1}$ for ^{12}CO , $\sim 0.17 \text{km s}^{-1}$ for ^{13}CO and C^{18}O in velocity, respectively. Velocities were all given with respect to the local standard of rest (LSR). The rms noises levels are $\sim 0.5 \text{K}$ for ^{12}CO , and $\sim 0.3 \text{K}$ for ^{13}CO and C^{18}O , respectively. More information about the telescope can be found in the telescope status report². All data were reduced by the dedicated pipelines based on C, IDL, and Python by MWISP working group³ and the GILDAS/CLASS package by IRAM (Pety 2005). After removing bad channels and correcting the first order (linear) base line fitting, the data were regridded into the standard FITS files with a pixel size of $30'' \times 30''$ (approximately half of the beam size).

3. RESULTS

3.1. Filamentary Network Cloud

As shown in Figure 1, we construct the Longitude-Velocity (LV) diagram by summing the emission along the latitude interval of $[1^{\circ}85, 3^{\circ}5]$. The CO emission mainly appears in the velocity interval of $[-45, 5] \text{km s}^{-1}$. According to the analysis in Dame et al. (2001), the emission in $[-15, 5] \text{km s}^{-1}$ is generally attributed to the Local arm. Xiong et al. (2017) partially presented the MWISP CO data analysis in this interval (towards the region of $147^{\circ}75 \leq l \leq 152^{\circ}0, 1^{\circ}5 \leq b \leq 5^{\circ}25$). In this work, we focus on the CO emission in the velocity interval of $[-42.5, -30.0] \text{km s}^{-1}$. The zoom-in LV diagram shows that the emission could be further divided into eastern⁴ ($l \sim [155^{\circ}0, 156^{\circ}5]$) and western ($l \sim [154^{\circ}0, 155^{\circ}0]$) regions.

Figure 2 shows the velocity-integrated intensity image for the three CO lines. For ^{12}CO and ^{13}CO , to obtain clear maps, we use pixels with emission above 3σ and at least 3 continuous channels for integration. For C^{18}O , in order to retain as many valid signals as possible, we apply for the DBSCAN algorithm (connectivity 1 and MinPts 4, see Yan

¹ <http://www.radioast.nsd.cn/mwisp.php>

² <http://www.radioast.csdb.cn/zhuangtaibaogao.php>

³ <http://www.iram.fr/IRAMFR/GILDAS>

⁴ All the directions mentioned in this work are in the Galactic coordinate system.

Table 1. associated H II regions and IRAS sources

Name	l ($^{\circ}$)	b ($^{\circ}$)	Velocity (km s^{-1})	references for association
G154.346+2.60	154.346	2.606	-43.60 ± 24.00 ^a	Anderson et al. (2015)
SH2-211	154.661	2.452	-35.22 ± 28.50 ^a -33.00 ^b	Balser et al. (2011) Pismis et al. (1991)
SH2-212	155.357	2.609	-43.95 ± 25.57 ^a -38.4 ^b -40.1 ± 1.0 ^c	Balser et al. (2011) Pismis et al. (1991) Lockman (1989)
IRAS04324+5102	154.397	2.548	-37.55	Yang et al. (2002)
IRAS04324+5106	154.347	2.606	-36.02 -37.3 ^d	Yang et al. (2002) Pirogov (1999)
IRAS04335+5110	154.414	2.774	-34.89	Yang et al. (2002)
IRAS04366+5022	155.331	2.596	-34.00	Yang et al. (2002)
IRAS04368+5021	155.367	2.607	\sim	Inoue et al. (2001)
IRAS04329+5045	154.650	2.435	\sim	Inoue et al. (2001)
IRAS04329+5047	154.637	2.445	-37.1 ^e -38.3 ^d	Snell et al. (1990) Pirogov (1999)

a: velocity of hydrogen radio recombination lines ($v_{\text{LSR,HRRLs}} \pm$ Full width at half height (FWHM)). b: $v_{\text{LSR,H}\alpha}$. c: $v_{\text{LSR,H109}\alpha}$. d: $v_{\text{LSR,HCN}(J=1-0)}$. e: $v_{\text{LSR,CO}}$

et al. 2020, for details) to make a mask. The parameters of cutoff threshold and the peak brightness temperature are selected as 1.5σ and $> 3\sigma$ to filter noise in this process. Then pixels within the mask greater than 2σ are used for integration. As shown in Figure 2, the three-color intensity image clearly shows the relative spatial distribution traced by the three isotope CO lines, respectively.

In the western region, the emission of ^{12}CO and ^{13}CO outlines a network structure. Compared with the relatively diffuse emission traced by ^{12}CO , the ^{13}CO emission shows the distinct skeletons of the network structure, while the C^{18}O emission is mainly concentrated at the main node structure. The peak intensity of the ^{12}CO emission appears at the position of $(l, b) \sim (154^{\circ}358, 2^{\circ}600)$. In the eastern region, two isolated filamentary structures are separately distributed up and down. The upper one extends about 1° along the direction from southwest to northeast with respect to the Galactic plane by an inclination angle of about 45° . The emission in the southwestern part seems brighter than the northeastern part. The lower one is roughly parallel to the Galactic plane.

Table 1 lists H II regions and IRAS sources associated with the MC. The association between the H II regions and the MC is based on the consistency of the velocities of the ionized gas and the CO gas. For IRAS sources, four of them are selected from the catalog of Yang et al. (2002). The rest three are selected from the analysis of previous studies (Inoue et al. 2001; Klein et al. 2005), e.g., according to correlation between the luminosities of IR and $\text{H}\alpha$, the IRAS04368+5021 and IRAS04329+5045 are identified to be associated with the H II regions of SH2-211 and SH2-212 respectively.

3.2. Distance of the cloud

In the second quadrant of the Milky Way, the systemic velocity (v_{LSR}) of molecular gas increases negatively from $\sim 0 \text{ km s}^{-1}$ to trace subsequently the Local arm, the Perseus Arm, the Outer Arm, and the Scutum-Centaurus Arm (Vallée 2008; Sun et al. 2015; Reid et al. 2019). Du et al. (2016, 2017) analyzed the MC structures in the region of $l \sim [100^{\circ}0, 150^{\circ}0]$, $b \sim [-3^{\circ}0, 5^{\circ}0]$, using the CO data from the MWISP survey. According to the tendency of LV map (see, e.g., Figure 5 in Du et al. 2016), the filamentary MC in this work is located in the Outer arm. According to previous

Table 2. Measured distances of the six selected positions.

NO.	l ($^{\circ}$)	b ($^{\circ}$)	v_{LSR} (km s^{-1})	distance (kpc)	probability	Arm
1	154.35	2.58	-35.1	4.50 ± 0.51	0.63	Out
2	154.48	2.49	-35.9	4.52 ± 0.51	0.68	Out
3	154.43	2.76	-33.8	4.48 ± 0.51	0.55	Out
4	154.44	2.87	-35.1	4.49 ± 0.51	0.60	Out
5	154.59	2.64	-35.2	4.50 ± 0.51	0.66	Out
6	154.84	2.43	-37.2	4.53 ± 0.51	0.74	Out
7	154.78	2.48	-35.5	4.51 ± 0.51	0.69	Out
8	154.77	2.81	-36.2	4.51 ± 0.51	0.68	Out
9	155.35	2.59	-36.6	4.50 ± 0.53	0.70	Out

optical observations of stars associated with the H II regions, the distance of IRAS04324 + 5106 was suggested to be ~ 6 kpc (Carpenter et al. 1993). The distance of SH2-212 was suggested to range from ~ 4.81 kpc to ~ 6.8 kpc (Moffat et al. 1979; Jose et al. 2011; Lim et al. 2015; Cantat-Gaudin & Anders 2020). For SH2-211, the spectroscopic distance was relatively uncertain, ranging from ~ 3 kpc to ~ 7.8 kpc (Chini & Wink 1984; Hunter & Massey 1990; Foster & Brunt 2015).

We try to estimate the distances using the Bayesian distance calculator provided by Reid et al. (2019). We select nine pixels with strong radiation and apply single Gaussian fits to the spectral lines to derive the peak velocities. The rotation model from Reid et al. (2019) is then applied to each coordinate and peak velocity to get the distance. The results are listed in Table 2. As shown in Figure 3, the position with strongest emission (named as “NO.1”) is found to have a higher combined probability (70%) to be associated with portion of the Outer arm at a distance of 4.51 ± 0.49 kpc than to be associated with the Perseus arm at 2.03 ± 0.34 kpc. The other eight positions go through the similar situation. The average distance is $\sim 4.50 \pm 0.51$ kpc. We therefor adopt 4.5 kpc as the distance of the filamentary cloud, which is comparable with the distance estimated in previous studies (see above).

3.3. Properties of the cloud

Assuming ^{12}CO is optically thick and the background temperature (T_{bg}) is 2.73 K, the excitation temperature (T_{ex}) could be calculated from the peak value of the main beam temperature of ^{12}CO ($T_{\text{mb,peak},^{12}\text{CO}}$) following the method of Garden et al. (1991). The formula is simplified as

$$T_{\text{ex}} = 5.532 \left[\log \left(1 + \frac{5.53}{T_{\text{mb,peak},^{12}\text{CO}} + 0.819} \right) \right]^{-1} \text{ (K)}. \quad (1)$$

The distribution of excitation temperature is shown in Figure 4. The value ranges from 3.1 to 26.4 K. The position of the peak value is spatially coincident with the H II region G154.346+02.606.

In the assumption of local thermodynamic equilibrium (LET) and equal T_{ex} of the isotopologue pair, the ^{13}CO column density ($N_{^{13}\text{CO}}$) can be estimated by

$$N_{^{13}\text{CO}} = 2.42 \times 10^{14} \cdot \frac{\int T_{\text{mb},^{13}\text{CO}} dv}{1 - \exp(-5.29/T_{\text{ex}})} \cdot \frac{\tau_{13}}{1 - e^{-\tau_{13}}}, \text{ where} \quad (2)$$

$$\tau_{13} = -\ln \left[1 - \frac{T_{\text{mb, peak}, ^{13}\text{CO}}}{5.29} \left(\left[e^{5.29/T_{\text{ex}}} - 1 \right]^{-1} - 0.164 \right)^{-1} \right] \quad (3)$$

As emission of the molecular cloud primarily occurs in regions with excitation temperatures greater than 5K, we set the excitation temperature that below 5K to 5K when estimating optical depth of ^{13}CO (τ_{13}). We get that the range of τ_{13} is 0.08 - 1.98.

Table 3. Properties of the cloud

Velocity interval (km s ⁻¹)	Distance (kpc)	Molecule Tracer	Area (arcmin ²)	$N(\text{H}_2)^a$ (10 ²¹ cm ⁻²)	$n(\text{H}_2)^a$ (cm ⁻³)	$M(\text{H}_2)^b$ (10 ⁴ M_\odot)
(1)	(2)	(3)	(4)	(5)	(6)	(7)
[-42.5, -30.0]	4.5	¹² CO	2347	2.85	25	11.7
		¹³ CO	506	3.53	68	2.96
		C ¹⁸ O	49	1.87	110	0.42

NOTE—a, mean value with weight of integrated intensity. b, the estimated values at the distance of 4.5 kpc.

The H₂ column density could be derived by multiplying the ¹³CO column density with the ratio of $N_{\text{H}_2}/N_{^{13}\text{CO}} \sim 7 \times 10^5$ (Frerking et al. 1982). For C¹⁸O is always thin, we use a similar but simpler method under the same assumption to derive the C¹⁸O column density:

$$N_{\text{C}^{18}\text{O}} = 2.24 \times 10^{14} \cdot \frac{(1 + 0.88/T_{\text{ex}}) \int T_{\text{mb},\text{C}^{18}\text{O}} dv}{1 - \exp(-5.27/T_{\text{ex}})}. \quad (4)$$

The H₂ column density could be derived by a conversion ratio of $N_{\text{H}_2}/N_{\text{C}^{18}\text{O}} \sim 7 \times 10^6$ (Castets & Langer 1995). The H₂ column density can also be estimated by multiplying the ¹²CO integrated intensity with the CO-to-H₂ conversion factor $X \sim 1.8 \times 10^{20} \text{ cm}^{-2} \text{ K}^{-1} \text{ km}^{-1} \text{ s}$ (Dame et al. 2001):

$$N_{\text{H}_2} = X \int T_{\text{mb},^{12}\text{CO}} dv. \quad (5)$$

Figure 5 shows the distributions of the derived H₂ column density. The volume density is obtained by dividing the column density by an equivalent radius, where the equivalent radius can be obtained if the emission area is assumed to be circle in shape. In the estimation process of the mass and volume density, a mean molecular weight with the value of 2.83 is adopted (Kauffmann et al. 2008). The projected emission area, column density, volume density and mass are listed in Table 3. The emission area of ¹²CO (2347 arcmin²) is much larger than that of ¹³CO (506 arcmin²) and C¹⁸O (49 arcmin²). The low-density molecular gas traced by ¹²CO occupies most of the total mass. In the following section 3.4, we focus on the ¹³CO emission as it better traces the filamentary skeletons.

3.4. Filaments

Generally, a filament is characterized by an elongated structure with an aspect ratio greater than $\sim 3-5$ (André et al. 2014), and is significantly overdense with respect to its surroundings. The identification of filaments in this work is based on two aspects: the characteristic of morphology and the velocity coherence. As shown in Figure 6, through visual inspecting the channel maps, six skeletons (F1 \sim F6) are carefully depicted and emphasized by different colored dashed lines. To avoid arbitrary judgment, we apply for the Discrete Persistent Structures Extractor (DisPerSE) (Sousbie 2011) to the H₂ column density map derived from ¹³CO to further identify the persistent filamentary structures. In order to not only guarantee a clear skeleton construction, but also retain the information of persistence in morphology as far as possible, the persistence threshold is set to be $3.8 \times 10^{20} \text{ cm}^{-2}$ ($\sim 4\sigma$), and the trimBelow threshold is set to be $9.9 \times 10^{20} \text{ cm}^{-2}$ ($\sim 10\sigma$). The results of a set of 1-pixel wide curves are marked out by black solid lines in Figure 7.

As shown in Figure 7, the skeletons obtained by the two methods are in good agreement with each other, especially for F1, F5, and F6. The DisPerSE identification only relies on column density and is not sensitive enough to the velocity coherence. On the other hand, visual inspection has considered the information of velocity gradients instead of connecting the filaments randomly in spatial distribution. The mean column density profile of each filament is constructed from radial cuts using a similar procedure as described in Arzoumanian et al. (2011) and Palmeirim et al. (2013). The width (deconvolved FWHM) of each filament is derived by applying for Gaussian fitting to the ¹³CO column density profile (see Figure 8). The average spectra of the filaments are extracted to get average v_{LSR} by

Table 4. Properties of filaments

Name	Length	Width	v_{LSR}	Mass	T_{ex}	N_{H_2}	M_{line}
	(pc)	(pc)	kms^{-1}	(M_{\odot})	(K)	(10^{21} cm^{-2})	($M_{\odot} \text{ pc}^{-1}$)
(1)	(2)	(3)	(4)	(5)	(6)	(7)	(8)
F1	51	3.2	-35.7	13650	10.0	5.74	248
F2	32	3.3	-36.4	1725	9.1	1.47	49
F3	75	2.6	-36.7	2245	8.6	1.32	28
F4	38	3.9	-38.6	4045	9.6	3.17	98
F5	90	1.3	-36.5	2343	6.7	1.18	24
F6	47	2.5	-35.6	227	6.6	0.41	4

applying Gaussian fits to ^{13}CO (see Figure 9). Adopting a distance of 4.5 kpc, the lengths of these filaments range from 32 to 90 pc. The widths range from 1.3 to 3.9 pc. We extract each filament along the visual inspection skeleton within the corresponding width and estimate the mean T_{ex} , the mean column density, and the total mass using the same method as in the calculations of the cloud physical parameters. The average line mass (M_{line}) is measured by dividing the mass by length. All the results are listed in Table 4.

Figure 10 shows the velocity field of the observed region. In morphology, F1 \sim F4 mesh together in the ^{12}CO image, while they are isolated relatively in the ^{13}CO image. F1 displays a V-shape opening to east. F2, F3 and F4 are located to the east of F1 and all the four filaments arrange in the order from Northwest to Southeast. F1 connects with F4 at the cross-A and connects with F2 at the cross-B. F3 connects with F2 at the cross-C. F5 and F6 are separated from the complex network and continue to extend eastward. Compared to F1, F2 \sim F6 have lower integrated intensities and similar aspect ratios. The three H II regions are located at the apexes of the filaments, e.g., G154.346+2.606 located within F1, SH2-212 located within F5. The seven IRAS sources are located within the filaments. Five of them are associated with H II regions. For F1–F4, the average v_{LSR} changes from redshifted to blueshifted in a direction from northwest to southeast. The velocity difference is up to $\sim 10 \text{ km s}^{-1}$. Correspondingly, as shown in Figure 9 and Table 4, the line center velocities of the four filament change form from -35.7 km s^{-1} to -38.6 km s^{-1} by a step of $\sim 0.5 \text{ km s}^{-1}$. In order to better analysis kinematic properties of the six filaments, we extend their paths appropriately based on velocity consistency of ^{12}CO , e.g., connecting F4 with F1 and extending the ends of F2, F3, F5 and F6 northward.

As shown in Figure 11, we extract five PV slices (widths ~ 2 pixels) along these extended paths from south end to north end. The filaments show large-scale kinematic oscillation pattern, e.g., F4+F1, F3, F5. We perform a linear fitting to velocity difference to obtain velocity gradient (∇v_{ii}) when the velocity difference is greater than 0.5 km s^{-1} (3 times velocity resolution) over a length of about 4 beam widths ($\sim 4.5 \text{ pc}$). For example, around the G154.346+2.606, the velocity difference is $\sim 1.34 \text{ km s}^{-1}$ along a length of $\sim 0^{\circ}15$ in the south side and $\sim 1.27 \text{ km s}^{-1}$ along a length of $\sim 0^{\circ}13$ length in the north side. The fitted velocity gradients are $\sim 1.27 \text{ km s}^{-1} \text{ pc}^{-1}$ and $\sim 0.39 \text{ km s}^{-1} \text{ pc}^{-1}$, respectively. The feature that velocity gradients with opposite directions existing between the IRAS sources, or H II regions or intersection points is common along these filaments, which implies ongoing mass-flow process around the star forming zones (see discussion below). The results including the center coordinates and half-length of the segments, the length of the segments, the velocity differences, and the ∇v_{ii} are listed in Table 5.

In order to investigate the periodicity of the six filaments, we construct the 1-D second-order structure functions (SF) of velocity and column density. More specifically, we extract slices⁵ along the splines and derive the average values as well as the standard deviations from the intensity-weighted mean velocities of ^{12}CO and the column densities estimated from ^{13}CO . The SF is defined as $S_p(\ell) = \langle |x(r) - x(r + \ell)|^p \rangle$, where $x(r)$ is the velocity or density at position, r , ℓ is the spatial displacement from r , p is the order (Heyer & Dame 2015; Henshaw et al. 2020). The maximum lag to compute the SF is set to be the half of the total length for each filament, as the method is only valid in this range

⁵ The width of slice is 8 pixels for F1 and 5 pixels for F2 - F6.

Table 5. Properties of the segments along the major filament

Name	(l, b , half – length)	segment	Length	Velocity difference	∇v_{\parallel}	Mass	\dot{M}^a
	($^{\circ}, ^{\circ}, ^{\circ}$)	($^{\circ}, ^{\circ}$)	(pc)	(km s^{-1})	$\text{km s}^{-1} \text{pc}^{-1}$	(M_{\odot})	($M_{\odot} \text{Myr}^{-1}$)
F4+F1	(154.76, 2.43, 0.090)	(0.15 , 0.33)	14.1	0.64	0.05	2261	115
	(154.53, 2.48, 0.060)	(0.43 , 0.55)	9.4	2.56	0.31	842	262
	(154.44, 2.54, 0.075)	(0.53 , 0.68)	11.7	0.39	0.04	2920	114
	(154.37, 2.67, 0.065)	(0.75 , 0.88)	10.2	1.27	0.14	5149	720
	(154.43, 2.86, 0.075)	(0.95 , 1.10)	11.7	1.33	0.13	1499	189
	(154.30, 3.31, 0.050)	(1.48 , 1.58)	7.8	0.77	0.11	337	39
F2	(154.47, 2.72, 0.070)	(0.10 , 0.24)	11.0	2.13	0.22	2105	462
	(154.52, 2.66, 0.035)	(0.22 , 0.29)	5.5	1.39	0.29	322	95
F3	(154.54, 2.68, 0.040)	(0.04 , 0.12)	6.3	0.71	0.13	226	30
	(154.57, 2.58, 0.055)	(0.13 , 0.24)	8.6	1.34	0.18	355	65
	(154.75, 2.84, 0.040)	(0.65 , 0.73)	6.3	1.71	0.31	802	246
	(154.72, 2.91, 0.035)	(0.74 , 0.81)	5.5	1.28	0.27	295	81
	(154.79, 3.07, 0.075)	(0.90 , 1.05)	11.7	2.53	0.24	384	92
F5	(155.28, 2.61, 0.050)	(0.35 , 0.45)	7.8	2.22	0.32	390	123
	(155.40, 2.66, 0.050)	(0.50 , 0.60)	7.8	1.42	0.20	756	152
	(155.83, 2.95, 0.050)	(1.10 , 1.20)	7.8	1.41	0.20	284	57
	(155.99, 2.96, 0.050)	(1.30 , 1.40)	7.8	2.90	0.41	303	125
F6	(155.35, 2.36, 0.035)	(0.18 , 0.25)	5.5	3.12	0.66	233	155

^aThe mass-flow rates (\dot{M}) is estimated using a simple cylindrical model from Kirk et al. (2013), $\dot{M} = \frac{\nabla v_{\parallel} M_{\text{gas}}}{\tan(\alpha)}$, where α is the angle of the inclination to the plane of the sky and M_{gas} is the mass of the filament segment, which is estimated from ^{13}CO in this work.

(Henshaw et al. 2020). We present the results in Figure 12. We do not observe significant dip in the SF of F2 and F4, indicating that no evidence for periodicity is found in the data of these two filament; we visually identify dips in F1, F3, F5 and F6 for the column densities profile (their minimum locations are [20,30,11,8]pc), and in F3, F5 and F6 for the velocity profile (with minimum locations of [25,20,13]pc). The minimum potential characteristic lengths as revealed by these dips are approximately 8-30 pc, which are larger but still comparable with the average length of the segments ($\lesssim 10$ pc). The flat slopes of the density structure functions imply that the ^{13}CO 's signal-to-noise ratio is not high enough, which makes the periodicity less evident.

3.5. Clumps

The general models of infinite self-gravitating fluid cylinder (Chandrasekhar & Fermi 1953; Ostriker 1964; Jackson et al. 2010) suggest that the entire filament will collapse toward the short axis and then fragment into clumps or cores when the M_{line} of an isothermal filament exceeds the critical value for equilibrium. To better understand the evolutionary phases of the filaments and star formation therein, we apply for the Gaussclumps algorithm in GILDAS (Stutzki & Guesten 1990) to the ^{13}CO datacube to search for molecular clumps in the velocity interval of [-42.5, -30.0] kms^{-1} . The threshold is set to be 5σ to avoid false clumps. The rest control parameters s_0, s_a, s_c, w are set to be 1, 1, 1, 2, respectively, which are suggested by Kramer et al. (1998). After removing the clumps with a short axis less than the spatial resolution ($50''$) and those located on the edge of the observed region, a total of 162 clumps are identified. The Gaussclumps fitting procedure gives the information of the clumps including the position in the Galactic coordinate system, angular sizes of the major (Θ_{maj}) and minor axis (Θ_{min}), v_{LSR} , peak temperature (T_{peak}) and spectral FWHM (ΔV). Using the calculation methods in Gong et al. (2016), the physical parameters including the radii after the beam deconvolution (R_{eff}), excitation temperature (T_{ex}), optical depth (τ), column density (N_{H_2}), volume density (n_{H_2}),

surface density (Σ_c), LTE mass (M_{LTE}), virial mass (M_{vir}), and virial parameter ($\alpha_{\text{vir}} = M_{\text{vir}}/M_{\text{LTE}}$) of these clumps are derived. The results are tabulated in Table 8.

The effective radius after deconvolution of the clumps range from 0.3 pc to 1.9 pc with a median value of 0.8 pc. The masses under local equilibrium range from $14 M_{\odot}$ to $2416 M_{\odot}$ with a median value of $78 M_{\odot}$. The excitation temperatures range from 4.6 K to 22.8 K with a median value of 9.5 K. The volume densities range from 70 cm^{-3} to 6554 cm^{-3} with a median value of 590 cm^{-3} . The virial parameters span a range of $0.33 \sim 2.96$ with a median value of 1.15.

As shown in Figure 13, we calculate the thermal and non-thermal velocity dispersions of the 162 clumps following the methods of Xiong et al. (2017). The thermal velocity dispersion of each species is given by $\sigma_{\text{T}}(\mu_{\text{obs}}) = \sqrt{\frac{k_{\text{B}} T_{\text{kin}}}{\mu_{\text{obs}} m_{\text{H}}}}$, where k_{B} is the Boltzmann constant, μ_{obs} is atomic weight of the observed molecule ($\mu_{\text{obs}} = 29$ for ^{13}CO), T_{kin} is the kinetic temperature that equals the excitation temperature and m_{H} is the mass of hydrogen atom. The non-thermal velocity dispersion is estimated by subtracting the thermal velocity dispersion from the measured linewidth, $\sigma_{\text{NT}} = \sqrt{\sigma_{\text{obs}}^2 - \sigma_{\text{T}}^2(\mu_{\text{obs}})}$, where $\sigma_{\text{obs}} = \Delta V / \sqrt{8 \ln 2}$, and ΔV is the measured FWHM from the Gaussclumps procedure. The three dimensional velocity dispersion ($\sigma_{3\text{D}}$) is estimated as $\sigma_{3\text{D}} = \sqrt{3} \sigma_{\text{obs}}$.

3.6. Young Stellar Objects

Using data from 2MASS (Two Micron All Sky Survey, Skrutskie et al. 2006) and WISE (Wide-field Infrared Survey Explorer, Wright et al. 2010) and a categorization scheme supplied by Koenig & Leisawitz (2014), we investigate the disk-bearing candidate YSOs in this region. To complement our catalogue, we use the YSO catalogues from Marton et al. (2016, 2019) who used machine learning classifiers to search for YSOs through WISE photometry and Gaia DR2 (the second Gaia Data Release, Gaia Collaboration et al. 2018). The disk-bearing YSOs can be categorized into three classes based on the Greene et al. (1994) concept: Class I ($\text{ALPHA} \geq 0.3$), flat-spectrum ($0.3 \geq \text{ALPHA} \geq -0.3$), and Class II ($-0.3 \geq \text{ALPHA} \geq -1.6$). The infrared (IR) spectral index ALPHA is defined as $\frac{d \log(\lambda F_{\lambda})}{d \log(\lambda)}$, where F_{λ} is the flux as a function of wavelength λ . A total of 279 disk-bearing candidate YSOs are identified in this region, of which 221 sources have matched Gaia objects and 203 sources have stellar parallax (Plx). To eliminate the foreground objects, we adopt a 30% distance uncertainty of the cloud (Zhang et al. 2019) and compare it with the parallax distance from Gaia ($1/Plx$). Finally, a total of 103 sources are reserved as the YSO sample, including 26 (77) sources with (without) Gaia parallax distance information. If 3σ of the ^{12}CO emission is used to define the boundary of the cloud, 79 sources are located within the cloud. The fraction of foreground/background contamination is estimated to be $\sim 6.6\%$ by the density of sources outside the cloud and the emission area of the cloud. In the YSO sample, 39% are from Marton et al. (2016) and 29% are from Marton et al. (2019). The contamination level may be underestimated as the YSOs identified from Marton et al. (2019) are only retained in the region where the dust opacity value is higher than 1.3×10^{-5} . Of the 79 sources, 32, 24, and 23 are classified as Class I, flat-spectrum, and Class II, respectively. The IR photometric magnitudes, the ALPHA values and the origin of the YSOs sample are listed in Table 9. As shown in Figure 14, most of the candidate YSOs are distributed along the ridgelines of the filaments. In addition, the Class I objects (magenta plus) appear to be assembled nearby the three H II regions.

4. DISCUSSION

4.1. Large-scale Filaments

Giant molecular filaments (GMF) can reach up to Galactic scale and play an important role as part of the spiral arms (Ragan et al. 2014; Wang et al. 2015; Zucker et al. 2015; Du et al. 2017). However, there is no clear definition of the GMF. According to the description of Zhang et al. (2019), in position-position-velocity space, an elongated molecular cloud structure with length greater than 10 pc and mass greater than $10^3 M_{\odot}$ could be considered as GMF. In this MC, except F6, these filaments can be considered as GMF as their length range from ~ 32 pc to ~ 90 pc and mass range from $\sim 1725 M_{\odot}$ to $\sim 13650 M_{\odot}$. The fitted widths of these filaments are 1.3 – 3.9 pc, which are much larger than the typical value with of ‘Herschel filaments’ (0.1 pc, Arzoumanian et al. 2011). The low-J CO only trace relatively diffuse gas and the angular resolution (~ 1.1 pc at a distance of ~ 4.5 kpc) is far from enough to resolve the widths of the filaments.

According to the criteria of hub-filament that a central body of low aspect ratio and high column density surrounded by branches with features of greater aspect ratio and lower column density (Myers 2009), and the criteria of ridge-crest structure that a single dominating denser filament with a disorganised network of lower-density filaments (Hill

Table 6. Characteristic fragmentation lengths of the filaments

Name	l_v^a	$l_{N_{H_2}}^b$	c_s	σ_{obs}	n_c^c	$\lambda_{\text{crit,th}}$	$\lambda_{\text{crit,turb}}$
	pc	pc	(km s ⁻¹)	(km s ⁻¹)	cm ⁻³	pc	pc
F1	-	20	0.17	0.89	366	1.7	9.2
F3	25	30	0.16	0.54	67	3.8	13.0
F5	20	11	0.15	0.56	157	2.3	8.8
F6	13	8	0.14	0.93	12	7.9	52.8

^aPotential characteristic length scales estimated from ¹²CO velocity structure function.

^bPotential characteristic length scales estimated from ¹³CO column density function.

^c $n_c = N_c/\text{width}$.

et al. 2011), we suggest that the construction of the identified filaments is similar to the ‘ridge-nest’ rather than ‘hub-filament’. We consider F1 as the main filament and F2 to F6 as sub-filaments. As shown in Table 4, F1 ~ F5 have larger M_{line} than the critical mass per unit length ($M_{\text{line, crit}}$) in the isothermal cylinder model (Ostriker 1964; Inutsuka & Miyama 1997), here $M_{\text{line, crit}} = 2c_s^2/G \sim 16.4 (T/10\text{K}) M_{\odot}\text{pc}^{-1}$ (c_s is the isothermal sound speed $\sim 0.2 \text{ km s}^{-1}$, and G is the gravitational constant). The $M_{\text{line, crit}}$ is the critical value required for a filament to be gravitationally unstable to radial contraction and fragmentation along its length (Inutsuka & Miyama 1997). The observed M_{line} of F1 ~ F5 exceed $M_{\text{line, crit}}$ except F6. It indicates that filaments F1 ~ F5 are gravitationally unstable and should fragment into dense cores, while F6 may expand eventually.

4.2. Kinematics of the Filaments

According to the theoretical model of an infinite self-gravitating fluid cylinder (Chandrasekhar & Fermi 1953; Ostriker 1964; Jackson et al. 2010), a hydrostatic filament can fragment if perturbations are larger than the critical wavelength of $\lambda_{\text{crit}} = 11H$, and its gravitational instability would peak at $\lambda_{\text{max}} = 2\lambda_{\text{crit}}$. The isothermal scale height H is expressed as $c_s (4\pi G\rho_c)^{-1/2}$, where c_s is the isothermal sound speed ($\sqrt{\frac{k_B T_{\text{kin}}}{\mu_{\text{obs}} m_H}}$), G is the gravitational constant, ρ_c is an initial gas mass density at the center of the filament. If turbulent pressure dominates over thermal pressure, c_s should be replaced by velocity dispersion σ_{obs} . We adopt the initial central density $\rho_c = \mu m_p n_c = \mu m_p N_c/\text{width}$, where N_c is the central column density along the filament, “width” is the deconvolved FWHM from Gaussian fitting of the radial column density profiles (see, Figure 8), m_p is the proton mass, and $\mu = 2.33$ is the molecular weight of molecular gas. The typical observed velocity dispersion σ_{obs} is estimated by $\Delta V/\sqrt{8 \ln 2}$, where ΔV is the average value of FWHM (Gaussian fitting) derived from each ¹³CO spectral line along the filaments. The theoretical predicted fragmentation characteristic lengths for the filaments with dips in their SF are listed in Table 6. The observed fragmentation characteristic lengths of F1, F3, and F5 are comparable with the predicted critical wavelength (λ_{crit}) or maximum wavelength (λ_{max}) of fragmentation of the self gravitating fluid cylinder. As described in Hacar & Tafalla (2011), based on the self-gravitating cylinder model, if the oscillatory pattern along filament is caused by core-forming motions, there will be a phase-shift of $\lambda/4$ between density and velocity. However, using the method of cross-correlation as demonstrated by Henshaw et al. (2020), we have not found significant evidence of the co-oscillation at such phase-shift.

The oscillation pattern along PV diagrams commonly appears in spectral line observations towards filamentary clouds (see, e.g., Jackson et al. 2010; Hacar & Tafalla 2011; Hacar et al. 2013; Guo et al. 2021), which is generally interpreted as mass transport along the segment due to core accretion (Kirk et al. 2013; Henshaw et al. 2014; Heitsch 2013; Lu et al. 2018). We estimate mass-flow rates (\dot{M}) using a simple cylindrical model from Kirk et al. (2013), $\dot{M} = \frac{\nabla v_{\text{in}} M_{\text{gas}}}{\tan(\alpha)}$, where α is the angle of the inclination to the plane of the sky, which is assumed to be 45° (Yuan et al.

2018; Liu et al. 2021). M_{gas} is the mass of the filament segment, which is estimated from ^{13}CO in this work. We apply for this method to the regions where mass-flow may exist along the filaments (see, Figure 11). The results of the mass-flow rates (\dot{M}) along the filaments are listed in Table 5.

Around the H II region G154.346+02.606, the estimated \dot{M} are $\sim 720 M_{\odot}\text{Myr}^{-1}$ and $\sim 114 M_{\odot}\text{Myr}^{-1}$, respectively. This result is consistent with the infall rate of the high-mass star formation regions from high resolution observations, e.g. the hub-filamentary cloud G22 ($\sim 400 M_{\odot}\text{Myr}^{-1}$, Yuan et al. 2018), the infrared dark cloud G14.225-0.506 ($\sim 100 M_{\odot}\text{Myr}^{-1}$, Chen et al. 2019). There may be deviations in mass estimation using different probes, e.g., the mass of G22 is derived from multiple mid-infrared extinction data, while the mass of G14.225-0.506 is estimated from $\text{N}_2\text{H}^+(1-0)$ which has a higher critical density. Due to the assumption of LTE conditions throughout the cloud, optical thin of ^{13}CO and a constant ^{13}CO to H_2 abundance, the mass maybe underestimated by 2-3 times from ^{13}CO in this work (see, e.g., Heyer et al. 2009; Goldsmith et al. 2008). Even so, the estimated mass-flow rate is still higher than $100 M_{\odot}\text{Myr}^{-1}$ which is thought to be high enough to allow the formation of even O-type stars (Inoue et al. 2018). For the region with a high mass flow rate of $\sim 720 M_{\odot}\text{Myr}^{-1}$, we obtain a mean volume density (ρ) of 272 cm^{-3} from ^{13}CO . The timescale of the free-fall time $t_{\text{ff}} = \left(\frac{3\pi}{32G\rho}\right)^{0.5}$ is estimated to be about 3.1 Myr. Within one t_{ff} , the mass would have accumulated to $2232 M_{\odot}$, roughly 7.5% of the total mass of the molecular cloud estimated from ^{13}CO .

There are about nine regions with mass-flow rate around them greater than $100 M_{\odot}\text{Myr}^{-1}$ (marked by bold numbers in Figure 11). These regions include the three H II regions, the intersections of the filaments (cross-A and cross-B), and a dense region along F3. The C^{18}O emission also appears in most of these areas correspondingly. All the systematic velocities at the intersections are relatively redshifted compared to that of the ambient gas, which implies that the intersection could play a role similar to a hub. The IRAS04335+5110 is overlaid with the cross-B and the velocity dispersion there seems relatively larger than its periphery, implying star formation activity is ongoing there. In addition to the star forming zones and intersections, the most eye-catching region is the dense area along F3, which has a material flow rate of $246 M_{\odot}\text{Myr}^{-1}$. It is of interest to study star formation activity therein in the further observations.

4.3. Distribution of the Clumps

As shown in Figure 15, most identified clumps are distributed along the filaments. About 43%(66/153) clumps have a separation less than 2 pc (\sim half of the filaments width) from the nearby backbones of the filaments. The spatial association between filaments and clumps is remarkable, which suggests that clumps form primarily along filaments (see, e.g., André et al. 2013). The ratios of clumps with $\alpha_{\text{vir}} < 1$ and $\alpha_{\text{vir}} < 2$ are approximately 32%(52/162) and 90%(147/162), respectively. Most of the clumps are in gravitationally bound states, implying that the global contraction along filaments is efficient. As shown in Figure 13, similar distributions between the observed velocity dispersion and the calculated non-thermal velocity dispersion suggest that the clumps are dominated by non-thermal motions, e.g., hierarchical, global gravitational collapse, stellar feedbacks, or accretion-driven turbulence, etc.

As shown in Figure 16, the clump C1 (MWISP G154.349+2.609) is located above the demarcation line ($M_c = 870 M_{\odot}(\text{R}/\text{pc})^{1.33}$) between high- and low-mass star formation that suggested by Kauffmann et al. (2010). The surface densities of the clump C1 and C29 (MWISP G154.350+2.610) are higher than the lower limit (0.05 g cm^{-2}) of high-mass star formation suggested by Urquhart et al. (2013). It implies that the two clumps (C1 and C29) have potential to form high-mass stars. These two clumps are located in the apex of filament F1, which is similar with the scene revealed by *Herschel* maps that massive stars tend to form at the junctions of supercritical filaments (see, e.g., Schneider et al. 2010; Hennemann et al. 2012). The most massive clump in this sample is Clump C1. It has a mass of $\sim 2416 M_{\odot}$ with a diameter of $\sim 1.1 \text{ pc}$ and a virial parameter of ~ 0.33 . In addition, we note that clumps with $\alpha_{\text{vir}} \leq 1$ mainly distribute in the apexes of filaments, e.g., the apex of F1, F4, the north of F1, F3, the south of F5. Clumps in these regions may go through rapid collapses to form stars. Generally, a sample of star-forming regions with roughly constant column density should have a mass distribution $M \propto R^{\sigma}$ with $\sigma \simeq 2$. The linear fitted slope of this sample is 2.57 with a correlation coefficient $r \simeq 0.66$, which agrees with the results of Ellsworth-Bowers et al. (2015) and Traficante et al. (2018), greater than the results ($\simeq 1.6 - 1.7$) of Lada et al. (2010), Kauffmann et al. (2010), and Urquhart et al. (2014), and less than the results (≥ 2.7) from Ragan et al. (2009). The slope greater than 2 may be caused by the superposition of mass in the line of sight direction (Ballesteros-Paredes et al. 2020).

4.4. Star Formation Rate and Efficiency

Table 7. The 10 massive candidate YSOs in the observed field.

allwise	l	b	from	Infrared luminosity
	($^{\circ}$)	($^{\circ}$)		(L_{\odot})
J043326.34+504330.2	154.3989685	1.941220484	SVMClassI/II	307
J043543.73+520129.5	153.6823386	3.083409916	ClassI	262
J043620.88+511222.4	154.3536567	2.603973726	SVMClassI/II	793
J043620.99+511254.1	154.3473066	2.610084698	SVMClassI/II	10895
J043621.33+511218.1	154.3553349	2.604027456	SVMClassI/II	232
J043649.54+505242.8	154.647162	2.439575961	SVMClassIII	235
J044027.19+502828.8	155.331961	2.59873844	SVMClassI/II	2944
J044035.03+502710.5	155.3620685	2.599936929	SVMClassI/II	102
J044037.27+502740.7	155.3597037	2.609947118	SVMClassIII	138
J044040.84+502738.5	155.3664467	2.616627731	SVMClassIII	105

^a Integral luminosity estimated from WISE.

The star formation efficiency is defined as the ratio of the mass of the YSOs to the total mass of YSOs and gas: $SFE = \frac{M_{\text{YSO}}}{M_{\text{YSO}} + M_{\text{gas}}}$. We use the trapezoid rule (Dunham et al. 2008, 2015) to integrate over the SEDs of the YSOs sample and the sources that located within the cloud, respectively. As shown in Figure17, the peak position of histogram is $\sim 10L_{\odot}$, indicating that the YSOs sample is complete down to $\sim 10L_{\odot}$. There are 9 out of 10 sources with luminosities above $100L_{\odot}$ located within the 3σ boundary of ^{12}CO emission (see Figure14 and Table7), three of which are distributed around H II region G154.346+02.606, one in H II region SH2-211, four in H II region SH2-212, and one to the south of the filamentary molecular cloud. The contamination from foreground/background on the candidate massive YSOs is estimated to be $\sim 2.3\%$, which is neglected in our following calculation. A total of 8 sources overlap with the filamentary cloud. According to Kryukova et al. (2012), the luminosity function (LF) of high-mass star forming clouds (HLF) have a characteristic tail extending toward luminosities above $100L_{\odot}$. Thus, the candidate YSOs with infrared luminosities above $100L_{\odot}$ could be candidate massive YSOs. However, the number of candidate massive YSOs is incomplete due to the saturation problem of WISE survey. We refer to the massive young stellar catalog from the Red MSX Source Survey (Lumsden et al. 2013) for supplement. Only two H II regions (G155.3319+02.5989 and G154.3472+02.6099) with bolometric luminosity up to 10^4L_{\odot} are found and they are coincides with the candidate massive YSOs in our sample (J044027.19+502828.8 and J043620.99+511254.1, see Table7). Based on the Kroupa IMF, the total number of YSO within the filamentary cloud is estimated to be 1255 assuming that the 8 sources would evolve into high-mass protostellars with mass greater than $8M_{\odot}$. The total mass of YSOs is estimated to be $\sim 627M_{\odot}$ provided that the mean mass of a single candidate YSO is $0.5M_{\odot}$. Given that the mass of molecular cloud ($2.96 \times 10^4M_{\odot}$, from ^{13}CO), the SFE will be $\sim 2.1\%$ in this case.

The ^{13}CO emission area is $\sim 506 \text{ arcmin}^2$ which is corresponded to $\sim 867 \text{ pc}^2$ at a distance of 4.5 kpc. Taking 2 Myr (Evans et al. 2009) and 0.54 Myr (Heiderman & Evans 2015) as the Class I + II and Class I lifetimes, the estimated star formation rate ($SFR = \frac{M_{\text{YSOs}}}{\tau}$, τ is the average lifetime of YSOs), the gas mass surface density ($\Sigma_{^{13}\text{CO}}$) and the SFR surface density (Σ_{SFR}) are $\sim 313 M_{\odot} \text{ Myr}^{-1}$, $\sim 34 M_{\odot} \text{ pc}^{-2}$, and $\sim 0.36 M_{\odot} \text{ Myr}^{-1} \text{ pc}^{-2}$, respectively. These results are comparable with that of Zhang et al. (2019), who investigated systematically the star-forming content of a sample of 57 GMFs and suggested that the SFRs of the GMFs scale similarly with dense gas as those of nearby molecular clouds. However, limited by the resolution, the seemingly individual object could potentially be an unresolved cluster at such a great distance. Considering the influence of YSO clustering, the estimated SFR can only be regarded as a lower limit which may be underestimated by a factor of 1.5 – 7 (Zhang et al. 2019).

4.5. WISE Three-Color Diagram

Figure 18 shows the multi-color WISE image ($22 \mu\text{m}$ in red, $4.6 \mu\text{m}$ in green, and $3.4 \mu\text{m}$ in blue) in the observed region. The $22 \mu\text{m}$ emission is used to trace the small warm dust grains heated by ionized gases. The $4.6 \mu\text{m}$ emission mostly originates from stars associated with the H II regions and is considered as a promising diagnostic in the search for massive candidate YSOs (Cyganowski et al. 2008, 2011). The $3.4 \mu\text{m}$ band contains polycyclic aromatic hydrocarbon

(PAH) emission at $3.3\ \mu\text{m}$ as well as a prominent molecular hydrogen feature at $3.234\ \mu\text{m}$. As shown in Figure 18, the infrared emission in the observed region is dominated by the three H II regions and we describe them below.

4.5.1. H II Regions in the Filaments

G154.346+02.606—As shown in Figure 19, the infrared emission is enclosed by the ^{13}CO emission. In addition, the velocity of hydrogen radio recombination lines (HRRs) is consistent with that of the CO emission (see Table 1). Thus the H II region *G154.346+02.606* is confirmed to be associated with filament F1. IRAS04324+5106 was identified as high-mass protostellar object due to its low FIR luminosity to virial mass ratio (Ao et al. 2018), which is spatially coincident with the ^{13}CO peak emission. One H_2O maser towards IRAS04324+5106 was detected by Wouterloot et al. (1988) using the 100 m Effelsberg telescope. The peak velocity of the maser is $-41\ \text{km s}^{-1}$. Sunada et al. (2007) confirmed this maser in the H_2O survey with the Nobeyama 45 m telescope. The H_2O maser is suggested to be one of the best tracers to the early phases of high-mass star formation (Elitzur et al. 1989; Furuya et al. 2001) as it is often associated with outflow or accretion processes (Sunada et al. 2007). A chain of $350\ \mu\text{m}$ clumps (orange ellipse) were identified by Bolocam Galactic Plane Survey (BGPS, Merello et al. 2015).

In our observations, about 10 ^{13}CO clumps are located around the H II region. Among them, C1 has potential to form high-mass star (see above) and undergoes rapid collapse as it has the largest mass and the smallest virial parameter (0.39). In the sub-region ($154^\circ30' \leq l \leq 154^\circ40'$, $2^\circ55' \leq b \leq 2^\circ65'$, $\sim 61\ \text{pc}^2$), the gas mass estimated from ^{13}CO is $\sim 7803\ M_\odot$. Three Class I sources are found with luminosity greater than $100\ L_\odot$. Assuming that the three Class I sources would evolve into high-mass protostars ($> 8M_\odot$), the total number of YSOs is estimated to be ~ 470 based on the Kroupa IMF. Thus, the SFE, SFR, $\Sigma_{^{13}\text{CO}}$, and Σ_{SFR} are estimated to be about 2.9%, $117\ M_\odot\text{My}^{-1}$, $124\ M_\odot\text{pc}^{-2}$, and $1.88\ M_\odot\text{My}^{-1}\text{pc}^{-2}$, respectively. Within the green contour ($\sim 8.1\ \text{pc}^{-2}$, the ^{13}CO integrated intensity greater $\gtrsim 12.65\ \text{K km s}^{-1}$, equivalent to $N_{\text{H}_2} \gtrsim 6.1 \times 10^{21}\ \text{cm}^{-2}$), the gas mass is estimated to be $\sim 2832\ M_\odot$. The SFE, SFR, $\Sigma_{^{13}\text{CO}}$, and Σ_{SFR} in this area is estimated to be $\sim 7.6\%$, $\sim 117\ M_\odot\text{My}^{-1}$, $\sim 388\ M_\odot\text{pc}^{-2}$, $\sim 16\ M_\odot\text{My}^{-1}\text{pc}^{-2}$. According to the starburst certification standard of $\Sigma_{\text{SFR}} > 1\ M_\odot\text{yr}^{-1}\text{kpc}^{-2}$ (Nguyen-Luong et al. 2016), *G154.346+02.606* would be a promising candidate for mini-starburst.

SH2-211—As shown in Figure 20, in the zoom-in region, the ^{13}CO morphology displays a ringlike structure and is spatially consistent with the infrared bubble in the northwestward. The rough consistency of the v_{LSR} ranges between HRRs and CO suggests that the CO emission is associated with SH2-211 (see Table 1). McCutcheon et al. (1986) revealed three gas components of HII, HI and CO associated with SH2-211 and SH2-212, and suggested that SH2-211 may be located in a more complex molecular environment according to the estimated parameters, e.g, sizes, masses. Two IRAS sources (IRAS04329+5047 and IRAS04329+5045, Klein et al. 2005) are located on the opposite sides of the IR bubble separately. Peak emission of ^{13}CO appears around IRAS04329+5047. Three early-type stars (BOV, $V=15.78$; O9V, $V=15.23$; and O9Ib, $V=13.54$) are suggested as the ionization sources of SH2-211 (Chini & Wink 1984). Three clumps (C118, C101, C46) are located around the bubble. The velocities of C118 ($-39.2\ \text{km s}^{-1}$) and C46 ($-36.7\ \text{km s}^{-1}$) are consistent with F4 and F3 respectively (see Figure 9), while C101 has the moderate velocity among the three. The gas mass calculated from ^{13}CO within the green box ($0^\circ07' \times 0^\circ07'$) is $\sim 275\ M_\odot$. The ^{13}CO emission area is $\sim 14\ \text{pc}^2$. Compared with *G154.346+02.606* and SH2-212, the mass-flow rate along the filament around SH2-211 is the lowest. There are 1 candidate massive YSOs (J043649.54+505242.8) at the center of the IR bubble. Based on the Kroupa IMF, the SFE, SFR, $\Sigma_{^{13}\text{CO}}$, and Σ_{SFR} within the green box are estimated to be about 22%, $39\ M_\odot\text{My}^{-1}$, $19\ M_\odot\text{pc}^{-2}$, and $2.8\ M_\odot\text{My}^{-1}\text{pc}^{-2}$, respectively. The H II region SH2-211 may host ongoing starburst event (Nguyen-Luong et al. 2016). As mentioned before, F3 and F4 has a distinct v_{LSR} (F3 at $-36\ \text{km s}^{-1}$, F4 at $-38\ \text{km s}^{-1}$). Based on the velocity continuity of ^{12}CO , the northwest part is likely to be associated with F3 and the southeast part is likely to be associated with F4. The bubble appears in the intersection of F3 and F4. It is likely that the collision of the two filaments accounts for the star formation and then the H II region.

The heated bubble has a relatively circular morphology. As shown in Figure 21, the CO PV diagram along the bubble also shows a circle morphology, indicating the expansion of the bubble. Assuming the bubble is produced by stellar wind, the mechanical luminosity of the stellar wind can be estimated by $L_{\text{wind}} \approx \frac{1}{3} \left(\frac{n_{\text{gas}}}{\text{cm}^{-3}} \right) \left(\frac{R_c}{\text{pc}} \right)^2 \left(\frac{V_c}{\text{km s}^{-1}} \right)^3 \times 10^{30}\ \text{erg s}^{-1}$ (Weaver et al. 1977), where R_c is the radius of the shell, V_c is the shell expansion velocity, n_{gas} is the density of the cavity within the MC. The R_c ($\sim 2.1\ \text{pc}$) and V_c ($\sim 1.5\ \text{km s}^{-1}$) of the shell are obtained from Figure 21. The n_{gas} ($n_{\text{gas}} = \frac{3N_{\text{shell}}}{R_c}$) estimated from the ^{12}CO emission within the shell is $\sim 1.7 \times 10^3\ \text{cm}^{-3}$. Then the L_{wind} is

estimated to be $\sim 8.4 \times 10^{33} \text{ erg s}^{-1}$. The kinetic time-scale ($t_{\text{kin}} \approx \frac{16 R_c \text{ km s}^{-1}}{27 \text{ pc } v_c}$) for opening such a shell is estimated to be about $\sim 8.2 \times 10^5 \text{ yr}$.

SH2-212—As shown in Figure 22, the ^{13}CO morphology displays an arc-like structure encircling the infrared bubble. The velocities of the HRRLs (see Table 1) differ from the CO molecular gas with an offset of $\sim 5 \text{ km s}^{-1}$. Deharveng et al. (2008) attributed this velocity difference to a scenario of “champagne flow” (Tenorio-Tagle 1979), the ionized gas flows away from the cloud. About six ^{13}CO clumps are semicircling the ionized gas. C37 and C128 have a velocity at -36 km s^{-1} , which is roughly same as that of F5 (see, Figure 9). C11, C24, and C75 have velocities at -35 km s^{-1} , differ from F5 with $\sim 1 \text{ km s}^{-1}$. C115 is the closest clumps to the infrared bubble and has velocity at $\sim -34 \text{ km s}^{-1}$, differ from F5 with $\sim 2 \text{ km s}^{-1}$. Deharveng et al. (2008) suggested the origin of the fragmented molecular gas around the infrared bubble through the collect and collapse process. Near C11 and C37, where the infrared cluster IRAS 04366+5022 is located, a possible second-generation UC H II region is forming (Deharveng et al. 2008). The velocity difference between C11 and C37 may be caused by the formation and ionization of the secondary UC H II region. The mass of the exciting star (No. 228 in Deharveng et al. 2008) of the second-generation UC H II region estimated from SED between $1.25 \mu\text{m}$ and $21.3 \mu\text{m}$ is $\sim 14 M_{\odot}$, and the spectral class is $\sim \text{B0.5V}$ (Jose et al. 2011). The gas mass calculated from ^{13}CO within the green box ($0^{\circ}1 \times 0^{\circ}1$) is $\sim 905 M_{\odot}$. The ^{13}CO emission area is $\sim 24 \text{ pc}^2$. Four candidate massive YSOs are found at the boundary of IR bubble, and the locations of two candidates (J044027.19+502828.8 and J044037.27+502740.7) are consistent with the region of $22 \mu\text{m}$ emission. Based on the Kroupa IMF, the lower limits of SFE, SFR, $\Sigma_{^{13}\text{CO}}$, and Σ_{SFR} within the green box are estimated to be about 15%, $78 M_{\odot} \text{ My}^{-1}$, $36 M_{\odot} \text{ pc}^{-2}$, and $3.1 M_{\odot} \text{ My}^{-1} \text{ pc}^{-2}$, respectively. Therefore, the H II region SH2-212 may also host ongoing starburst event.

4.5.2. Other Regions

As shown in Figure 23, based on the analysis of CO molecular dynamics structure (see Figure 11), we zoom in to nine regions where mass-flow activities exist, including cross-A, cross-B, and cross-C (corresponding to the zoom-in areas 1, 2, and 4). The WISE point sources appear in clusters in these regions and the emission at $4.6 \mu\text{m}$ and $22 \mu\text{m}$ bands is obvious. The $4.6 \mu\text{m}$ emission is consistent with the strong ^{13}CO emission, which implies that YSOs are embedded in the CO clouds. The estimated accretion rates around these regions are $\sim 100 M_{\odot} \text{ Myr}^{-1}$, several times smaller than those around the H II regions. Among the nine regions, the area 2 (cross-B) is probably the most active one with star formation as it has the largest accretion rate. Actually, when examining the entire WISE image, we consider that the entire MC is undergoing active star formation.

5. CONCLUSION

We present a larg-field survey of the $J = 1 - 0$ transition lines of ^{12}CO , ^{13}CO , and C^{18}O towards the Galactic region of $l=[153^{\circ}6, 156^{\circ}5]$ and $b=[1^{\circ}85, 3^{\circ}5]$, using the PMO 13.7 m millimeter telescope. The main results are summarized as follows:

1. A network-shaped cloud is found in the velocity interval of $[-42.5, -30.0] \text{ km s}^{-1}$. The distance is estimated to be $\sim 4.5 \text{ kpc}$. The basic physical parameters including excitation temperatures, H_2 column densities, and masses are estimated from ^{12}CO and ^{13}CO , respectively.
2. Six large-scale filaments are identified from the ^{13}CO emission. By comparing the observed average M_{line} and the $M_{\text{line, crit}}$, filaments F1-F5 are suggested to be under the gravitationally unstable conditions and will fragment into dense cores.
3. The PV diagrams of the filaments (e.g. F1, F5) show oscillation patterns, which is explained by the mass-flow caused by accretion activity. The material seems to transport along the filaments to feed the H II regions G154.346+2.606, SH2-212 and cross-B, with high mass-flow rates larger than $100 M_{\odot} \text{ Myr}^{-1}$. The mass-flow rates in the rest parts of filaments are relatively lower, at a level of a few tens of $M_{\odot} \text{ Myr}^{-1}$.
4. A total of 162 CO clumps are extracted from the ^{13}CO datacube, of which 32% have α_{vir} less than 1 and 90% have α_{vir} less than 2. Rapid collapse seems to take place in the apexes of the filaments as most clumps with α_{vir} less than 1 are located therein. Global contraction along filaments is efficient. We find 163 candidate YSOs within the cloud traced by ^{12}CO . The SFE along the filaments is $\sim 2.1\%$, which is comparable with that of other GMFs.
5. Three H II regions, including G154.346+02.606, SH2-211 and SH2-212, are associated with the filaments. According to the estimated SFR densities ($> 1 M_{\odot} \text{ My}^{-1} \text{ pc}^{-2}$), the three H II regions are considered to host ongoing mini starburst events. In addition, other 9 regions with material flow around show signature of star forming activity in the

WISE three-color diagram. The results from both the CO and infrared emission suggest that the entire filamentary cloud is undergoing intense star formation.

This work was supported by the National key R&D Program of China (grant No.2017YFA0402702), the National Natural Science Foundation of China (grant No. 12041305), and CAS International Cooperation Program (grant No. 114332KYSB20190009). M.Zhang was supported by the National Natural Science Foundation of China (grants No. 12073079). This research made use of the data from the Milky Way Imaging Scroll Painting (MWISP) project, which is a multi-line survey in $^{12}\text{CO}/^{13}\text{CO}/\text{C}^{12}\text{O}$ along the northern galactic plane with PMO-13.7m telescope. We are grateful to all the members of the MWISP working group, particularly the staff members at PMO-13.7m telescope, for their long-term support. MWISP was sponsored by National Key R&D Program of China with grant 2017YFA0402701 and CAS Key Research Program of Frontier Sciences with grant QYZDJ-SSW-SLH047.

Facilities: PMO-13.7m

Software: GILDAS/CLASS (Pety 2005)

REFERENCES

- Anderson, L. D., Armentrout, W. P., Johnstone, B. M., et al. 2015, *ApJS*, 221, 26, doi: [10.1088/0067-0049/221/2/26](https://doi.org/10.1088/0067-0049/221/2/26)
- André, P., Di Francesco, J., Ward-Thompson, D., et al. 2014, in *Protostars and Planets VI*, ed. H. Beuther, R. S. Klessen, C. P. Dullemond, & T. Henning, 27, doi: [10.2458/azu_uapress.9780816531240-ch002](https://doi.org/10.2458/azu_uapress.9780816531240-ch002)
- André, P., Könyves, V., Arzoumanian, D., Palmeirim, P., & Peretto, N. 2013, in *Astronomical Society of the Pacific Conference Series*, Vol. 476, *New Trends in Radio Astronomy in the ALMA Era: The 30th Anniversary of Nobeyama Radio Observatory*, ed. R. Kawabe, N. Kuno, & S. Yamamoto, 95
- André, P., Men'shchikov, A., Bontemps, S., et al. 2010, *A&A*, 518, L102, doi: [10.1051/0004-6361/201014666](https://doi.org/10.1051/0004-6361/201014666)
- Ao, Y., Yang, J., Tatematsu, K., et al. 2018, *AJ*, 156, 210, doi: [10.3847/1538-3881/aae259](https://doi.org/10.3847/1538-3881/aae259)
- Arzoumanian, D., André, P., Didelon, P., et al. 2011, *A&A*, 529, L6, doi: [10.1051/0004-6361/201116596](https://doi.org/10.1051/0004-6361/201116596)
- Ballesteros-Paredes, J., André, P., Hennebelle, P., et al. 2020, *SSRv*, 216, 76, doi: [10.1007/s11214-020-00698-3](https://doi.org/10.1007/s11214-020-00698-3)
- Bally, J. 1981, PhD thesis, Massachusetts Univ., Amherst.
- Balser, D. S., Rood, R. T., Bania, T. M., & Anderson, L. D. 2011, *ApJ*, 738, 27, doi: [10.1088/0004-637X/738/1/27](https://doi.org/10.1088/0004-637X/738/1/27)
- Cantat-Gaudin, T., & Anders, F. 2020, *A&A*, 633, A99, doi: [10.1051/0004-6361/201936691](https://doi.org/10.1051/0004-6361/201936691)
- Carpenter, J. M., Snell, R. L., Schloerb, F. P., & Skrutskie, M. F. 1993, *ApJ*, 407, 657, doi: [10.1086/172548](https://doi.org/10.1086/172548)
- Castets, A., & Langer, W. D. 1995, *A&A*, 294, 835
- Chandrasekhar, S., & Fermi, E. 1953, *ApJ*, 118, 116, doi: [10.1086/145732](https://doi.org/10.1086/145732)
- Chen, H.-R. V., Zhang, Q., Wright, M. C. H., et al. 2019, *ApJ*, 875, 24, doi: [10.3847/1538-4357/ab0f3e](https://doi.org/10.3847/1538-4357/ab0f3e)
- Chini, R., & Wink, J. E. 1984, *A&A*, 139, L5
- Colombo, D., König, C., Urquhart, J. S., et al. 2021, *A&A*, 655, L2, doi: [10.1051/0004-6361/202142182](https://doi.org/10.1051/0004-6361/202142182)
- Cyganowski, C. J., Brogan, C. L., Hunter, T. R., & Churchwell, E. 2011, *ApJ*, 743, 56, doi: [10.1088/0004-637X/743/1/56](https://doi.org/10.1088/0004-637X/743/1/56)
- Cyganowski, C. J., Whitney, B. A., Holden, E., et al. 2008, *AJ*, 136, 2391, doi: [10.1088/0004-6256/136/6/2391](https://doi.org/10.1088/0004-6256/136/6/2391)
- Dame, T. M., Hartmann, D., & Thaddeus, P. 2001, *ApJ*, 547, 792, doi: [10.1086/318388](https://doi.org/10.1086/318388)
- Deharveng, L., Lefloch, B., Kurtz, S., et al. 2008, *A&A*, 482, 585, doi: [10.1051/0004-6361:20079233](https://doi.org/10.1051/0004-6361:20079233)
- Du, X., Xu, Y., Yang, J., & Sun, Y. 2017, *ApJS*, 229, 24, doi: [10.3847/1538-4365/aa5d9d](https://doi.org/10.3847/1538-4365/aa5d9d)
- Du, X., Xu, Y., Yang, J., et al. 2016, *ApJS*, 224, 7, doi: [10.3847/0067-0049/224/1/7](https://doi.org/10.3847/0067-0049/224/1/7)
- Dunham, M. M., Crapsi, A., Evans, Neal J., I., et al. 2008, *ApJS*, 179, 249, doi: [10.1086/591085](https://doi.org/10.1086/591085)
- Dunham, M. M., Allen, L. E., Evans, Neal J., I., et al. 2015, *ApJS*, 220, 11, doi: [10.1088/0067-0049/220/1/11](https://doi.org/10.1088/0067-0049/220/1/11)
- Elitzur, M., Hollenbach, D. J., & McKee, C. F. 1989, *ApJ*, 346, 983, doi: [10.1086/168080](https://doi.org/10.1086/168080)
- Ellsworth-Bowers, T. P., Glenn, J., Riley, A., et al. 2015, *ApJ*, 805, 157, doi: [10.1088/0004-637X/805/2/157](https://doi.org/10.1088/0004-637X/805/2/157)
- Evans, Neal J., I., Dunham, M. M., Jørgensen, J. K., et al. 2009, *ApJS*, 181, 321, doi: [10.1088/0067-0049/181/2/321](https://doi.org/10.1088/0067-0049/181/2/321)
- Foster, T., & Brunt, C. M. 2015, *AJ*, 150, 147, doi: [10.1088/0004-6256/150/5/147](https://doi.org/10.1088/0004-6256/150/5/147)
- Frerking, M. A., Langer, W. D., & Wilson, R. W. 1982, *ApJ*, 262, 590, doi: [10.1086/160451](https://doi.org/10.1086/160451)

- Fukui, Y., Kohno, M., Yokoyama, K., et al. 2018, PASJ, 70, S41, doi: [10.1093/pasj/psy017](https://doi.org/10.1093/pasj/psy017)
- Furuya, R. S., Kitamura, Y., Wootten, H. A., Claussen, M. J., & Kawabe, R. 2001, ApJL, 559, L143, doi: [10.1086/324012](https://doi.org/10.1086/324012)
- Gaia Collaboration, Brown, A. G. A., Vallenari, A., et al. 2018, A&A, 616, A1, doi: [10.1051/0004-6361/201833051](https://doi.org/10.1051/0004-6361/201833051)
- Garden, R. P., Hayashi, M., Gatley, I., Hasegawa, T., & Kaifu, N. 1991, ApJ, 374, 540, doi: [10.1086/170143](https://doi.org/10.1086/170143)
- Goldsmith, P. F., Heyer, M., Narayanan, G., et al. 2008, ApJ, 680, 428, doi: [10.1086/587166](https://doi.org/10.1086/587166)
- Gong, Y., Mao, R. Q., Fang, M., et al. 2016, A&A, 588, A104, doi: [10.1051/0004-6361/201527334](https://doi.org/10.1051/0004-6361/201527334)
- Greene, T. P., Wilking, B. A., Andre, P., Young, E. T., & Lada, C. J. 1994, ApJ, 434, 614, doi: [10.1086/174763](https://doi.org/10.1086/174763)
- Guo, W., Chen, X., Feng, J., et al. 2021, ApJ, 921, 23, doi: [10.3847/1538-4357/ac15fe](https://doi.org/10.3847/1538-4357/ac15fe)
- Hacar, A., & Tafalla, M. 2011, A&A, 533, A34, doi: [10.1051/0004-6361/201117039](https://doi.org/10.1051/0004-6361/201117039)
- Hacar, A., Tafalla, M., Forbrich, J., et al. 2018, A&A, 610, A77, doi: [10.1051/0004-6361/201731894](https://doi.org/10.1051/0004-6361/201731894)
- Hacar, A., Tafalla, M., Kauffmann, J., & Kovács, A. 2013, A&A, 554, A55, doi: [10.1051/0004-6361/201220090](https://doi.org/10.1051/0004-6361/201220090)
- Heiderman, A., & Evans, Neal J., I. 2015, ApJ, 806, 231, doi: [10.1088/0004-637X/806/2/231](https://doi.org/10.1088/0004-637X/806/2/231)
- Heitsch, F. 2013, ApJ, 769, 115, doi: [10.1088/0004-637X/769/2/115](https://doi.org/10.1088/0004-637X/769/2/115)
- Hennemann, M., Motte, F., Schneider, N., et al. 2012, A&A, 543, L3, doi: [10.1051/0004-6361/201219429](https://doi.org/10.1051/0004-6361/201219429)
- Henshaw, J. D., Caselli, P., Fontani, F., Jiménez-Serra, I., & Tan, J. C. 2014, MNRAS, 440, 2860, doi: [10.1093/mnras/stu446](https://doi.org/10.1093/mnras/stu446)
- Henshaw, J. D., Kruijssen, J. M. D., Longmore, S. N., et al. 2020, Nature Astronomy, 4, 1064, doi: [10.1038/s41550-020-1126-z](https://doi.org/10.1038/s41550-020-1126-z)
- Heyer, M., & Dame, T. M. 2015, ARA&A, 53, 583, doi: [10.1146/annurev-astro-082214-122324](https://doi.org/10.1146/annurev-astro-082214-122324)
- Heyer, M., Krawczyk, C., Duval, J., & Jackson, J. M. 2009, ApJ, 699, 1092, doi: [10.1088/0004-637X/699/2/1092](https://doi.org/10.1088/0004-637X/699/2/1092)
- Hill, T., Motte, F., Didelon, P., et al. 2011, A&A, 533, A94, doi: [10.1051/0004-6361/201117315](https://doi.org/10.1051/0004-6361/201117315)
- Hunter, D. A., & Massey, P. 1990, AJ, 99, 846, doi: [10.1086/115378](https://doi.org/10.1086/115378)
- Inoue, A. K., Hirashita, H., & Kamaya, H. 2001, ApJ, 555, 613, doi: [10.1086/321499](https://doi.org/10.1086/321499)
- Inoue, T., Hennebelle, P., Fukui, Y., et al. 2018, PASJ, 70, S53, doi: [10.1093/pasj/psx089](https://doi.org/10.1093/pasj/psx089)
- Inutsuka, S.-i., & Miyama, S. M. 1997, ApJ, 480, 681, doi: [10.1086/303982](https://doi.org/10.1086/303982)
- Jackson, J. M., Allingham, D., Patterson, P., et al. 2019, in American Astronomical Society Meeting Abstracts, Vol. 233, American Astronomical Society Meeting Abstracts #233, 127.06
- Jackson, J. M., Finn, S. C., Chambers, E. T., Rathborne, J. M., & Simon, R. 2010, ApJL, 719, L185, doi: [10.1088/2041-8205/719/2/L185](https://doi.org/10.1088/2041-8205/719/2/L185)
- Johnstone, D., & Bally, J. 1999, ApJL, 510, L49, doi: [10.1086/311792](https://doi.org/10.1086/311792)
- Jose, J., Pandey, A. K., Ogura, K., et al. 2011, MNRAS, 411, 2530, doi: [10.1111/j.1365-2966.2010.17860.x](https://doi.org/10.1111/j.1365-2966.2010.17860.x)
- Kauffmann, J., Bertoldi, F., Bourke, T. L., Evans, N. J., I., & Lee, C. W. 2008, A&A, 487, 993, doi: [10.1051/0004-6361:200809481](https://doi.org/10.1051/0004-6361:200809481)
- Kauffmann, J., Pillai, T., Shetty, R., Myers, P. C., & Goodman, A. A. 2010, ApJ, 716, 433, doi: [10.1088/0004-637X/716/1/433](https://doi.org/10.1088/0004-637X/716/1/433)
- Kirk, H., Myers, P. C., Bourke, T. L., et al. 2013, ApJ, 766, 115, doi: [10.1088/0004-637X/766/2/115](https://doi.org/10.1088/0004-637X/766/2/115)
- Klein, R., Posselt, B., Schreyer, K., Forbrich, J., & Henning, T. 2005, ApJS, 161, 361, doi: [10.1086/496962](https://doi.org/10.1086/496962)
- Koenig, X. P., & Leisawitz, D. T. 2014, ApJ, 791, 131, doi: [10.1088/0004-637X/791/2/131](https://doi.org/10.1088/0004-637X/791/2/131)
- Könyves, V., André, P., Men'shchikov, A., et al. 2015, A&A, 584, A91, doi: [10.1051/0004-6361/201525861](https://doi.org/10.1051/0004-6361/201525861)
- Kramer, C., Stutzki, J., Rohrig, R., & Corneliussen, U. 1998, A&A, 329, 249
- Kryukova, E., Megeath, S. T., Gutermuth, R. A., et al. 2012, AJ, 144, 31, doi: [10.1088/0004-6256/144/2/31](https://doi.org/10.1088/0004-6256/144/2/31)
- Lada, C. J., Lewis, J. A., Lombardi, M., & Alves, J. 2017, A&A, 606, A100, doi: [10.1051/0004-6361/201731221](https://doi.org/10.1051/0004-6361/201731221)
- Lada, C. J., Lombardi, M., & Alves, J. F. 2009, ApJ, 703, 52, doi: [10.1088/0004-637X/703/1/52](https://doi.org/10.1088/0004-637X/703/1/52)
- . 2010, ApJ, 724, 687, doi: [10.1088/0004-637X/724/1/687](https://doi.org/10.1088/0004-637X/724/1/687)
- Lim, B., Sung, H., Bessell, M. S., et al. 2015, AJ, 149, 127, doi: [10.1088/0004-6256/149/4/127](https://doi.org/10.1088/0004-6256/149/4/127)
- Liu, X.-L., Xu, J.-L., Wang, J.-J., et al. 2021, A&A, 646, A137, doi: [10.1051/0004-6361/201935035](https://doi.org/10.1051/0004-6361/201935035)
- Lockman, F. J. 1989, ApJS, 71, 469, doi: [10.1086/191383](https://doi.org/10.1086/191383)
- Louvet, F., Motte, F., Hennebelle, P., et al. 2014, A&A, 570, A15, doi: [10.1051/0004-6361/201423603](https://doi.org/10.1051/0004-6361/201423603)
- Lu, X., Zhang, Q., Liu, H. B., et al. 2018, ApJ, 855, 9, doi: [10.3847/1538-4357/aaad11](https://doi.org/10.3847/1538-4357/aaad11)
- Lumsden, S. L., Hoare, M. G., Urquhart, J. S., et al. 2013, ApJS, 208, 11, doi: [10.1088/0067-0049/208/1/11](https://doi.org/10.1088/0067-0049/208/1/11)
- Marton, G., Tóth, L. V., Paladini, R., et al. 2016, MNRAS, 458, 3479, doi: [10.1093/mnras/stw398](https://doi.org/10.1093/mnras/stw398)
- Marton, G., Ábrahám, P., Szegedi-Elek, E., et al. 2019, MNRAS, 487, 2522, doi: [10.1093/mnras/stz1301](https://doi.org/10.1093/mnras/stz1301)

- Mattern, M., Kauffmann, J., Csengeri, T., et al. 2018, *A&A*, 619, A166, doi: [10.1051/0004-6361/201833406](https://doi.org/10.1051/0004-6361/201833406)
- McCutcheon, W. H., Dewdney, P. E., Purton, C. R., Wall, W. F., & Sato, T. 1986, in *Bulletin of the American Astronomical Society*, Vol. 18, 921
- Merello, M., Evans, Neal J., I., Shirley, Y. L., et al. 2015, *ApJS*, 218, 1, doi: [10.1088/0067-0049/218/1/1](https://doi.org/10.1088/0067-0049/218/1/1)
- Moffat, A. F. J., Fitzgerald, M. P., & Jackson, P. D. 1979, *A&AS*, 38, 197
- Motte, F., Bontemps, S., & Louvet, F. 2018, *ARA&A*, 56, 41, doi: [10.1146/annurev-astro-091916-055235](https://doi.org/10.1146/annurev-astro-091916-055235)
- Myers, P. C. 2009, *ApJ*, 700, 1609, doi: [10.1088/0004-637X/700/2/1609](https://doi.org/10.1088/0004-637X/700/2/1609)
- Nguyen Luong, Q., Motte, F., Hennemann, M., et al. 2011, *A&A*, 535, A76, doi: [10.1051/0004-6361/201117831](https://doi.org/10.1051/0004-6361/201117831)
- Nguyen-Luong, Q., Nguyen, H. V. V., Motte, F., et al. 2016, *ApJ*, 833, 23, doi: [10.3847/0004-637X/833/1/23](https://doi.org/10.3847/0004-637X/833/1/23)
- Ostriker, J. 1964, *ApJ*, 140, 1056, doi: [10.1086/148005](https://doi.org/10.1086/148005)
- Palmeirim, P., André, P., Kirk, J., et al. 2013, *A&A*, 550, A38, doi: [10.1051/0004-6361/201220500](https://doi.org/10.1051/0004-6361/201220500)
- Pety, J. 2005, in *SF2A-2005: Semaine de l'Astrophysique Française*, ed. F. Casoli, T. Contini, J. M. Hameury, & L. Pagani, 721
- Pirogov, L. 1999, *A&A*, 348, 600
- Pismis, P., Hasse, I., & Quintero, A. 1991, *PASP*, 103, 843, doi: [10.1086/132891](https://doi.org/10.1086/132891)
- Ragan, S. E., Bergin, E. A., & Gutermuth, R. A. 2009, *ApJ*, 698, 324, doi: [10.1088/0004-637X/698/1/324](https://doi.org/10.1088/0004-637X/698/1/324)
- Ragan, S. E., Henning, T., Tackenberg, J., et al. 2014, *A&A*, 568, A73, doi: [10.1051/0004-6361/201423401](https://doi.org/10.1051/0004-6361/201423401)
- Reid, M. J., Dame, T. M., Menten, K. M., & Brunthaler, A. 2016, *ApJ*, 823, 77, doi: [10.3847/0004-637X/823/2/77](https://doi.org/10.3847/0004-637X/823/2/77)
- Reid, M. J., Menten, K. M., Brunthaler, A., et al. 2019, *ApJ*, 885, 131, doi: [10.3847/1538-4357/ab4a11](https://doi.org/10.3847/1538-4357/ab4a11)
- Russek, D., Schneider, N., Anderson, L. D., et al. 2013, *A&A*, 554, A42, doi: [10.1051/0004-6361/201219971](https://doi.org/10.1051/0004-6361/201219971)
- Schneider, N., Csengeri, T., Bontemps, S., et al. 2010, *A&A*, 520, A49, doi: [10.1051/0004-6361/201014481](https://doi.org/10.1051/0004-6361/201014481)
- Shan, W., Yang, J., Shi, S., et al. 2012, *IEEE Transactions on Terahertz Science and Technology*, 2, 593, doi: [10.1109/TTHZ.2012.2213818](https://doi.org/10.1109/TTHZ.2012.2213818)
- Skrutskie, M. F., Cutri, R. M., Stiening, R., et al. 2006, *AJ*, 131, 1163, doi: [10.1086/498708](https://doi.org/10.1086/498708)
- Snell, R. L., Dickman, R. L., & Huang, Y. L. 1990, *ApJ*, 352, 139, doi: [10.1086/168521](https://doi.org/10.1086/168521)
- Soler, J. D., Beuther, H., Syed, J., et al. 2020, *A&A*, 642, A163, doi: [10.1051/0004-6361/202038882](https://doi.org/10.1051/0004-6361/202038882)
- Sousbie, T. 2011, *MNRAS*, 414, 350, doi: [10.1111/j.1365-2966.2011.18394.x](https://doi.org/10.1111/j.1365-2966.2011.18394.x)
- Stutzki, J., & Guesten, R. 1990, *ApJ*, 356, 513, doi: [10.1086/168859](https://doi.org/10.1086/168859)
- Su, Y., Yang, J., Zhang, S., et al. 2019, *ApJS*, 240, 9, doi: [10.3847/1538-4365/aaflc8](https://doi.org/10.3847/1538-4365/aaflc8)
- Sun, Y., Xu, Y., Yang, J., et al. 2015, *ApJL*, 798, L27, doi: [10.1088/2041-8205/798/2/L27](https://doi.org/10.1088/2041-8205/798/2/L27)
- Sun, Y., Yang, J., Yan, Q.-Z., et al. 2021, *ApJS*, 256, 32, doi: [10.3847/1538-4365/ac11fe](https://doi.org/10.3847/1538-4365/ac11fe)
- Sunada, K., Nakazato, T., Ikeda, N., et al. 2007, *PASJ*, 59, 1185, doi: [10.1093/pasj/59.6.1185](https://doi.org/10.1093/pasj/59.6.1185)
- Syed, J., Soler, J. D., Beuther, H., et al. 2021, arXiv e-prints, arXiv:2111.01057, <https://arxiv.org/abs/2111.01057>
- Tatematsu, K., Kandori, R., Umemoto, T., & Sekimoto, Y. 2008, *PASJ*, 60, 407, doi: [10.1093/pasj/60.3.407](https://doi.org/10.1093/pasj/60.3.407)
- Tenorio-Tagle, G. 1979, *A&A*, 71, 59
- Traficante, A., Duarte-Cabral, A., Elia, D., et al. 2018, *MNRAS*, 477, 2220, doi: [10.1093/mnras/sty798](https://doi.org/10.1093/mnras/sty798)
- Treviño-Morales, S. P., Fuente, A., Sánchez-Monge, Á., et al. 2019, *A&A*, 629, A81, doi: [10.1051/0004-6361/201935260](https://doi.org/10.1051/0004-6361/201935260)
- Urquhart, J. S., Moore, T. J. T., Schuller, F., et al. 2013, *MNRAS*, 431, 1752, doi: [10.1093/mnras/stt287](https://doi.org/10.1093/mnras/stt287)
- Urquhart, J. S., Moore, T. J. T., Csengeri, T., et al. 2014, *MNRAS*, 443, 1555, doi: [10.1093/mnras/stu1207](https://doi.org/10.1093/mnras/stu1207)
- Vallée, J. P. 2008, *AJ*, 135, 1301, doi: [10.1088/0004-6256/135/4/1301](https://doi.org/10.1088/0004-6256/135/4/1301)
- Wang, K., Testi, L., Ginsburg, A., et al. 2015, *MNRAS*, 450, 4043, doi: [10.1093/mnras/stv735](https://doi.org/10.1093/mnras/stv735)
- Weaver, R., McCray, R., Castor, J., Shapiro, P., & Moore, R. 1977, *ApJ*, 218, 377, doi: [10.1086/155692](https://doi.org/10.1086/155692)
- Wouterloot, J. G. A., Brand, J., & Henkel, C. 1988, *A&A*, 191, 323
- Wright, E. L., Eisenhardt, P. R. M., Mainzer, A. K., et al. 2010, *AJ*, 140, 1868, doi: [10.1088/0004-6256/140/6/1868](https://doi.org/10.1088/0004-6256/140/6/1868)
- Xiong, F., Chen, X., Yang, J., et al. 2017, *ApJ*, 838, 49, doi: [10.3847/1538-4357/aa6443](https://doi.org/10.3847/1538-4357/aa6443)
- Yan, Q.-Z., Yang, J., Su, Y., Sun, Y., & Wang, C. 2020, *ApJ*, 898, 80, doi: [10.3847/1538-4357/ab9f9c](https://doi.org/10.3847/1538-4357/ab9f9c)
- Yang, J., Jiang, Z., Wang, M., Ju, B., & Wang, H. 2002, *ApJS*, 141, 157, doi: [10.1086/340038](https://doi.org/10.1086/340038)
- Yuan, J., Li, J.-Z., Wu, Y., et al. 2018, *ApJ*, 852, 12, doi: [10.3847/1538-4357/aa9d40](https://doi.org/10.3847/1538-4357/aa9d40)
- Yuan, L., Yang, J., Du, F., et al. 2021, *ApJS*, 257, 51, doi: [10.3847/1538-4365/ac242a](https://doi.org/10.3847/1538-4365/ac242a)
- Zhang, M., Kainulainen, J., Mattern, M., Fang, M., & Henning, T. 2019, *A&A*, 622, A52, doi: [10.1051/0004-6361/201732400](https://doi.org/10.1051/0004-6361/201732400)
- Zucker, C., Battersby, C., & Goodman, A. 2015, *ApJ*, 815, 23, doi: [10.1088/0004-637X/815/1/23](https://doi.org/10.1088/0004-637X/815/1/23)

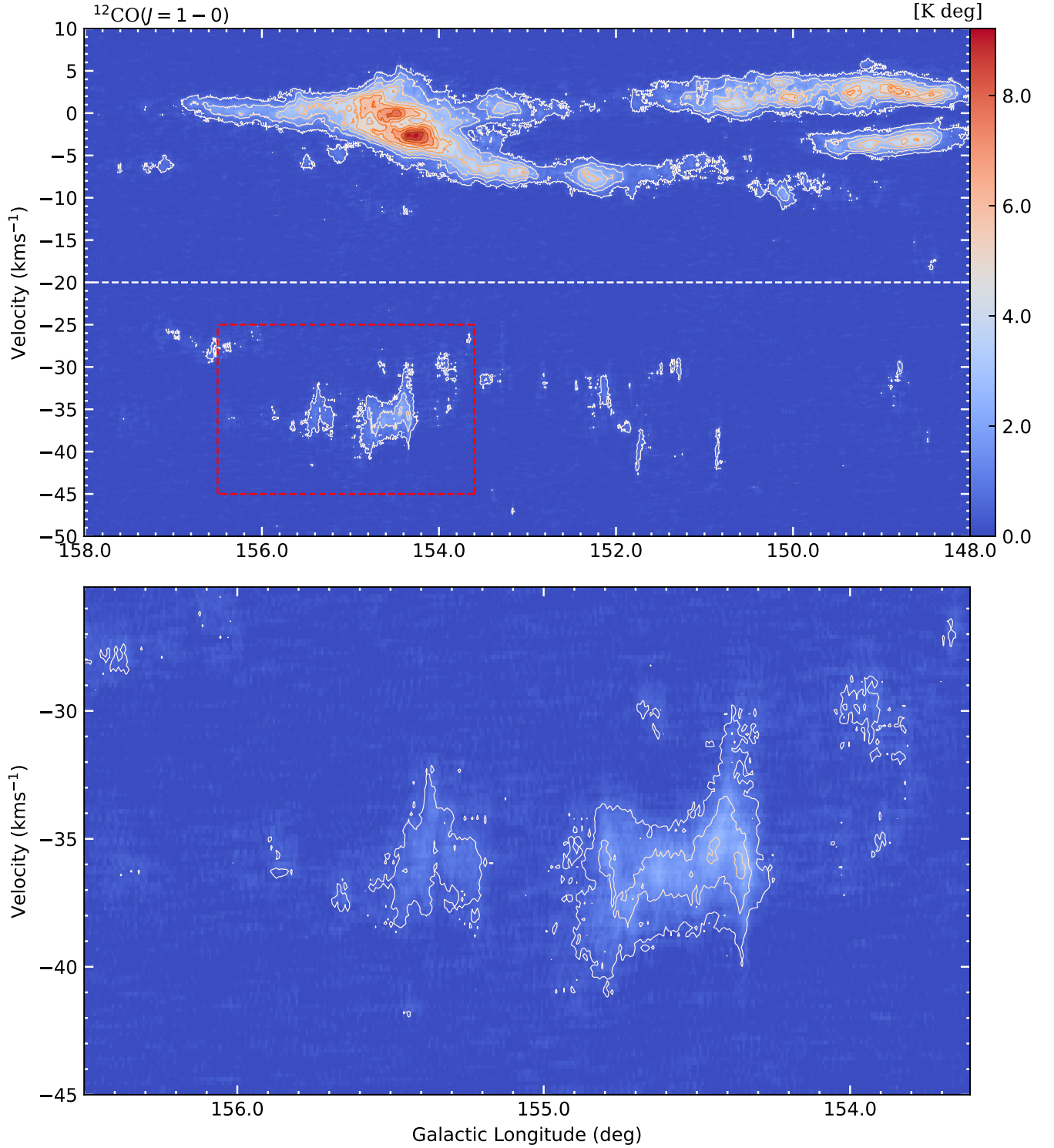


Figure 1. Upper panel: The LV map of ^{12}CO towards the region of $148^\circ \leq l \leq 158^\circ$ and $-50 \leq v \leq 10 \text{ km s}^{-1}$. The latitude is integrated from $1^\circ 85'$ to $3^\circ 5'$. The integrated noise level (σ) is about 0.051 K deg . The contours are set from 10σ to peak value (9.2 K deg) by a step of 10%. The horizontal white dashed line separates the velocity intervals into Local Arm and Perseus/Outer Arm (see Dame et al. 2001; Reid et al. 2019). The red rectangle indicates the region focused in this work. Below panel: The zoom-in map of the red rectangle with a velocity range of $[-45, -25] \text{ km s}^{-1}$ and a longitude range of $[153^\circ 6', 156^\circ 5']$.

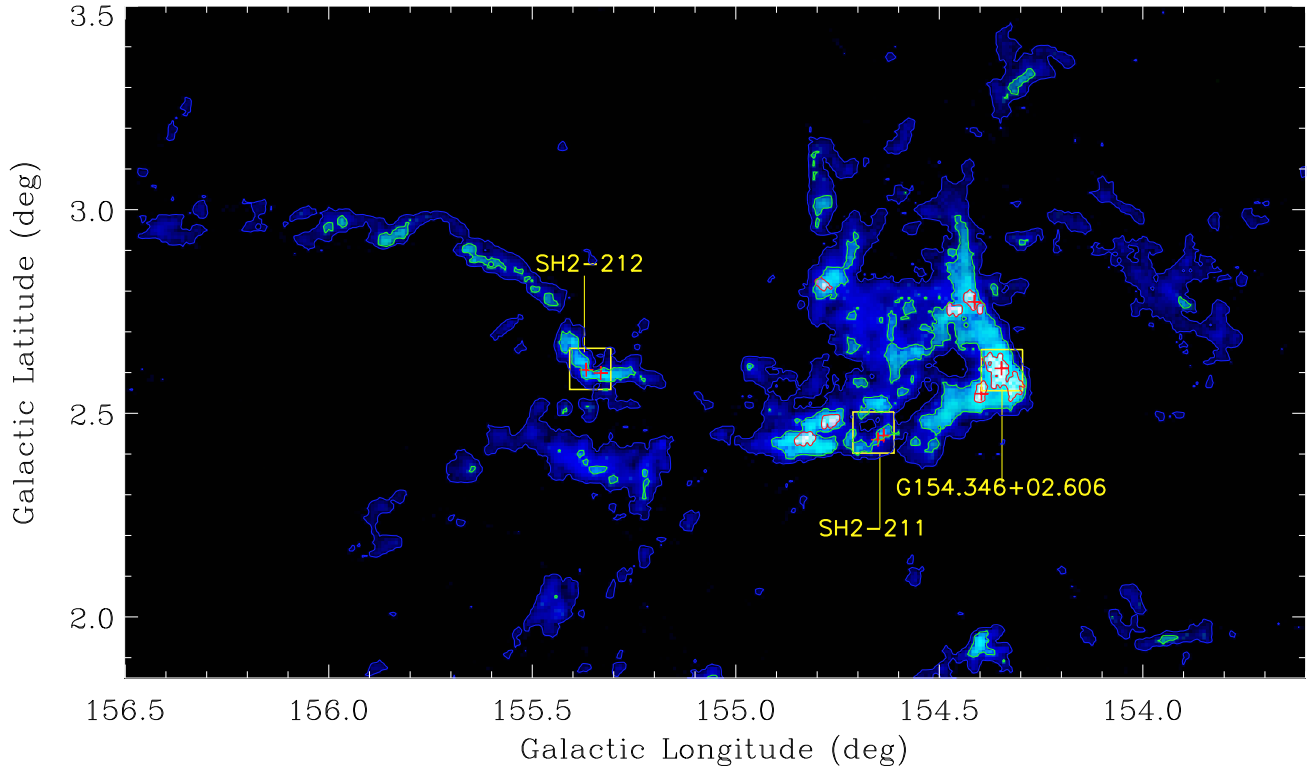


Figure 2. The three-color image of ^{12}CO (blue), ^{13}CO (green), and C^{18}O (red) in the velocity interval of $[-42.5, -30.0] \text{ km s}^{-1}$. For ^{12}CO and ^{13}CO , the pixels with emission above 3σ with at least 3 continuous channels are used for integration. The pixels of C^{18}O are obtained by DBSCAN algorithm (see Section 3.1). The blue, green and red contours are the 3σ , 3σ , and 1σ boundaries for ^{12}CO , ^{13}CO and C^{18}O , respectively. The yellow squares and the red pluses represent the locations of H II regions and IRAS sources, respectively.

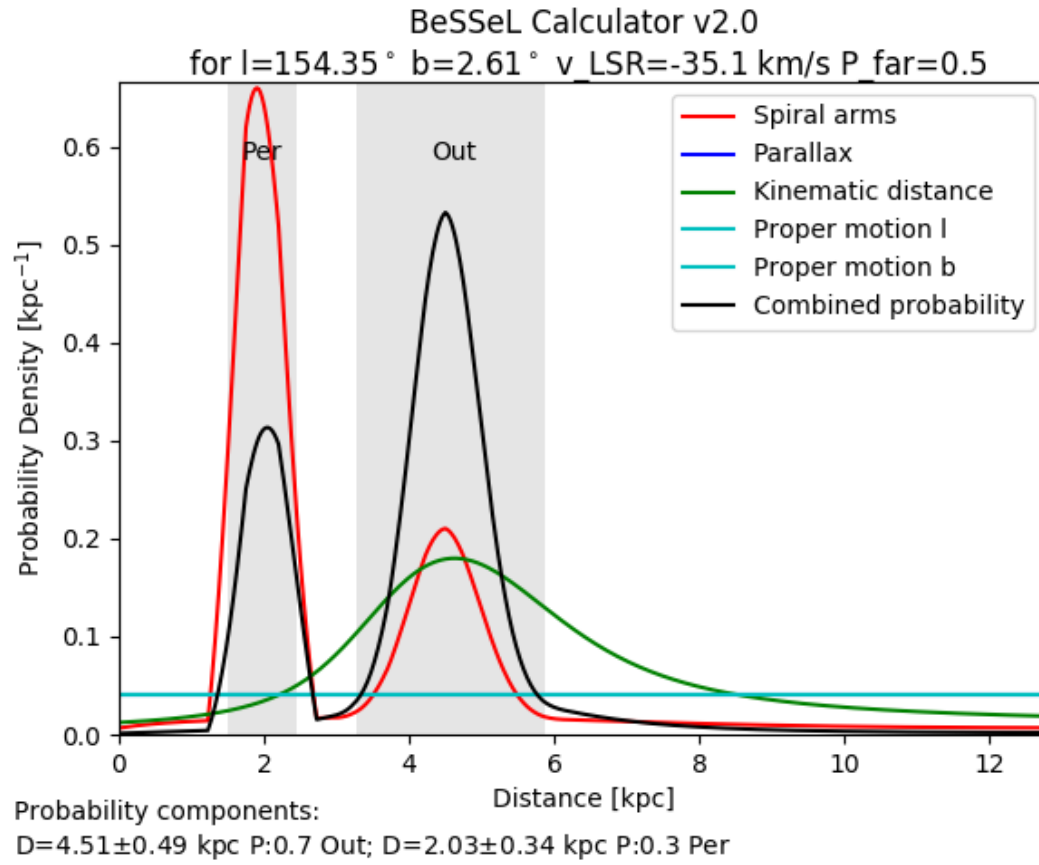


Figure 3. Distance probability density function of the position NO.1 (see Table2), using the Bayesian distance calculator (Reid et al. 2016).

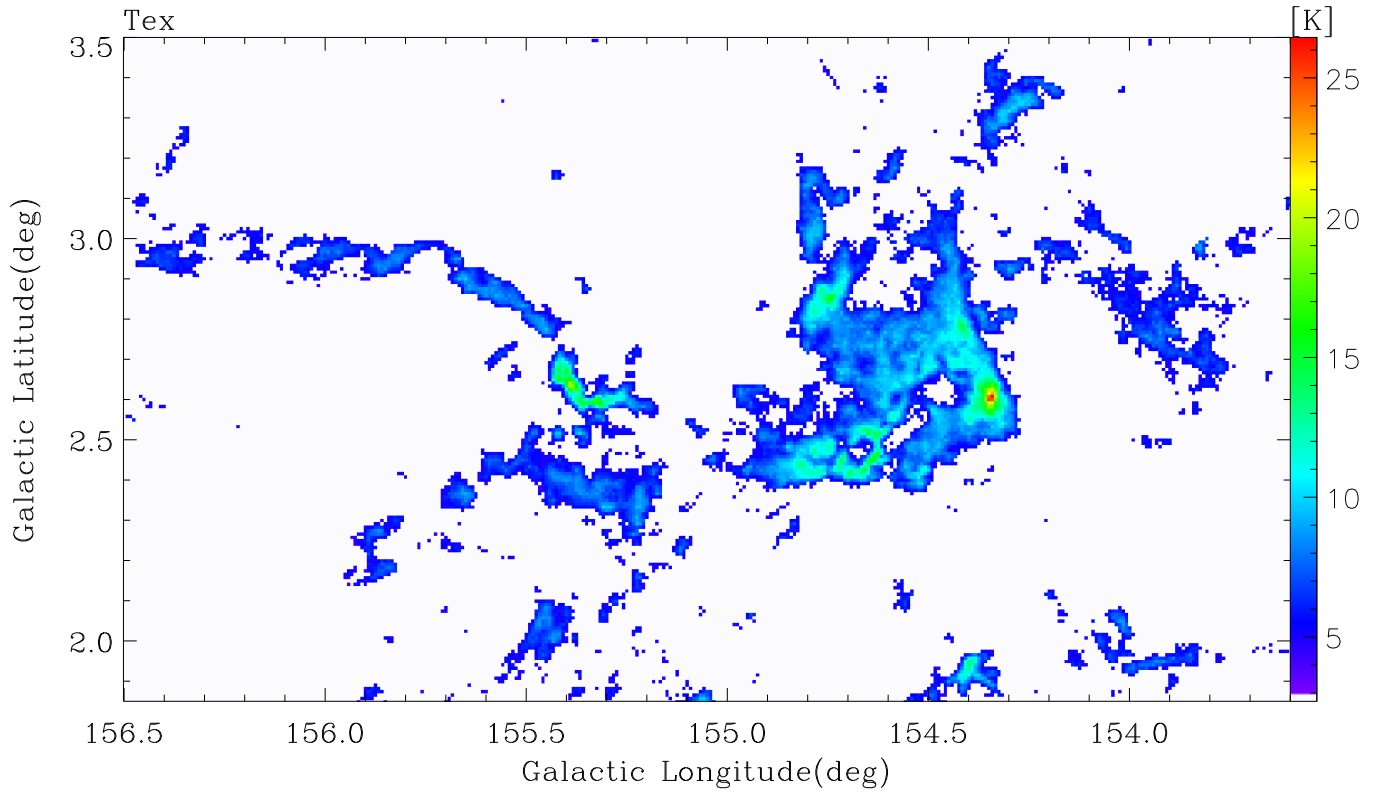


Figure 4. The distribution of the excitation temperature calculated from the peak value of the main beam temperature of ^{12}CO in the velocity interval of $[-42.5, -30.0] \text{ km s}^{-1}$.

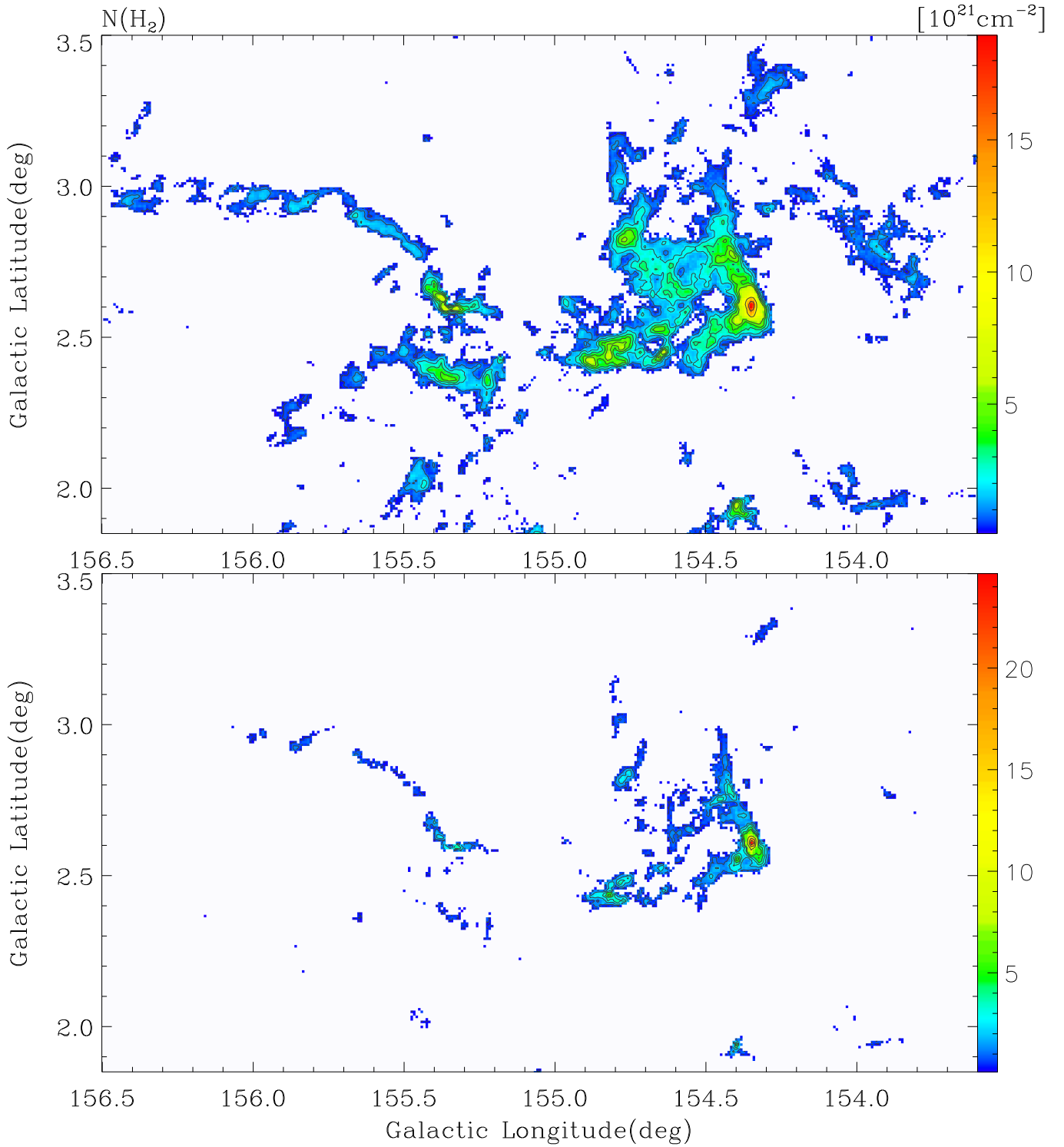


Figure 5. The H_2 column density maps derived from ^{12}CO (upper panel) and ^{13}CO (bottom panel) in the velocity interval of $[-42.5, -30]\text{km s}^{-1}$, respectively. The contours are 0.4 (3σ noise level), $1, 2, 3, 4, 5, 10, 15 \times 10^{21}\text{cm}^{-2}$, respectively. The colorbar is in unit of 10^{21}cm^{-2} .

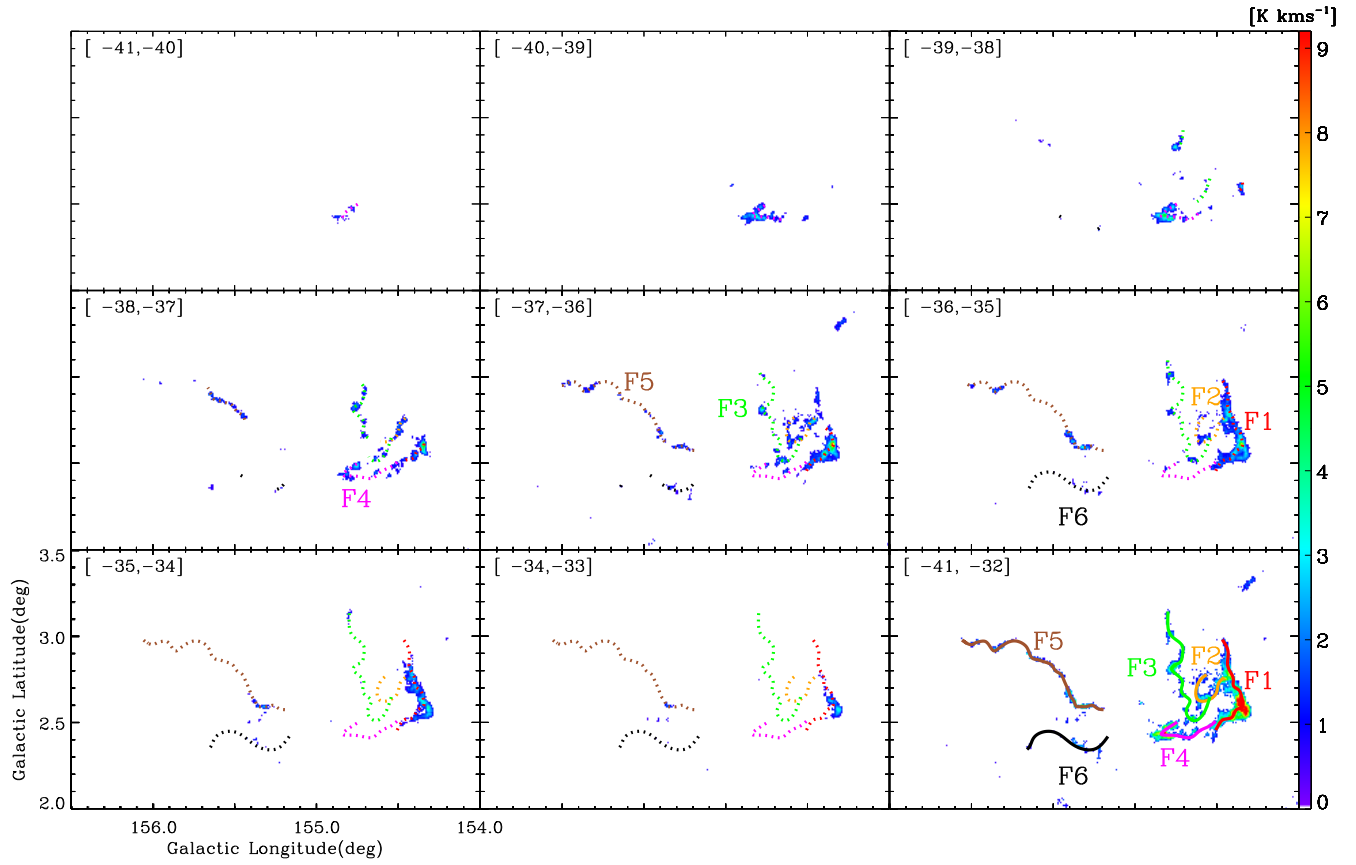


Figure 6. The ^{13}CO channel maps from -41 km s^{-1} to -32 km s^{-1} by a step of 1 km s^{-1} . Only pixels with at least 3 channels above 3 sigma are kept for integration. The colored dotted lines indicate the filament skeletons identified by visual inspection step by step. The names are marked out beside each filaments. The last panel shows the intensity image integrated within $[-41, -32] \text{ km s}^{-1}$ that overlapped with the visual inspection filaments (colored solid lines).

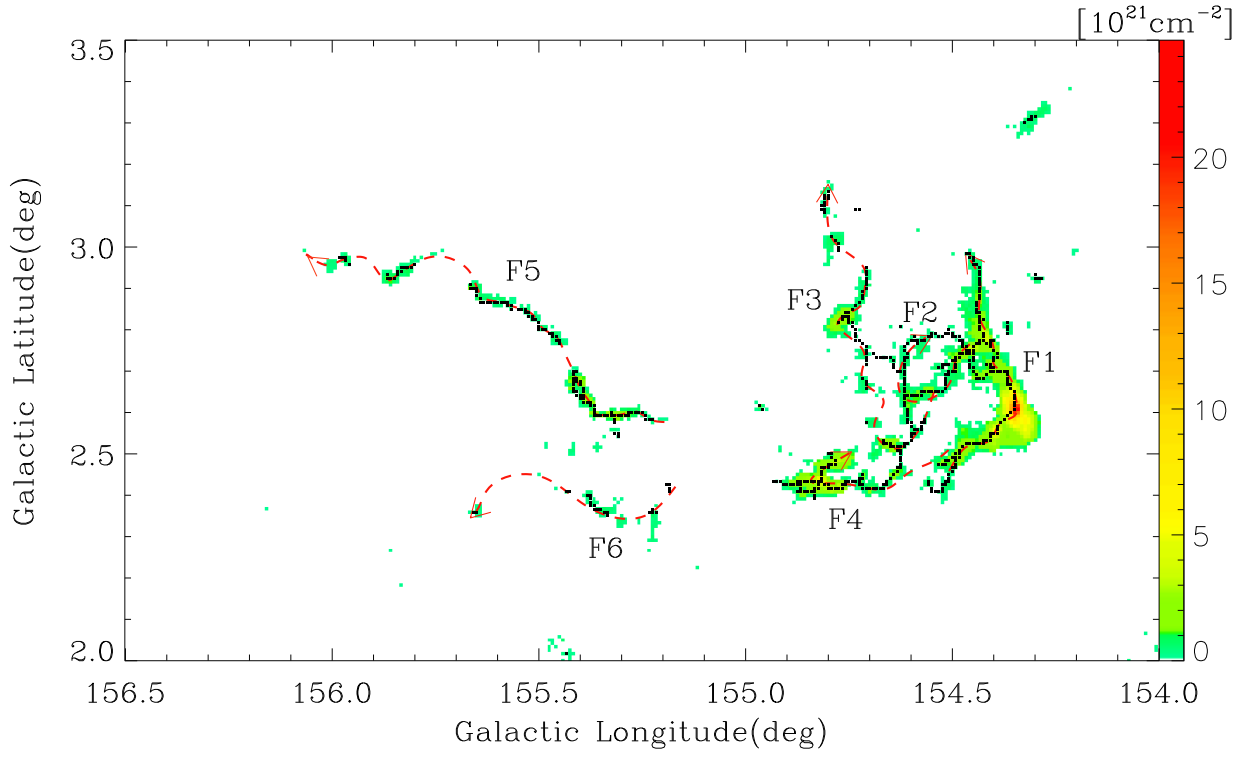


Figure 7. The H_2 column density map estimated from the ^{13}CO emission. The dotted black lines and the red dashed lines represent the filament skeletons that are extracted by DisPerSE algorithm and visual inspection, respectively. The colorbar is in unit of 10^{21}cm^{-2} .

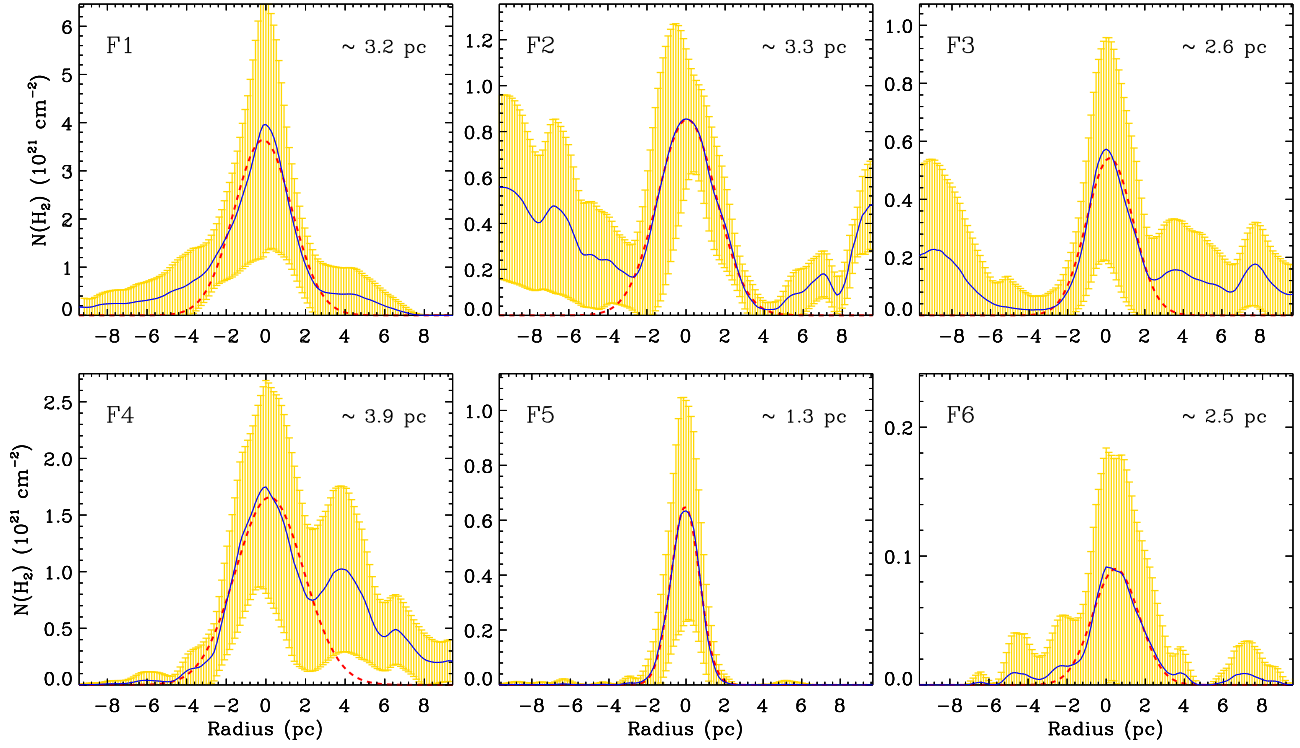


Figure 8. The blue curves represent the mean radial column density profiles of the ^{13}CO emission. The yellow bars indicate the $\pm 1\sigma$ dispersion. The red dashed curves represent the Gaussian fitting results. The peak position in each profile is regarded as the center of the profile. The widths (deconvolved FWHMs) are marked in the upper right corner of each panel.

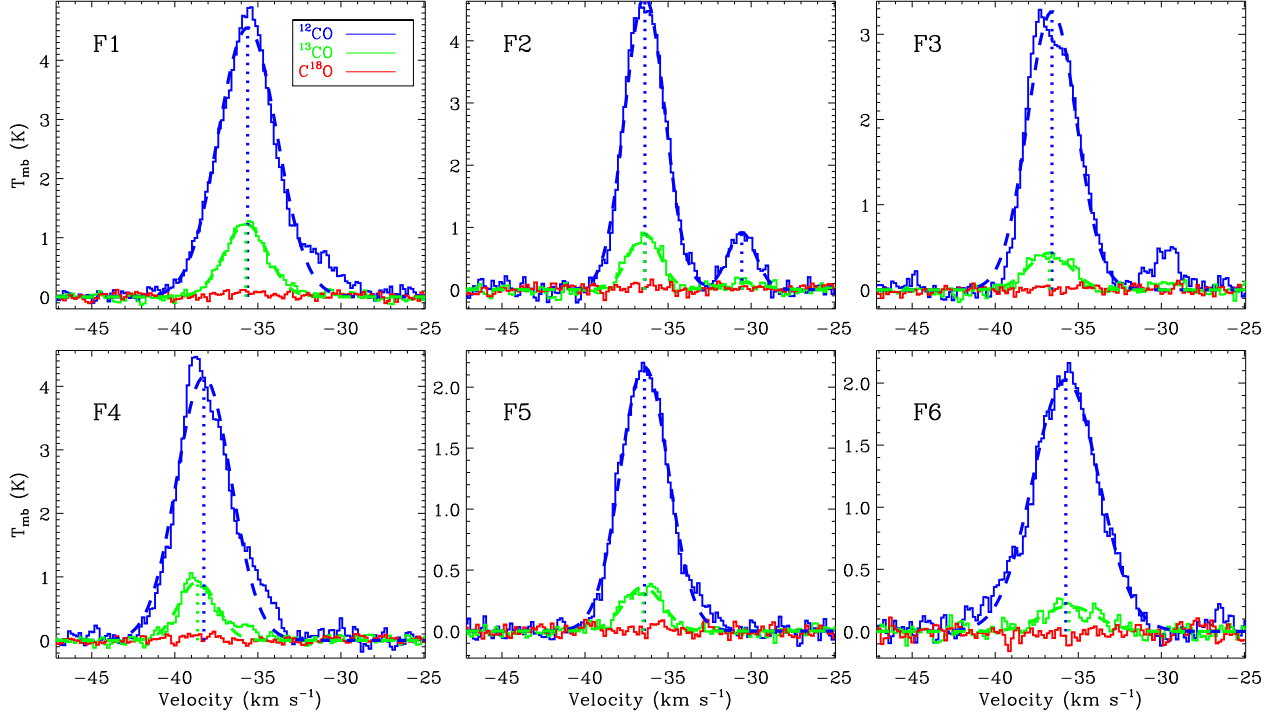


Figure 9. Averaged spectral lines of ^{12}CO (blue), ^{13}CO (green), and C^{18}O (red) extracted from the six identified filaments. The dashed lines with the corresponding colors are the Gaussian fitting results. The vertical dotted lines indicate the fitted central velocity. The average v_{LSR} of the filaments are obtained from ^{13}CO .

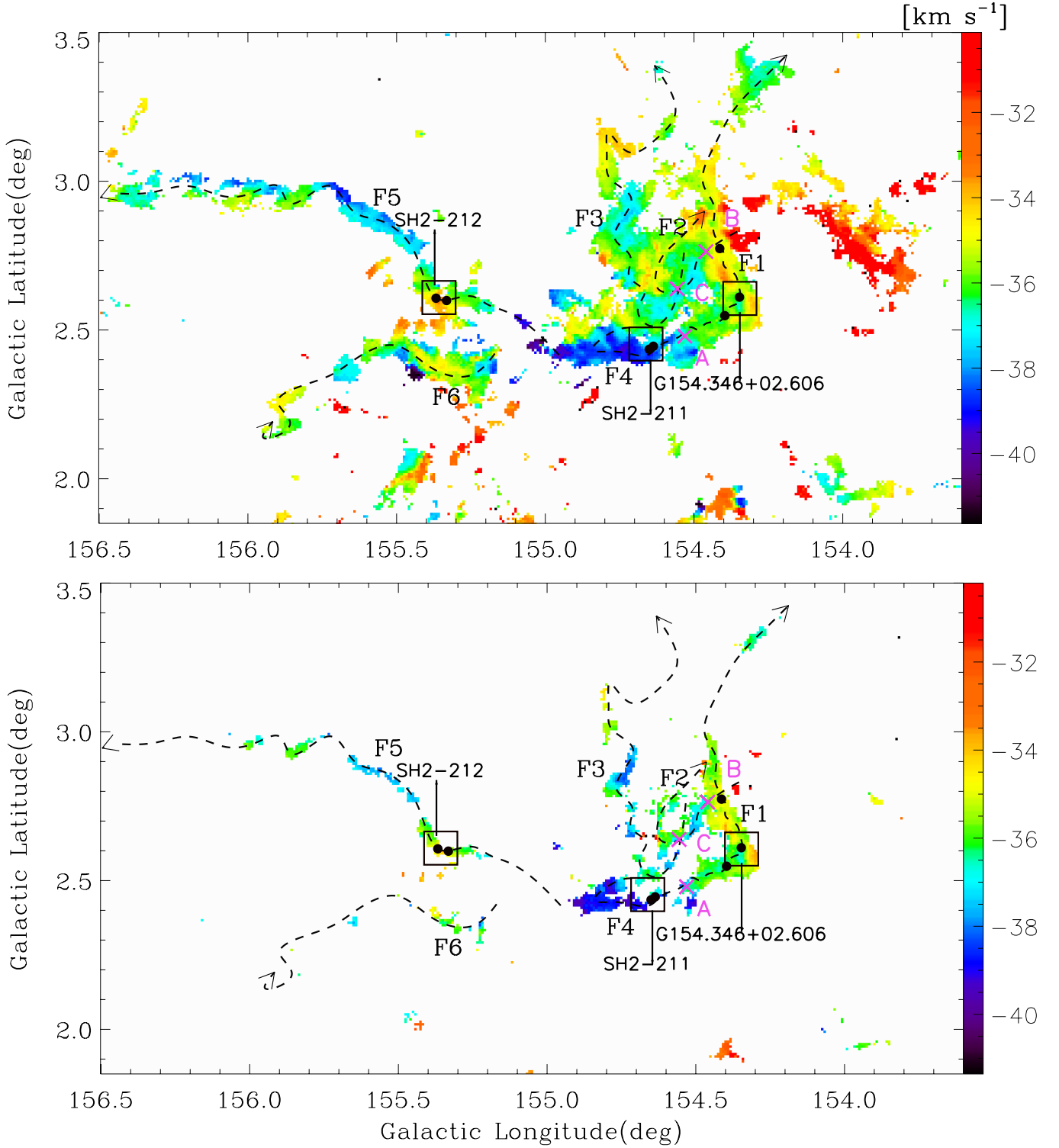


Figure 10. The velocity-field maps (moment 1) of ^{12}CO (upper panel) and ^{13}CO (bottom panel). The black arrow lines indicate the extended paths according to the ^{12}CO emission. The name of each filament is marked beside. The symbols of squares, solid circles, magenta crosses represent the associated H II regions, IRAS sources, and the intersection positions between filaments, respectively. The coordinates (l, b) of the intersection are cross-A $\sim (154^\circ 531, 2^\circ 479)$, cross-B $\sim (154^\circ 452, 2^\circ 754)$, and cross-C $\sim (154^\circ 556, 2^\circ 638)$, respectively.

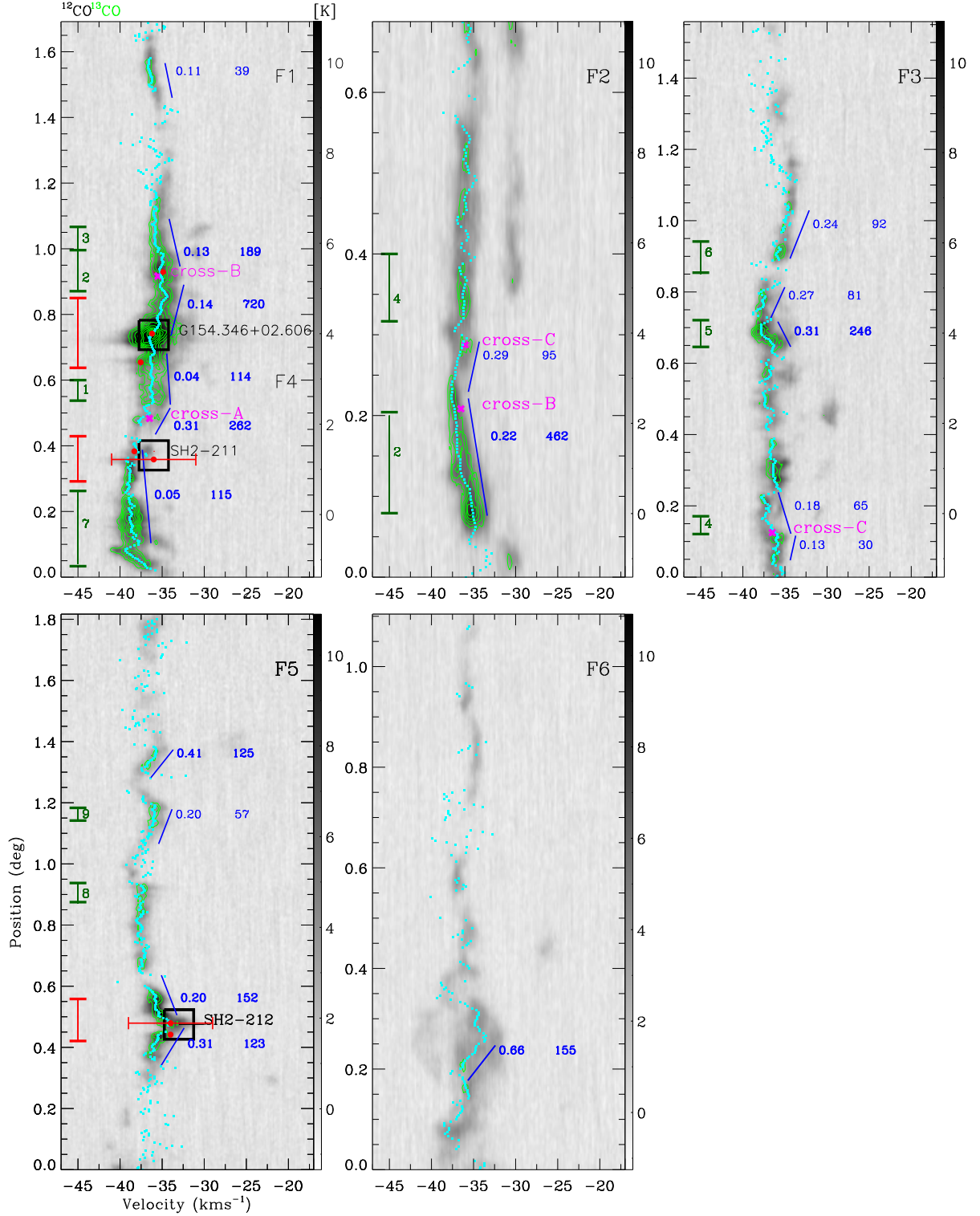


Figure 11. The PV diagrams of ^{12}CO (grayscale) and ^{13}CO (green contours) along the filaments. The green contours are set from 3σ to peak value in step of 3σ . The colorbar is in unit of K. In order to preserve the velocity continuity, pixels above 2σ are kept to construct the ^{13}CO m1 profiles (cyan dotted lines). The blue lines are the linear fitting results of the corresponding segments. The corresponding velocity gradients in units of $\text{km s}^{-1} \text{pc}^{-1}$ and the mass-flow rates in units of $M_{\odot} \text{Myr}^{-1}$ are marked besides. The symbols of black squares, red solid circles, and magenta crosses are the star formation sets of H II regions, IRAS sources, and intersection points between filaments. The red and green intervals mark out the zoomed-in areas in Figure 18

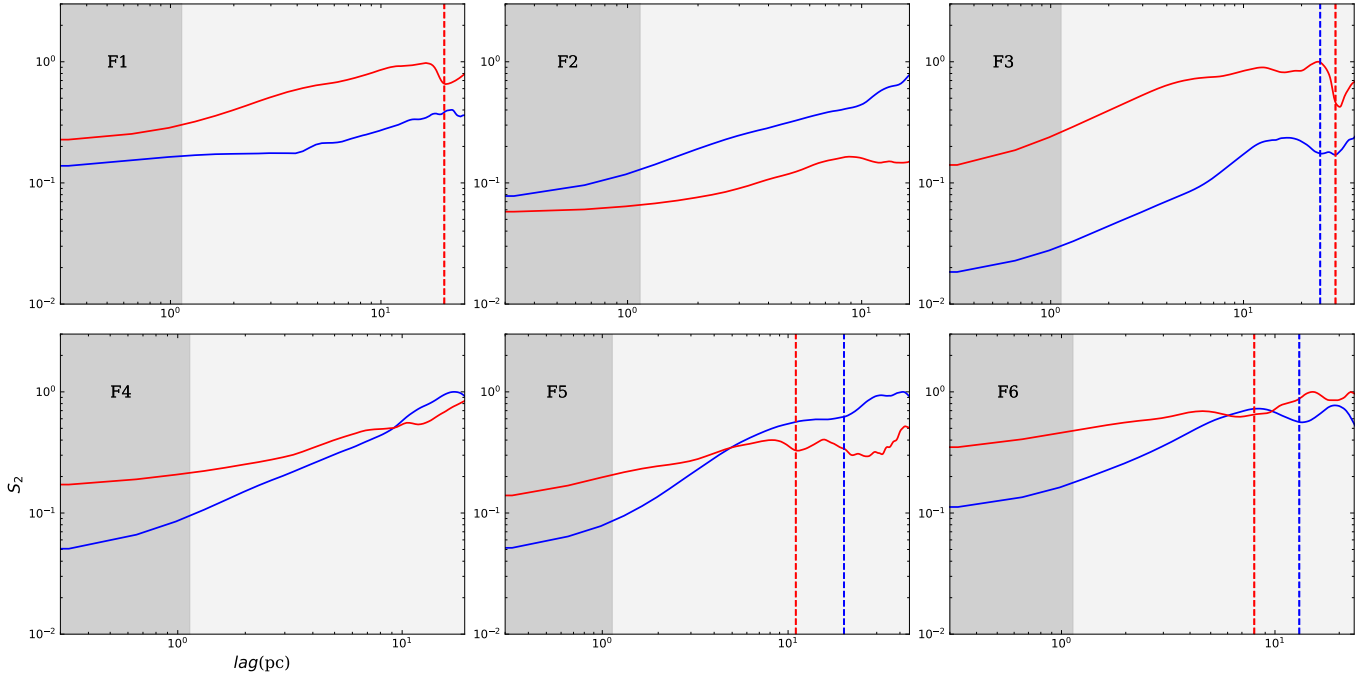


Figure 12. The normalised second-order structure functions of velocity (blue solid lines) and column density (red solid lines). In order to maintain the velocity consistent, the intensity-weighted mean velocity of ^{12}CO along each filament is used to construct the velocity profiles. The column density estimated from ^{13}CO is used to construct the density profile. Pixels above 3σ are kept in the process. The blue and red shaded areas indicate the standard deviation ranges of the structure function profiles. The vertical blue and red dashed lines indicate the potential characteristic length scales of periodic fluctuations in velocity and density. The dark grey shaded area indicates the range of lags below spatial resolution of the data.

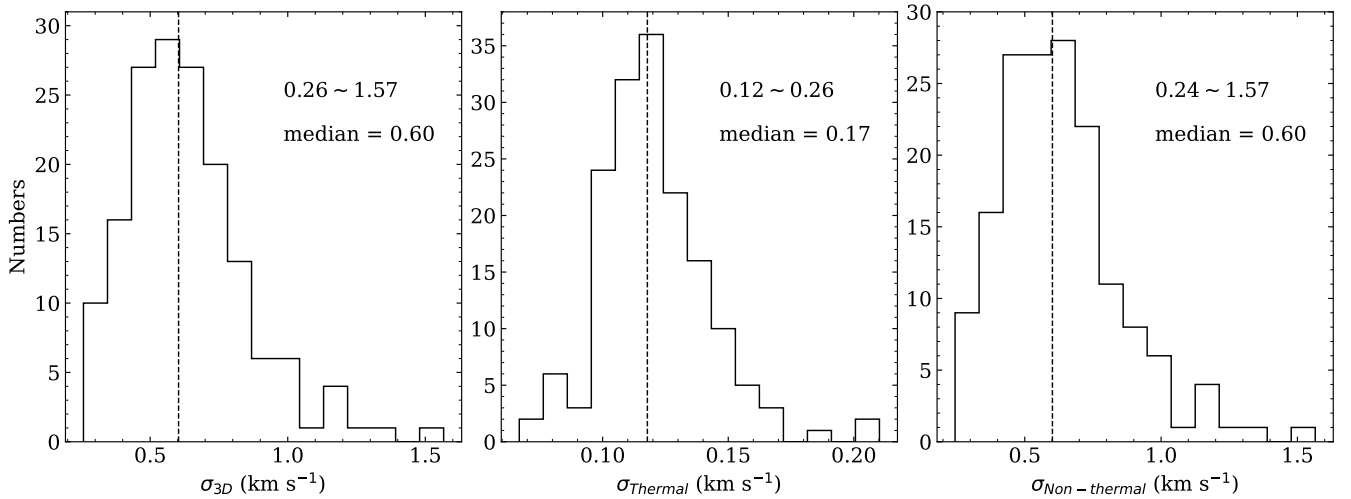


Figure 13. Histogram of three-dimensional velocity dispersion (left panel), the one-dimensional thermal (middle panel) and non-thermal (right panel) velocity dispersions of the ^{13}CO clumps. The range and median values are marked on each panel.

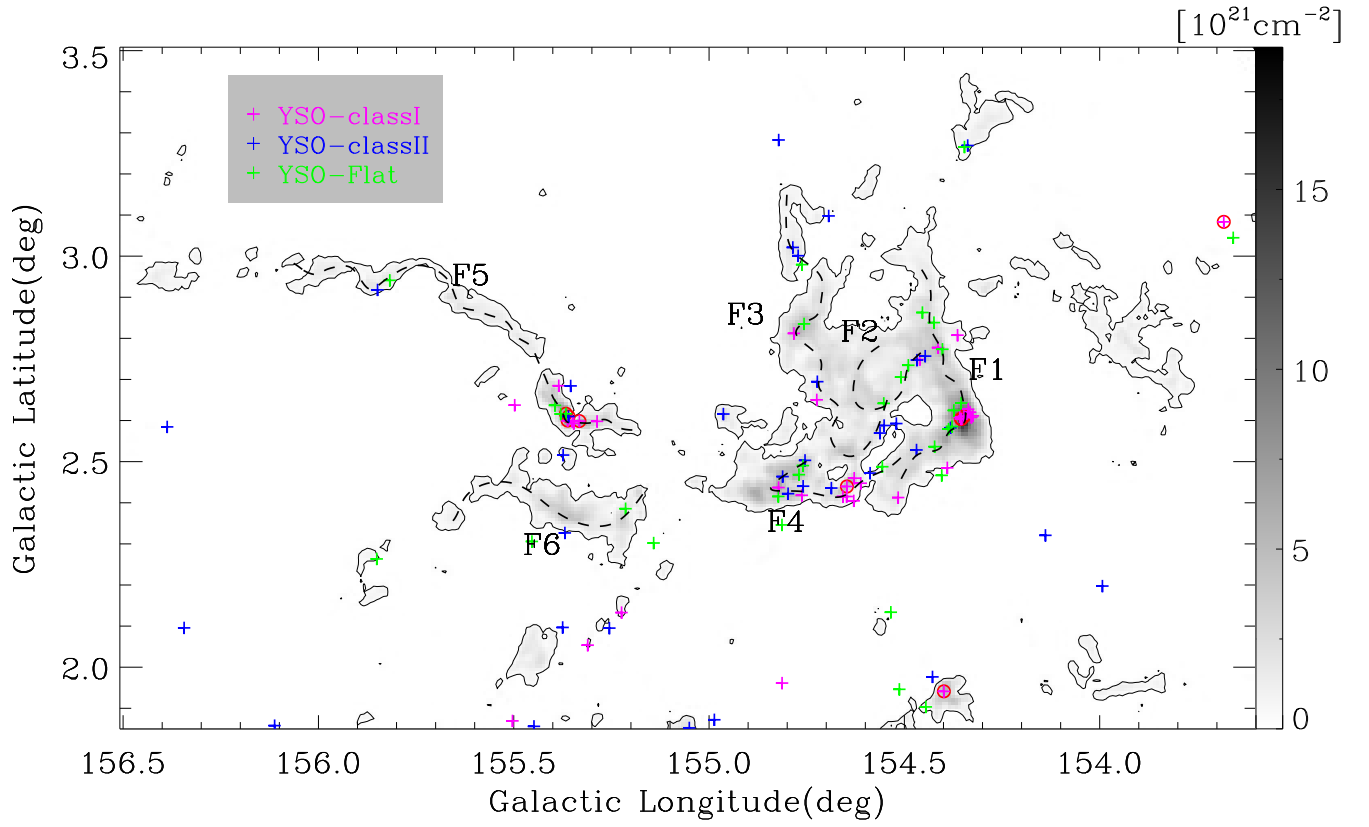


Figure 14. The distribution of the candidate YSOs. The grayscale background is the H_2 column density map estimated from ^{12}CO . The black dashed lines are the filament skeleton identified in Figure 6. The gray contour represents the 3σ boundary of the ^{12}CO emission ($0.2 \times 10^{21} \text{cm}^{-2}$). The magenta, green, and blue crosses represent the candidate YSOs of Class I, the Flat type, and Class II, respectively. The red circle with plus indicates the candidate YSOs with luminosity greater than $100L_{\odot}$.

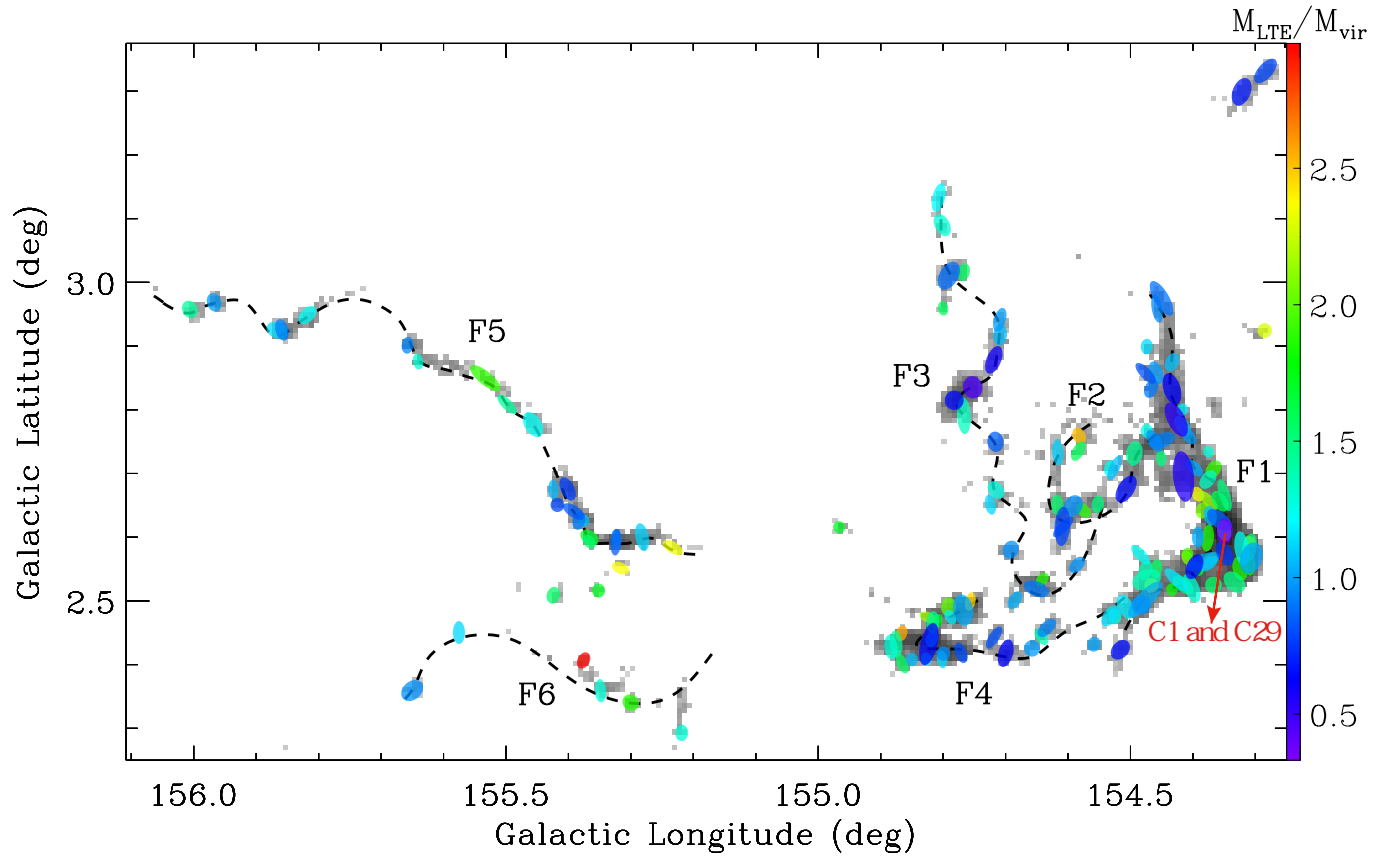


Figure 15. The ^{13}CO velocity-integrated intensity map (moment 0) that overlapped with the clumps colored by α_{vir} . The black dashed lines are same as those in Figure 6.

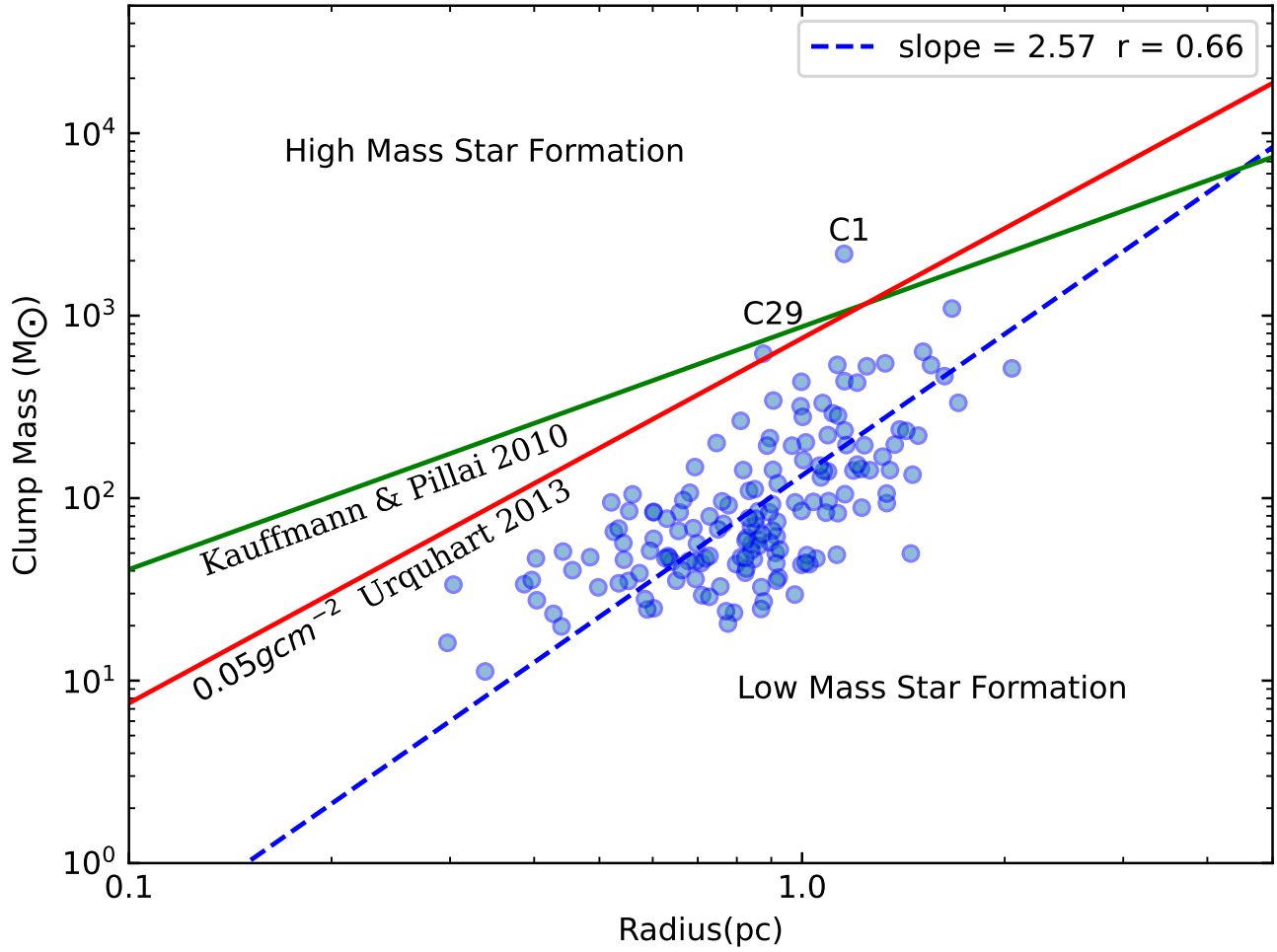


Figure 16. The mass versus radius diagram of ^{13}CO clumps. The green line and red line represent the lower limits of high-mass star formation ($M_c = 870 M_{\odot} (R/\text{pc})^{1.33}$) from Kauffmann et al. (2010) and 0.05 g cm^{-2} from Urquhart et al. (2013). The linear fitted slope and correlation coefficient of the clump sample are labeled in the upper right corner.

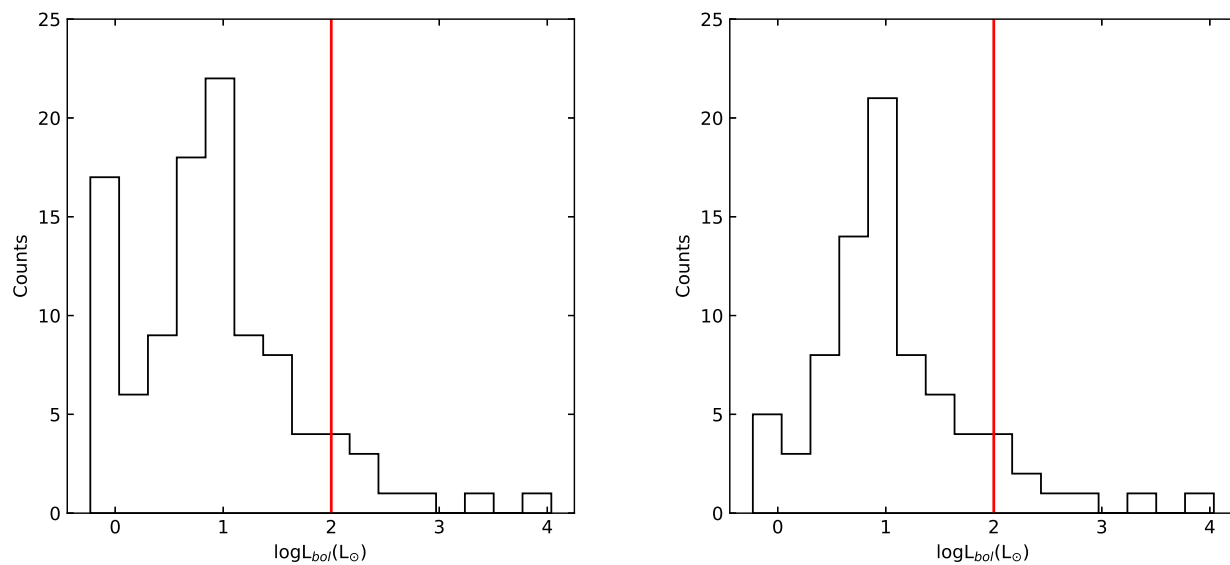


Figure 17. Luminosity function of the YSOs sample (left panel) and the sources that located within the cloud (right panel). The red vertical line is the position $100L_{\odot}$.

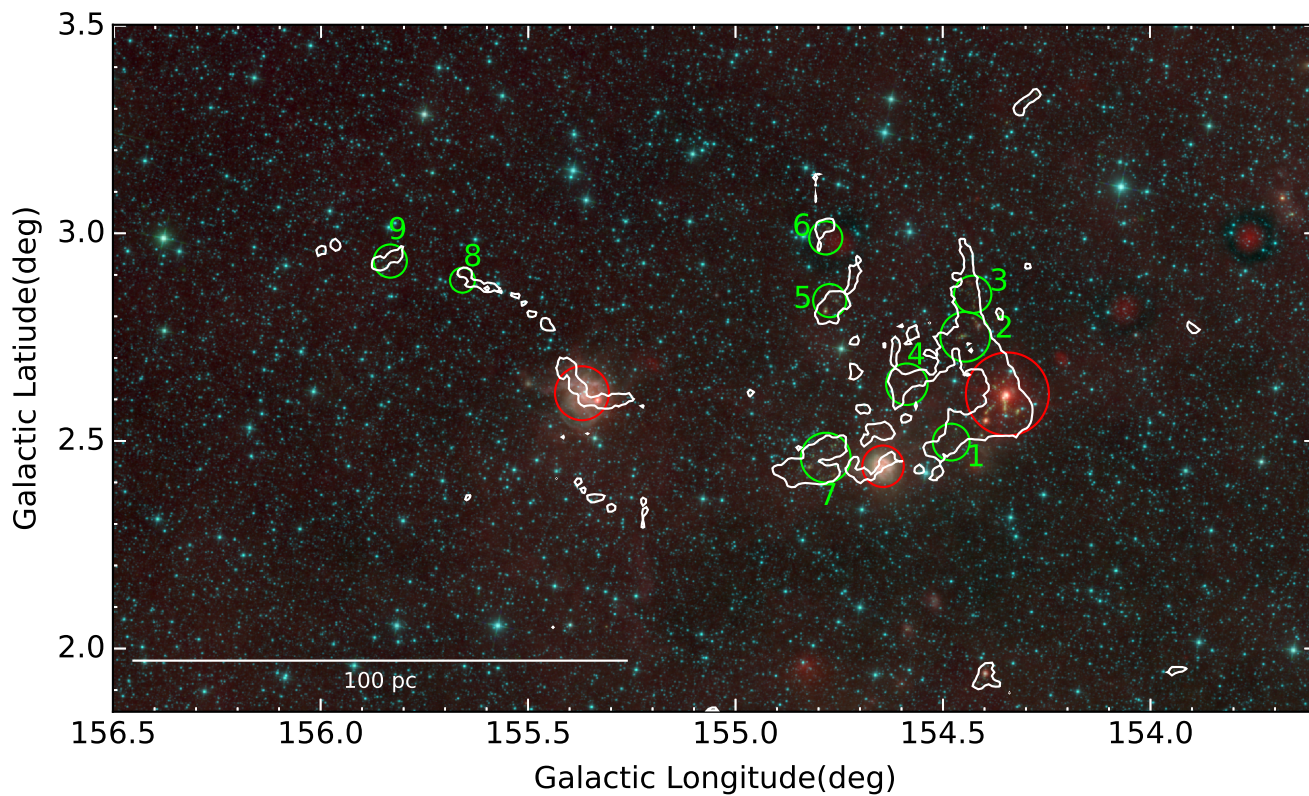


Figure 18. The composite three-color image of three WISE bands ($22\ \mu\text{m}$ in red, $4.6\ \mu\text{m}$ in green, $3.4\ \mu\text{m}$ in blue). The white contour represents the 3σ boundary of the ^{13}CO emission. The red circles are the locations of the three H II regions. The nine green circles indicate the regions where mass-flow activities are detected.

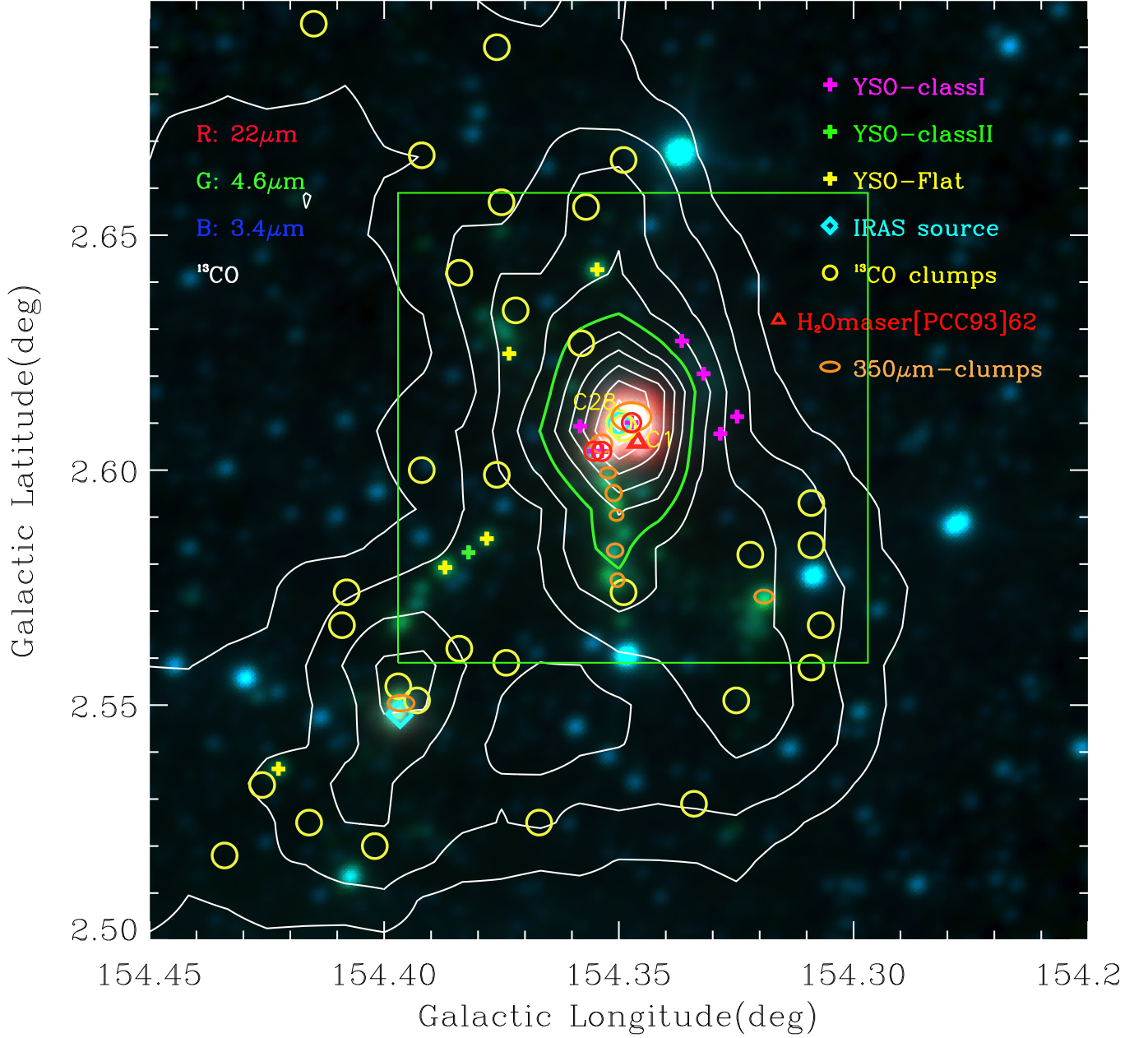


Figure 19. The background is the composite three-color image of three WISE bands ($22 \mu\text{m}$ in red, $4.6 \mu\text{m}$ in green, $3.4 \mu\text{m}$ in blue) toward the zoom-in region of G154.346+02.606. The white contours show the ^{13}CO intensity integrated in the velocity interval of $[-39.5, -33.5] \text{ km s}^{-1}$, which are set from 10σ to the peak value in this region by an 10% average step. The green box is centered at $(l, b) \sim (154^\circ 347', 2^\circ 609')$ with a size of $0^\circ.1 \times 0^\circ.1$. The green contour indicates the region with intensity greater than $12.65 \text{ K km s}^{-1}$, or roughly $N_{\text{H}_2} \gtrsim 6.1 \times 10^{21} \text{ cm}^{-2}$. The magenta, yellow, and green plus signs represent the candidate YSOs of Class I, Class II, and Flat type, respectively. The red circle with plus signs represent the candidate massive YSOs. The yellow circles, cyan diamond, red triangle, and orange ellipses represent the ^{13}CO clumps, IRAS sources, H_2O maser, and the $350 \mu\text{m}$ clumps found out by BGPS, respectively.

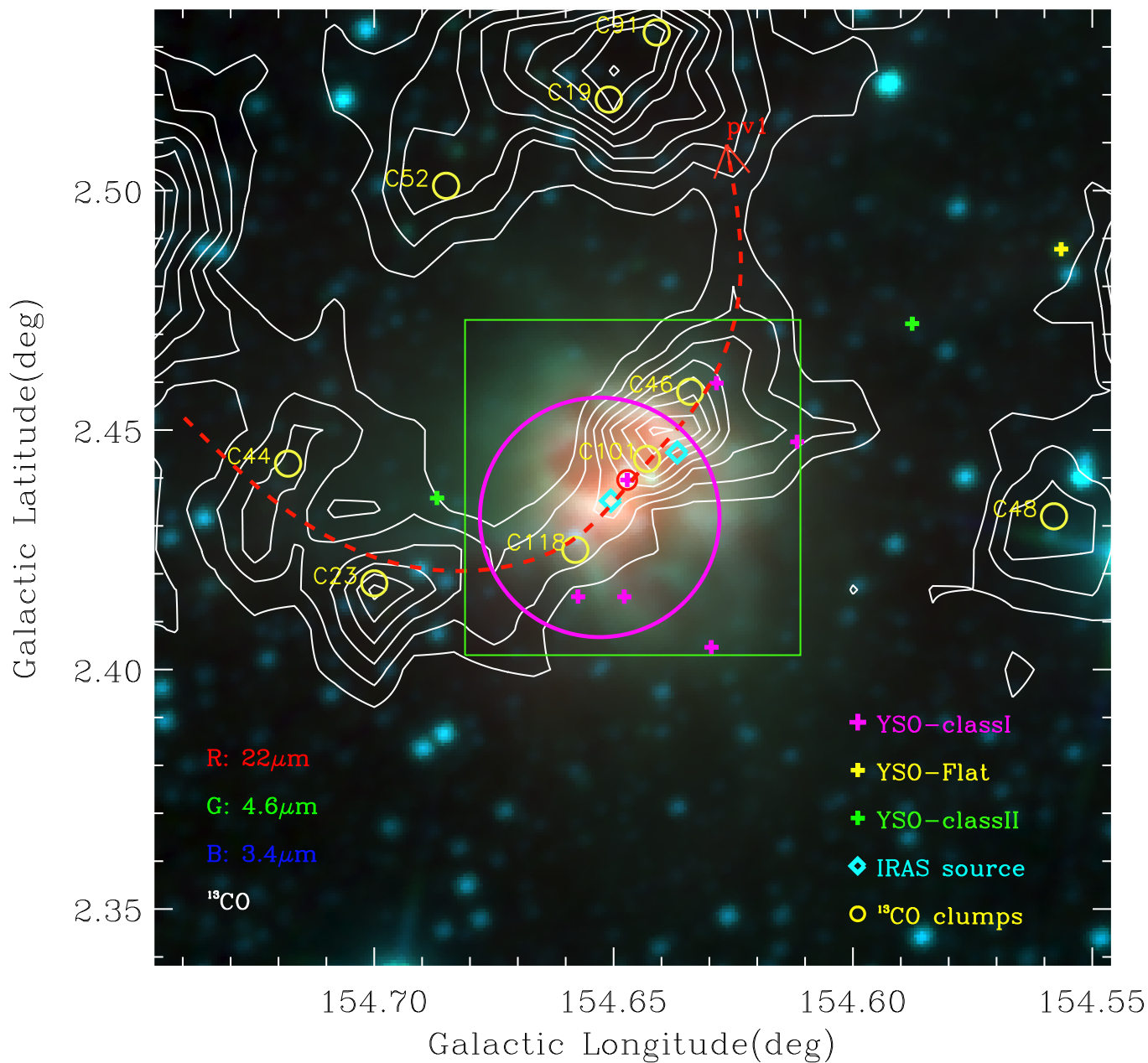


Figure 20. Same as Figure 19 but for the region of SH2-211. The white contours show the ^{13}CO intensity integrated in the velocity interval of $[-39.5, -33.5] \text{ km s}^{-1}$, which are set from 5σ to the peak value in this region by an 10% average step. The green box is centered at $(l, b) \sim (154.646, 2.438)$ with a size of $0.07^\circ \times 0.07^\circ$. The red dotted arrow line indicate the PV slice path (width ~ 2 pixels). The IR bubble is indicated by a magenta circle with a center of $(l, b) \sim (154.653^\circ, 2.432^\circ)$ and a radius of 0.025° .

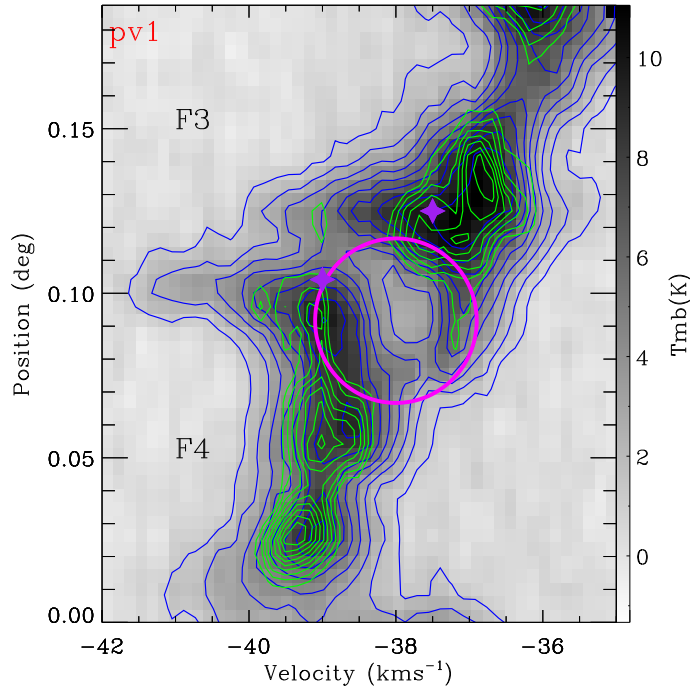


Figure 21. The PV diagram of ¹²CO (grayscale and blue contours) and ¹³CO (green contours) along the PV slice path in Figure 20. The colorbar is in unit of K. The contours are set from 3σ to the peak emission by an average step of 10%. The magenta ellipse is centered at -38 km s^{-1} with velocity radius of 1.5 km s^{-1} and position radius of 0.025 , which is corresponding to the magenta circle in Figure 20.

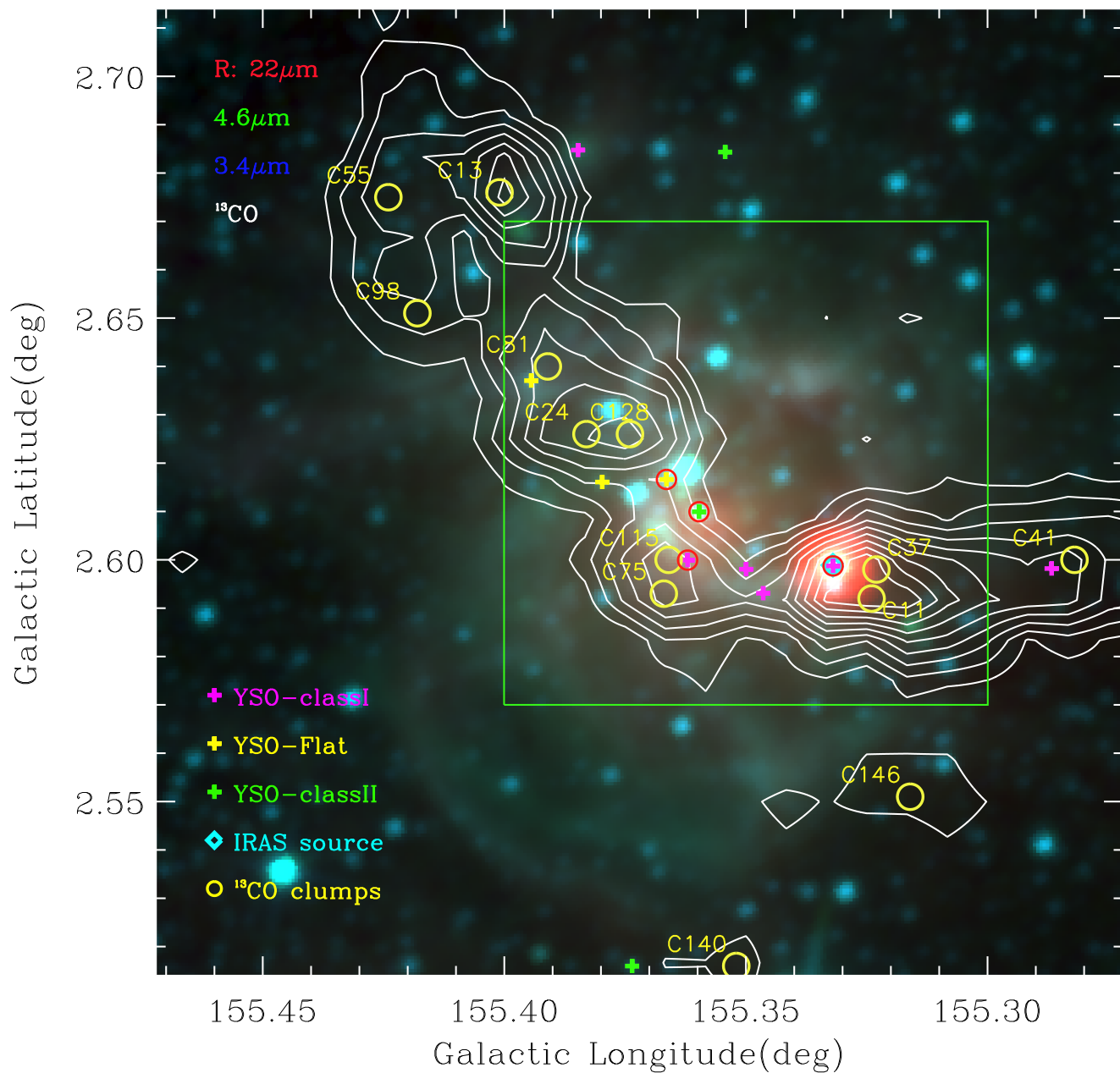


Figure 22. Same as Figure 19 but for the region of SH2-212. The white contours show the ^{13}CO intensity integrated in the velocity interval of $[-39.5, -33.5] \text{ km s}^{-1}$, which are set from 10σ to the peak value in this region by an 10% average step. The green box is centered at $(l, b) \sim (155^\circ 350, 2^\circ 620)$ with a size of $0^\circ.1 \times 0^\circ.1$.

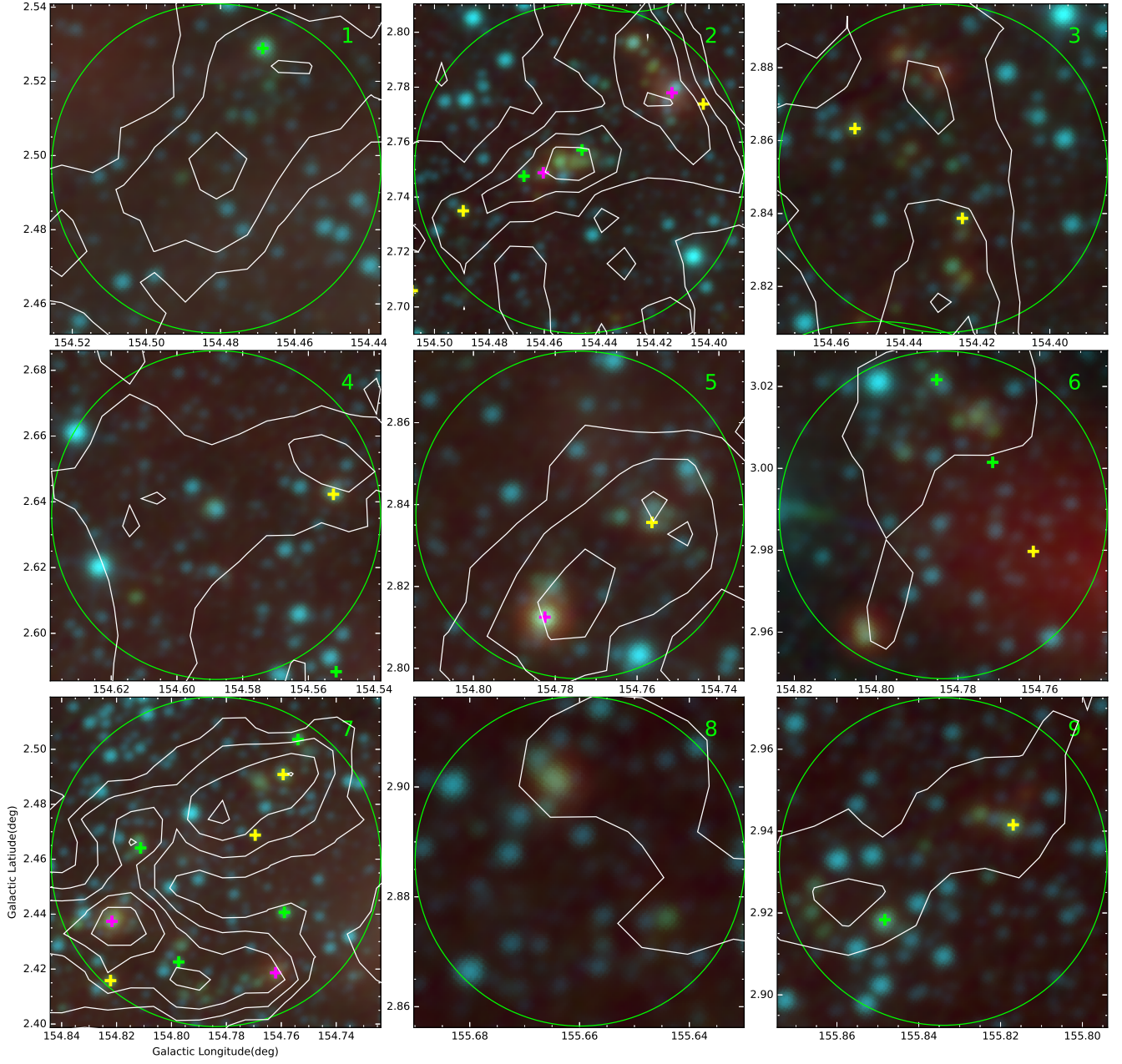


Figure 23. The zoom-in of the nine green circles indicated in Figure 18. The red, yellow, and green crosses represent the candidate YSOs of Class I, Class II, and Flat type, respectively. The red circle with plus signs represent the candidate massive YSOs. The white contours are the ^{13}CO intensity integrated in the velocity interval of $[-39.5, -33.5] \text{ km s}^{-1}$, which are set from 3σ ($1\sigma \sim 0.28 \text{ K km s}^{-1}$) to peak value (27 K km s^{-1}) in a 6% average step.

Table 8. Properties of the identified dense clumps

NO.	Clump	Θ_{maj}	Θ_{min}	PA	v	T_{peak}	ΔV	R_{eff}^a	T_{ex}	τ	N_{H_2}	Σ_c	n_{H_2}	M_{LTE}	M_{vir}	α_{vir}
(1)	(2)	(3)	(4)	(5)	(6)	(7)	(8)	(9)	(10)	(11)	(12)	(13)	(14)	(15)	(16)	(17)
		($'$)	($'$)	($^\circ$)	(kms^{-1})	(K)	(kms^{-1})	(pc)	(K)		(10^{21}cm^{-2})	($\text{M}_\odot \text{pc}^{-2}$)	(10^3cm^{-3})	(M_\odot)	(M_\odot)	
C1	MWISP G154.349	+2.609	1.53	2.40	87.0	-36.36	7.4	1.88	1.08	22.8	0.48	12.10	656.4	2416	800	0.33
C2	MWISP G154.397	+2.554	1.47	2.49	64.4	-36.52	4.0	1.24	1.08	11.4	0.68	2.42	143.5	530	348	0.66
C3	MWISP G154.823	+2.432	4.07	1.63	-14.1	-38.69	4.0	1.58	1.57	12.9	0.53	3.35	161.2	1241	817	0.66
C4	MWISP G154.753	+2.835	2.12	1.86	11.5	-38.19	4.1	0.97	1.13	13.5	0.52	2.23	120.3	484	223	0.46
C5	MWISP G154.427	+2.785	1.67	3.53	117.8	-35.5	3.4	1	1.46	13.2	0.42	1.85	86.5	577	305	0.53
C6	MWISP G154.400	+1.936	1.35	2.20	71.1	-32.38	4.1	1.45	0.94	11.9	0.64	2.97	188.3	518	411	0.79
C7	MWISP G154.782	+2.815	1.82	1.82	55.3	-36.54	3.8	1.11	1.01	11.4	0.63	2.05	124.0	394	259	0.66
C8	MWISP G154.771	+2.419	2.02	1.13	21.7	-38.86	3.7	1.24	0.76	12.1	0.55	2.36	167.0	303	244	0.81
C9	MWISP G154.349	+2.574	1.45	2.45	119.0	-37.19	3.2	1.35	1.06	18.2	0.24	3.08	151.4	532	403	0.76
C10	MWISP G154.449	+2.752	1.34	2.58	19.8	-35.37	3.1	1.18	1.04	11.0	0.50	1.71	95.7	326	303	0.93
C11	MWISP G154.322	+2.582	1.39	3.27	98.3	-34.87	2.8	1.65	1.25	12.7	0.35	2.45	117.2	572	709	1.24
C12	MWISP G155.324	+2.592	2.51	1.04	-4.5	-34.88	3.3	1.3	0.85	15.4	0.32	2.66	155.3	352	300	0.85
C13	MWISP G154.358	+2.627	1.48	2.79	143.8	-33.88	2.9	1.36	1.17	16.4	0.26	2.60	122.3	526	452	0.86
C14	MWISP G155.401	+2.676	1.28	2.37	116.6	-36.02	3.1	0.95	0.95	10.5	0.58	1.35	82.5	234	179	0.77
C15	MWISP G154.434	+2.833	1.63	3.03	108.1	-35.37	2.8	0.78	1.31	10.5	0.48	0.98	48.9	263	167	0.63
C16	MWISP G154.768	+2.486	2.97	1.89	10.7	-38.18	3.2	1.59	1.42	10.5	0.58	2.29	116.4	735	749	1.02
C17	MWISP G154.357	+2.656	1.36	2.18	125.2	-36.02	2.7	1.67	0.93	11.4	0.41	2.19	124.8	341	544	1.59
C18	MWISP G154.415	+2.695	4.78	2.00	6.6	-34.89	2.8	0.89	1.92	10.2	0.50	1.10	49.6	575	318	0.55
C19	MWISP G154.461	+2.751	2.31	1.23	31.6	-36.86	2.8	1.04	0.91	11.0	0.46	1.38	82.3	212	205	0.96
C20	MWISP G154.651	+2.519	1.41	2.53	158.9	-36.52	2.8	1.1	1.06	12.8	0.34	1.62	83.3	294	268	0.91
C21	MWISP G154.816	+2.467	1.25	2.07	86.1	-38.69	2.7	1.41	0.84	10.1	0.50	1.68	107.5	238	349	1.47
C22	MWISP G155.859	+2.925	2.09	1.25	15.8	-35.55	3.0	1.02	0.85	7.9	1.00	1.11	87.7	198	185	0.93
C23	MWISP G154.372	+2.634	1.24	1.86	101.9	-35.2	2.4	0.98	0.77	13.1	0.28	1.26	77.7	143	154	1.07
C24	MWISP G154.700	+2.418	2.65	1.40	-15.8	-39.03	2.7	0.75	1.09	12.7	0.34	1.07	54.1	202	128	0.63
C25	MWISP G155.383	+2.626	1.73	1.20	-11.8	-35.05	2.7	1.12	0.70	16.0	0.24	1.96	128.9	198	184	0.92
C26	MWISP G154.307	+2.567	2.09	3.05	70.5	-33.87	2.8	1.34	1.53	8.9	0.68	1.49	77.1	564	573	1.02
C27	MWISP G154.884	+2.427	2.35	1.28	7.2	-39.52	2.5	1.13	0.94	8.5	0.65	1.09	69.2	193	251	1.30
C28	MWISP G155.658	+2.901	1.60	1.14	-8.3	-37.04	2.7	0.87	0.62	8.5	0.73	0.93	86.5	103	98	0.94
C29	MWISP G154.350	+2.610	1.31	1.92	104.9	-38.02	2.7	2.13	0.82	22.8	0.15	5.02	276.8	586	779	1.33
C30	MWISP G154.552	+2.651	1.63	1.18	-7.3	-35.87	2.6	1.33	0.65	10.6	0.44	1.57	121.0	161	240	1.50
C31	MWISP G154.483	+2.494	1.81	1.87	175.5	-35.21	2.5	0.86	1.02	8.7	0.60	0.84	49.6	163	158	0.97
C32	MWISP G154.719	+2.878	1.40	2.76	67.2	-38.04	2.7	0.63	1.12	10.2	0.49	0.75	40.1	157	93	0.59
C33	MWISP G154.494	+2.732	1.57	2.34	79.8	-36.86	2.3	1.28	1.08	9.9	0.44	1.30	69.1	255	371	1.45
C34	MWISP G154.476	+2.502	1.55	4.47	45.7	-36.37	2.2	1.07	1.60	9.1	0.48	0.98	45.9	369	383	1.04
C35	MWISP G154.609	+2.617	1.48	3.70	86.4	-36.52	2.4	0.81	1.39	9.6	0.47	0.82	39.6	242	191	0.79

Table 8 continued on next page

Table 8 (continued)

NO.	Clump	Θ_{maj}	PA	v	T_{peak}	ΔV	R_{eff}^d	T_{ex}	τ	N_{H_2}	Σ_c	n_{H_2}	M_{LTE}	M_{vir}	α_{vir}	
(1)	(2)	(3)	(4)	(5)	(6)	(7)	(8)	(9)	(10)	(11)	(12)	(13)	(14)	(15)	(16)	(17)
		($'$)	($'$)	($^\circ$)	(kms^{-1})	(K)	(kms^{-1})	(pc)	(K)	(10^{21}cm^{-2})	($M_\odot \text{pc}^{-2}$)	(10^3cm^{-3})	(M_\odot)	(M_\odot)		
C36	MWISP G154.516	+2.423	1.55	2.11	44.9	-39.18	2.6	0.66	1.00	11.0	0.41	0.81	44.4	139	91	0.65
C37	MWISP G154.384	+2.562	1.38	3.48	20.9	-35.7	1.9	0.89	1.29	11.6	0.26	0.83	37.7	196	213	1.09
C38	MWISP G155.323	+2.598	1.72	0.97	4.1	-36.03	2.5	0.88	0.56	11.0	0.39	1.02	89.2	89	91	1.02
C39	MWISP G154.507	+2.676	1.57	2.86	57.1	-37.68	2.4	0.67	1.23	11.0	0.38	0.76	37.2	178	116	0.65
C40	MWISP G154.788	+2.474	0.99	1.50	119.7	-40.84	2.5	1.08	0.49	11.1	0.39	1.29	134.8	101	119	1.18
C41	MWISP G155.818	+2.949	1.29	2.08	42.8	-36.04	2.4	0.99	0.86	8.2	0.67	0.92	62.2	145	177	1.22
C42	MWISP G155.282	+2.600	2.66	1.27	11.5	-36.19	2.5	1.11	1.02	11.1	0.39	1.33	71.4	235	264	1.12
C43	MWISP G154.402	+2.520	2.86	1.42	22.2	-34.87	2.3	1.09	1.16	8.7	0.53	0.97	52.3	221	288	1.30
C44	MWISP G154.791	+3.010	1.79	2.87	58.8	-35.53	2.5	0.91	1.34	9.3	0.52	0.93	46.8	264	232	0.88
C45	MWISP G154.718	+2.443	0.98	2.41	56.4	-39.35	2.4	0.75	0.78	12.5	0.31	0.94	58.2	112	92	0.82
C46	MWISP G155.967	+2.969	1.79	1.37	19.0	-36.7	2.5	0.82	0.81	7.2	0.94	0.70	56.3	115	113	0.98
C47	MWISP G154.634	+2.458	1.17	2.17	44.2	-36.71	2.5	1.02	0.83	15.0	0.24	1.55	88.3	192	181	0.94
C48	MWISP G154.376	+2.599	1.18	2.54	82.9	-35.87	2.1	1.6	0.94	14.1	0.21	1.89	98.1	272	503	1.85
C49	MWISP G154.558	+2.432	1.27	1.42	69.1	-37.19	2.4	0.78	0.61	8.6	0.60	0.74	65.1	77	78	1.01
C50	MWISP G154.802	+2.408	1.68	1.00	7.1	-38.36	2.2	0.9	0.56	12.1	0.29	1.01	84.7	85	96	1.13
C51	MWISP G153.948	+1.943	2.60	1.11	15.2	-36.04	2.4	0.77	0.92	7.6	0.81	0.67	46.1	121	113	0.93
C52	MWISP G155.641	+2.876	1.52	0.98	11.3	-37.03	2.3	0.99	0.49	8.3	0.62	0.89	101.2	77	101	1.31
C53	MWISP G154.284	+3.332	1.41	2.83	47.7	-36.68	2.4	0.72	1.15	9.7	0.46	0.73	38.3	158	124	0.79
C54	MWISP G154.685	+2.501	1.15	1.89	56.5	-36.7	2.3	0.81	0.73	10.5	0.39	0.86	58.0	97	100	1.03
C55	MWISP G154.349	+2.666	1.06	3.14	107.7	-35.03	2.0	1.03	1.01	9.6	0.38	0.87	46.4	149	224	1.50
C56	MWISP G154.417	+1.910	1.15	1.36	47.9	-33.21	2.4	0.96	0.52	11.5	0.34	1.11	104.2	88	100	1.13
C57	MWISP G154.426	+2.533	1.12	3.02	137.7	-36.36	1.9	0.74	1.03	9.4	0.36	0.58	30.5	101	117	1.17
C58	MWISP G155.424	+2.675	1.01	1.86	92.7	-35.37	2.3	0.92	0.64	13.3	0.26	1.15	83.4	107	113	1.06
C59	MWISP G154.322	+3.299	1.71	2.74	67.3	-36.19	2.3	0.63	1.27	9.9	0.41	0.62	30.3	153	105	0.69
C60	MWISP G154.865	+2.401	1.95	1.04	25.4	-39.35	2.0	0.97	0.68	9.1	0.42	0.80	58.3	86	134	1.57
C61	MWISP G154.367	+2.707	1.83	1.32	-40.6	-36.19	2.0	1.19	0.80	8.6	0.48	0.94	62.0	124	236	1.90
C62	MWISP G154.525	+2.476	1.52	1.26	16.1	-35.38	2.1	0.84	0.65	9.0	0.46	0.73	57.3	75	95	1.27
C63	MWISP G154.827	+2.409	1.23	1.03	15.3	-38.36	1.9	0.84	0.38	10.8	0.30	0.75	106.1	47	56	1.17
C64	MWISP G154.325	+2.551	1.43	2.28	104.9	-36.36	1.9	1.18	1.00	9.8	0.34	0.94	50.1	156	290	1.86
C65	MWISP G154.800	+2.418	1.32	1.32	136.2	-39.35	1.9	0.61	0.59	11.2	0.28	0.56	43.9	48	46	0.95
C66	MWISP G154.585	+2.557	1.16	1.84	44.5	-37.68	2.1	0.69	0.72	11.3	0.30	0.69	45.7	74	71	0.97
C67	MWISP G154.692	+2.580	1.77	1.51	-26.9	-36.52	2.1	0.73	0.86	6.0	1.38	0.47	43.1	100	96	0.96
C68	MWISP G154.709	+2.918	1.32	2.02	83.5	-37.37	2.1	0.7	0.86	8.4	0.53	0.57	36.0	84	88	1.05
C69	MWISP G154.533	+2.477	2.26	1.32	-36.4	-37.86	2.0	0.74	0.94	8.6	0.47	0.58	34.0	94	107	1.14
C70	MWISP G154.398	+2.709	1.11	2.15	138.7	-34.04	1.9	0.6	0.79	9.7	0.34	0.48	29.8	58	59	1.02
C71	MWISP G153.893	+2.767	1.09	2.89	151.1	-34.87	2.1	0.82	0.97	7.7	0.61	0.62	37.5	112	137	1.22
C72	MWISP G154.407	+2.759	1.11	1.89	132.6	-34.04	1.9	0.67	0.70	12.5	0.23	0.66	42.5	66	66	1.00

Table 8 continued on next page

Table 8 (continued)

NO.	Clump	Θ_{maj}	Θ_{min}	PA	v	T_{peak}	ΔV	R_{eff}^{θ}	T_{ex}	τ	N_{H_2}	Σ_c	n_{H_2}	M_{LTE}	M_{vir}	α_{vir}	
(1)	(2)	(3)	(4)	(5)	(6)	(7)	(8)	(9)	(10)	(11)	(12)	(13)	(14)	(15)	(16)	(17)	
		($'$)	($'$)	($^{\circ}$)	(kms^{-1})	(K)	(kms^{-1})	(pc)	(K)		(10^{21}cm^{-2})	($M_{\odot} \text{pc}^{-2}$)	(10^3cm^{-3})	(M_{\odot})	(M_{\odot})		
C73	MWISP	G154.616	+2.733	1.09	2.44	94.7	-36.36	1.7	0.57	0.86	8.8	0.36	0.39	22.8	52	58	1.11
C74	MWISP	G154.715	+2.674	1.37	1.88	130.6	-37.2	2.0	0.81	0.84	9.0	0.43	0.66	41.0	91	115	1.27
C75	MWISP	G154.476	+2.548	1.29	1.89	72.1	-35.22	1.8	0.78	0.80	9.4	0.34	0.59	36.4	73	102	1.39
C76	MWISP	G154.818	+2.440	1.11	1.60	70.9	-39.52	1.8	0.63	0.60	10.5	0.29	0.51	40.0	45	50	1.10
C77	MWISP	G155.349	+2.359	2.19	1.07	3.8	-36.2	1.9	0.74	0.78	8.0	0.52	0.53	36.2	68	89	1.30
C78	MWISP	G154.850	+2.408	1.26	1.15	18.1	-38.35	1.8	0.61	0.47	9.2	0.36	0.46	49.6	34	36	1.07
C79	MWISP	G155.367	+2.593	1.07	1.47	130.6	-35.04	2.0	1.2	0.53	13.5	0.22	1.35	118.8	103	158	1.54
C80	MWISP	G155.498	+2.809	0.98	2.43	135.8	-37.03	2.0	0.84	0.79	7.6	0.60	0.59	41.7	81	116	1.43
C81	MWISP	G155.457	+2.777	1.62	2.60	123.5	-37.52	2.0	0.89	1.18	8.4	0.50	0.69	36.2	159	196	1.23
C82	MWISP	G154.967	+2.616	1.18	1.13	59.1	-39.19	2.0	1.13	0.41	6.9	0.80	0.78	121.0	65	110	1.70
C83	MWISP	G154.393	+2.551	1.12	1.50	119.6	-37.69	1.7	0.92	0.56	10.8	0.26	0.73	59.7	60	100	1.67
C84	MWISP	G154.375	+1.916	1.33	1.33	-5.7	-31.05	1.9	0.92	0.59	6.0	1.13	0.55	62.4	69	105	1.52
C85	MWISP	G154.534	+2.708	1.55	1.00	-13.0	-36.52	1.7	0.64	0.52	9.7	0.30	0.46	42.5	36	44	1.24
C86	MWISP	G155.391	+2.640	1.10	2.36	148.1	-35.71	1.9	0.65	0.85	14.4	0.19	0.72	39.7	89	75	0.84
C87	MWISP	G154.376	+2.690	1.30	2.01	49.8	-35.21	1.7	0.72	0.85	9.4	0.33	0.52	30.3	68	92	1.34
C88	MWISP	G154.334	+2.529	1.66	2.37	138.6	-34.71	1.8	0.99	1.13	10.3	0.29	0.79	38.4	155	232	1.50
C89	MWISP	G154.591	+2.649	1.71	2.08	59.7	-35.38	1.8	0.61	1.06	9.6	0.34	0.47	24.3	86	82	0.96
C90	MWISP	G154.367	+2.525	1.61	1.61	-2.9	-36.52	1.6	0.74	0.84	7.9	0.43	0.45	27.9	62	96	1.55
C91	MWISP	G154.451	+2.724	1.00	1.54	94.8	-35.2	1.7	0.82	0.51	9.7	0.31	0.61	57.7	47	72	1.52
C92	MWISP	G154.716	+2.750	1.93	1.55	8.1	-37.2	1.7	0.45	0.94	8.2	0.43	0.29	16.9	47	40	0.85
C93	MWISP	G154.484	+2.573	1.02	2.36	134.5	-35.87	1.8	0.63	0.80	7.2	0.58	0.39	27.0	54	66	1.23
C94	MWISP	G154.807	+3.133	1.21	2.77	75.6	-34.54	1.8	0.72	1.02	8.2	0.46	0.51	28.1	91	110	1.21
C95	MWISP	G154.458	+2.959	1.01	2.68	100.9	-35.86	1.7	0.53	0.87	9.6	0.32	0.39	22.6	54	51	0.95
C96	MWISP	G154.641	+2.533	1.02	1.49	46.9	-37.69	1.9	1.13	0.50	9.5	0.37	0.91	90.8	71	134	1.87
C97	MWISP	G154.433	+2.875	1.83	1.27	-26.8	-35.37	1.6	0.52	0.77	8.8	0.35	0.34	21.8	41	44	1.07
C98	MWISP	G156.006	+2.958	1.70	1.44	30.5	-35.86	1.8	0.76	0.80	7.4	0.57	0.49	33.5	68	97	1.42
C99	MWISP	G154.724	+2.651	1.90	1.04	12.1	-38.02	1.9	0.62	0.66	8.7	0.42	0.46	34.3	47	53	1.12
C100	MWISP	G154.384	+2.642	1.58	1.34	-25.6	-36.69	1.6	1.14	0.71	11.8	0.21	0.92	58.5	94	194	2.07
C101	MWISP	G154.476	+2.857	1.04	2.57	135.3	-34.71	1.7	0.42	0.87	8.6	0.38	0.28	16.5	39	32	0.82
C102	MWISP	G154.474	+2.767	1.32	1.15	5.6	-37.36	1.7	0.65	0.50	9.1	0.34	0.46	45.0	35	44	1.25
C103	MWISP	G155.418	+2.651	1.32	1.32	141.7	-36.69	1.8	0.54	0.59	13.4	0.20	0.55	41.9	45	36	0.79
C104	MWISP	G154.800	+2.959	1.00	1.36	98.8	-36.03	1.8	0.89	0.43	7.9	0.49	0.60	78.0	45	71	1.58
C105	MWISP	G155.650	+2.359	1.73	2.32	39.3	-37.19	1.9	0.62	1.15	8.5	0.44	0.45	23.2	96	92	0.96
C106	MWISP	G154.183	+2.959	1.15	1.01	12.5	-34.53	1.8	0.35	0.32	6.1	0.90	0.20	47.4	15	8	0.54
C107	MWISP	G154.643	+2.444	1.76	1.05	35.9	-37.69	1.8	0.99	0.62	14.7	0.18	1.08	76.3	94	128	1.37
C108	MWISP	G155.219	+2.293	1.24	1.55	87.7	-36.36	1.7	0.62	0.65	7.6	0.50	0.38	30.3	40	52	1.30
C109	MWISP	G154.409	+2.567	1.49	1.03	27.7	-37.36	1.5	1.05	0.51	11.5	0.20	0.75	67.6	55	117	2.13

Table 8 continued on next page

Table 8 (continued)

NO.	Clump	Θ_{maj}	PA	v	T_{peak}	ΔV	R_{eff}^{θ}	T_{ex}	τ	N_{H_2}	Σ_c	n_{H_2}	M_{LTE}	M_{vir}	α_{vir}			
(1)	(2)	(3)	(4)	(5)	(6)	(7)	(8)	(9)	(10)	(11)	(12)	(13)	(14)	(15)	(16)	(17)		
		($'$)	($'$)	($'$)	(kms^{-1})	(K)	(kms^{-1})	(pc)	(K)	(10^{21}cm^{-2})	($M_{\odot} \text{pc}^{-2}$)	(10^3cm^{-3})	(M_{\odot})	(M_{\odot})				
C110	MWISP	G154.309	+2.584	1.38	2.67	79.3	-32.39	1.7	0.85	1.09	9.1	0.33	0.58	29.4	0.29	109	164	1.51
C111	MWISP	G154.417	+2.800	1.18	1.11	-24.9	-34.04	1.6	0.58	0.40	8.8	0.33	0.36	47.5	1.28	24	28	1.18
C112	MWISP	G154.810	+2.468	0.97	1.46	64.3	-35.54	1.7	0.94	0.45	9.7	0.31	0.68	74.9	1.78	49	84	1.73
C113	MWISP	G154.583	+2.735	1.11	2.02	58.9	-36.69	1.5	0.67	0.75	9.0	0.29	0.39	25.1	0.36	44	70	1.59
C114	MWISP	G154.525	+2.709	0.98	2.53	65.4	-36.03	1.5	0.46	0.82	8.3	0.36	0.27	16.3	0.22	34	36	1.06
C115	MWISP	G154.392	+2.600	1.17	2.00	90.0	-36.69	1.4	0.5	0.77	11.7	0.19	0.36	21.0	0.29	40	40	1.02
C116	MWISP	G155.300	+2.340	1.49	1.65	139.1	-35.86	1.6	0.86	0.81	6.4	0.71	0.45	32.7	0.44	67	125	1.86
C117	MWISP	G154.466	+2.524	1.40	1.39	-22.9	-37.19	1.5	0.97	0.65	9.4	0.27	0.59	42.1	0.69	57	129	2.27
C118	MWISP	G154.756	+2.499	0.98	1.78	77.1	-36.53	1.7	1.26	0.59	9.3	0.33	0.90	72.8	1.33	80	196	2.46
C119	MWISP	G154.474	+2.533	1.87	2.83	19.9	-35.7	1.5	0.81	1.37	9.2	0.30	0.52	23.3	0.18	137	188	1.37
C120	MWISP	G154.474	+2.899	1.14	1.47	86.8	-35.7	1.6	0.51	0.56	7.8	0.44	0.30	27.0	0.52	27	31	1.14
C121	MWISP	G155.366	+2.600	1.28	1.90	149.0	-33.87	1.7	0.9	0.80	9.4	0.33	0.65	39.5	0.53	79	135	1.70
C122	MWISP	G154.434	+2.518	1.17	1.08	15.9	-36.69	1.5	0.81	0.38	8.0	0.37	0.44	64.5	1.84	29	52	1.79
C123	MWISP	G154.617	+2.651	1.18	1.93	92.8	-36.69	1.5	0.68	0.76	9.5	0.27	0.42	26.2	0.37	48	74	1.54
C124	MWISP	G154.658	+2.425	1.55	1.54	-22.2	-39.19	1.6	0.55	0.79	12.1	0.20	0.44	25.7	0.35	50	50	0.99
C125	MWISP	G154.342	+1.892	1.06	1.25	89.8	-31.38	1.7	0.6	0.41	5.7	1.11	0.30	54.1	1.42	29	31	1.08
C126	MWISP	G154.309	+2.558	1.04	2.23	91.3	-35.53	1.4	0.74	0.77	8.4	0.33	0.41	25.9	0.36	48	88	1.82
C127	MWISP	G154.374	+2.559	1.08	1.95	36.5	-36.37	1.3	0.48	0.71	12.6	0.15	0.32	19.6	0.30	31	34	1.10
C128	MWISP	G154.801	+3.090	1.42	2.25	118.8	-35.2	1.6	0.63	0.98	5.7	0.91	0.30	20.6	0.23	63	82	1.30
C129	MWISP	G154.709	+2.941	1.14	2.32	72.6	-37.85	1.6	0.46	0.86	7.8	0.44	0.27	16.5	0.21	38	38	0.99
C130	MWISP	G154.408	+2.574	1.10	1.13	85.8	-36.2	1.3	0.92	0.36	10.5	0.20	0.55	79.4	2.37	33	64	1.96
C131	MWISP	G154.508	+2.491	2.44	1.45	26.6	-37.04	1.4	0.52	1.06	8.2	0.34	0.28	14.5	0.15	51	60	1.18
C132	MWISP	G154.767	+2.791	3.47	1.32	3.3	-36.03	1.4	0.69	1.25	10.1	0.22	0.42	18.7	0.16	92	125	1.35
C133	MWISP	G154.309	+2.593	1.02	1.23	136.6	-35.2	1.4	1.04	0.37	8.5	0.31	0.58	83.8	2.43	36	84	2.31
C134	MWISP	G154.608	+2.616	0.97	2.59	44.7	-36.03	1.4	0.36	0.82	9.6	0.26	0.22	12.7	0.17	27	22	0.82
C135	MWISP	G155.374	+2.626	0.99	1.14	93.6	-36.19	1.6	0.77	0.28	11.7	0.21	0.61	128.7	4.89	33	35	1.08
C136	MWISP	G154.375	+2.734	1.01	1.10	121.6	-35.37	1.4	0.62	0.28	7.2	0.41	0.29	70.8	2.75	17	22	1.30
C137	MWISP	G154.375	+2.657	1.01	2.34	134.7	-32.04	1.5	1	0.78	10.7	0.22	0.67	39.6	0.55	76	163	2.15
C138	MWISP	G154.392	+2.667	1.13	1.47	119.1	-34.04	1.4	1.01	0.56	10.6	0.20	0.63	51.2	0.99	50	119	2.38
C139	MWISP	G154.285	+2.924	1.39	1.39	86.5	-31.21	1.5	0.91	0.65	7.3	0.46	0.48	37.0	0.61	49	113	2.28
C140	MWISP	G154.582	+2.759	1.64	1.22	28.0	-36.36	1.3	0.91	0.67	9.1	0.25	0.48	32.5	0.52	46	117	2.52
C141	MWISP	G154.467	+2.833	1.82	1.22	-25.7	-34.87	1.4	0.37	0.74	9.5	0.25	0.22	13.5	0.20	23	21	0.91
C142	MWISP	G155.867	+2.925	1.50	2.06	157.1	-36.04	1.5	0.51	0.96	8.0	0.38	0.29	15.8	0.18	46	52	1.14
C143	MWISP	G155.424	+2.509	1.26	1.61	71.0	-33.87	1.6	0.73	0.68	9.5	0.29	0.48	33.3	0.53	49	76	1.56
C144	MWISP	G154.201	+2.990	2.21	0.98	-10.9	-34.7	1.5	0.48	0.73	4.6	3.36	0.19	37.8	0.56	63	35	0.56
C145	MWISP	G154.416	+2.525	1.31	2.34	141.0	-37.52	1.3	0.62	0.95	8.5	0.29	0.32	17.3	0.20	49	77	1.55
C146	MWISP	G155.533	+2.850	1.28	3.60	141.6	-37.86	1.4	0.9	1.25	7.7	0.38	0.47	22.7	0.20	112	212	1.89

Table 8 continued on next page

Table 8 (continued)

NO.	Clump	Θ_{maj}	PA	v	T_{peak}	ΔV	R_{eff}^a	T_{ex}	τ	N_{H_2}	Σ_c	n_{H_2}	M_{LTE}	M_{vir}	α_{vir}			
(1)	(2)	(3)	(4)	(5)	(6)	(7)	(8)	(9)	(10)	(11)	(12)	(13)	(14)	(15)	(16)	(17)		
		($'$)	($'$)	($'$)	(kms^{-1})	(K)	(kms^{-1})	(pc)	(K)	(10^{21}cm^{-2})	($M_{\odot} \text{pc}^{-2}$)	(10^3cm^{-3})	(M_{\odot})	(M_{\odot})				
C147	MWISP	G154.791	+2.491	1.75	1.43	-7.6	-39.68	1.4	0.86	0.82	9.5	0.26	0.51	29.9	0.40	63	126	2.01
C148	MWISP	G153.900	+1.957	1.08	1.99	50.8	-35.37	1.4	0.54	0.72	5.5	0.90	0.23	19.5	0.29	32	44	1.38
C149	MWISP	G155.352	+2.516	1.25	1.31	95.8	-34.04	1.4	0.79	0.55	4.9	1.52	0.30	43.8	0.86	42	72	1.72
C150	MWISP	G155.233	+2.584	1.08	2.15	150.6	-36.86	1.5	0.94	0.77	8.1	0.36	0.51	32.6	0.46	61	143	2.33
C151	MWISP	G154.767	+3.016	1.15	1.71	74.5	-36.2	1.5	0.6	0.67	7.3	0.44	0.30	22.9	0.37	32	50	1.57
C152	MWISP	G155.376	+2.407	1.15	1.63	59.7	-34.87	1.3	1.03	0.64	7.4	0.38	0.49	37.5	0.64	48	141	2.96
C153	MWISP	G154.825	+2.474	0.97	1.66	160.2	-37.69	1.4	0.86	0.54	9.4	0.25	0.49	42.5	0.85	39	83	2.15
C154	MWISP	G154.575	+2.642	1.11	1.62	137.2	-37.03	1.3	0.71	0.61	10.1	0.20	0.40	29.4	0.52	34	64	1.87
C155	MWISP	G155.316	+2.551	1.05	1.75	156.7	-34.87	1.4	0.88	0.62	7.8	0.37	0.45	35.0	0.61	42	101	2.37
C156	MWISP	G154.458	+2.551	1.85	1.09	-7.0	-36.69	1.3	0.56	0.68	9.1	0.24	0.29	19.5	0.31	29	45	1.57
C157	MWISP	G154.459	+2.858	2.22	1.30	19.3	-35.37	1.3	0.39	0.91	9.2	0.24	0.21	11.2	0.13	29	29	0.99
C158	MWISP	G155.575	+2.450	2.16	1.15	0.3	-35.21	1.5	0.44	0.81	6.2	0.64	0.20	14.1	0.19	29	33	1.12
C159	MWISP	G154.875	+2.433	2.54	1.20	5.0	-40.35	1.3	0.56	0.95	9.5	0.23	0.30	15.3	0.17	43	62	1.43
C160	MWISP	G154.450	+2.975	1.41	3.72	121.0	-35.36	1.3	0.4	1.36	7.9	0.33	0.19	8.8	0.07	51	45	0.89
C161	MWISP	G154.866	+2.449	1.51	1.08	-17.0	-39.19	1.2	0.81	0.55	7.3	0.36	0.35	31.0	0.61	29	75	2.57
C162	MWISP	G154.417	+2.775	1.27	2.09	126.5	-36.2	1.2	0.5	0.86	14.0	0.12	0.34	17.7	0.22	41	45	1.10

^a Deconvolution radius: $R_{\text{eff}} = \frac{1}{2} \times d \times \frac{\pi}{2} \sqrt{\Theta_{\text{maj}} \Theta_{\text{min}} - \theta_{\text{beam}}^2}$.

Table 9. Infrared Photometric Magnitudes of Candidate YSOs

allwise	<i>l</i>	<i>b</i>	<i>W1</i> (3.4 μm)	<i>W2</i> (4.6 μm)	<i>W3</i> (12 μm)	<i>W4</i> (22 μm)	<i>J</i> (1.25 μm)	<i>H</i> (1.65 μm)	<i>K_s</i> (2.16 μm)	FROM <i>d</i>	GAIA_SOURCE_ID	ALPHA	<i>p.l.x</i>	distance							
(1)	(2)	(3)	(4)	(5)	(6)	(7)	(8)	(9)	(10)	(11)	(12)	(13)	(12)	(13)							
	($^{\circ}$)	($^{\circ}$)	(mag)	(mag)	(mag)	(mag)	(mag)	(mag)	(mag)	(mag)	(mag)	(mag)	mas	kpc							
J043252.89+511147.9	153.9931	2.1973	12.882	± 0.024	12.158	± 0.023	10.177	± 0.068	8.338	14.728	± 0.044	13.846	± 0.030	13.249	± 0.039	svmgaia	271001136322616576	-1.142	0.316	3.2	
J043356.97+503841.3	154.5128	1.9461	13.162	± 0.025	12.331	± 0.024	9.397	± 0.040	8.155	± 0.272	15.612	± 0.056	14.706	± 0.064	14.032	± 0.050	svmgaia	258916369662466944	-0.198	0.180	5.6
J043526.26+520059.8	153.6582	3.0447	10.065	± 0.022	9.016	± 0.019	6.899	± 0.019	4.258	± 0.026	14.892	± 0.050	13.307	± 0.042	12.331	± 0.027	svmgaia	272561339025907328	-0.024	0.188	5.3
J043722.95+504519.0	154.7977	2.4222	12.415	± 0.025	12.048	± 0.024	10.619	± 0.089	8.206	± 0.275	14.405	± 0.033	13.523	± 0.037	13.072	± 0.028	svmgaia	25884891843742464	-1.467	0.276	3.6
J043754.76+505030.2	154.7543	2.5032	12.040	± 0.022	8.594	± 0.033	6.238	± 0.066	14.821	± 0.034	13.706	± 0.033	12.979	± 0.028	15.779	± 0.028	svmgaia	258886541111382784	-0.312	0.176	5.7
J044044.00+502701.3	155.3797	2.6161	12.213	± 0.027	11.798	± 0.025	9.385	4.962	± 0.083	15.068	± 0.036	14.229	± 0.046	13.496	± 0.032	svmgaia	260166991123413248	0.129	0.214	4.7	
J043343.59+504339.4	154.4280	1.9763	15.732	± 0.046	16.143	± 0.188	11.764	± 0.253	8.547	16.946	± 0.181	16.088	± 0.187	15.677	± 0.228	svmgaia	258920694691048960	-0.631	0.278	3.6	
J043454.84+504520.6	154.5346	2.1336	15.837	± 0.055	16.473	11.232	± 0.214	8.618	16.532	± 0.132	15.943	± 0.172	15.735	± 0.167	15.545	svmgaia	258939901784863872	0.149	0.218	4.6	
J043517.83+502602.8	154.8131	1.9613	15.800	± 0.064	15.866	± 0.178	12.529	7.304	± 0.137	16.655	± 0.123	15.974	± 0.161	15.545	svmgaia	25887393647358336	1.265	0.315	3.2		
J043557.01+501445.7	154.9864	1.8721	15.284	± 0.041	15.471	± 0.113	12.653	8.959	± 0.445	16.356	± 0.115	15.778	± 0.135	15.427	± 0.167	svmgaia	258856923018080768	-1.237	0.297	3.4	
J043643.55+505640.4	154.5876	2.4722	13.863	± 0.031	13.770	± 0.043	9.787	± 0.076	7.636	± 0.244	14.764	± 0.034	14.303	± 0.050	14.142	± 0.058	svmgaia	25893856053330688	-0.473	0.240	4.2
J043700.49+510430.1	154.5206	2.5927	15.511	± 0.046	15.487	± 0.112	11.506	± 0.229	8.675	± 0.386	16.557	± 0.122	15.616	± 0.128	15.367	± 0.168	svmgaia	258951309218508032	-0.430	0.240	4.2
J043704.64+510143.0	154.5624	2.5696	15.191	± 0.041	15.814	± 0.153	11.591	± 0.235	8.708	± 0.515	16.180	± 0.085	15.652	± 0.137	15.321	± 0.161	svmgaia	25890965621090688	-0.739	0.214	4.7
J043705.51+504133.8	154.8134	2.3461	15.724	± 0.053	16.169	± 0.198	11.309	± 0.174	8.724	± 0.459	16.737	± 0.146	15.836	± 0.158	15.587	± 0.188	svmgaia	258883173856673280	0.006	0.304	3.3
J043728.59+495336.1	155.4483	1.8561	15.123	± 0.037	15.330	± 0.098	12.482	± 0.517	8.554	± 0.349	16.087	± 0.074	15.344	± 0.098	15.027	± 0.111	svmgaia	25864378960987520	-1.299	0.279	3.6
J043749.33+501442.7	155.2239	2.1328	15.382	± 0.042	15.761	± 0.140	10.714	± 0.128	7.801	± 0.220	16.677	± 0.149	15.813	± 0.143	15.475	svmgaia	258668794731758464	0.634	0.267	3.7	
J043816.09+502509.6	155.1418	2.3022	15.373	± 0.042	15.482	± 0.107	11.174	± 0.168	8.699	± 0.383	16.252	± 0.100	15.720	± 0.133	15.374	± 0.163	svmgaia	258675228719310848	-0.242	0.269	3.7
J043817.02+500632.1	155.3748	2.0967	15.263	± 0.041	15.381	± 0.105	11.967	± 0.320	8.854	16.388	± 0.138	15.594	± 0.123	15.501	± 0.181	svmgaia	258654509799884032	-1.549	0.311	3.2	
J043952.11+510911.7	154.7620	2.9793	14.844	± 0.039	15.025	± 0.082	12.103	7.212	± 0.132	15.715	± 0.072	15.163	± 0.083	14.807	± 0.093	svmgaia	260398747557713536	0.197	0.272	3.7	
J044000.87+510936.9	154.7719	3.0011	15.740	± 0.037	11.463	± 0.045	7.667	± 0.144	3.052	± 0.026	13.586	± 0.043	12.689	± 0.043	12.412	± 0.039	svmgaia	260398644478512256	-1.527	0.293	3.4
J044015.74+503029.3	155.2867	2.5982	15.421	± 0.051	16.308	10.401	± 0.094	8.424	16.885	± 0.171	15.955	± 0.186	16.021	± 0.281	15.824	svmgaia	260179738585855360	0.792	0.264	3.8	
J044051.48+502738.6	155.3500	2.5981	11.618	± 0.031	13.469	± 0.035	9.212	± 0.037	7.441	± 0.152	14.421	± 0.039	14.073	± 0.056	13.920	± 0.059	svmgaia	260166926701879680	1.098	0.251	4.0
J044056.97+503052.5	155.3543	2.6843	13.824	± 0.031	14.101	± 0.057	9.770	± 0.071	7.915	± 0.483	15.463	± 0.050	14.610	± 0.056	14.307	± 0.045	svmgaia	260167506519018624	-0.524	0.283	3.5
J044101.42+495150.1	155.8506	2.2633	13.669	± 0.031	13.469	± 0.035	9.212	± 0.037	7.441	± 0.152	14.421	± 0.039	14.073	± 0.056	13.920	± 0.059	svmgaia	260085631561486976	0.184	0.269	3.7
J044134.45+511832.3	154.8217	3.2826	15.356	± 0.043	15.379	± 0.098	12.111	± 0.305	9.042	16.656	± 0.154	15.881	± 0.175	15.464	± 0.167	svmgaia	260423898884400640	-1.583	0.301	3.3	
J044215.18+492259.5	156.3438	2.0957	11.772	± 0.023	11.206	± 0.021	9.966	± 0.057	8.478	13.614	± 0.028	13.057	± 0.030	12.515	± 0.024	svmgaia	259260138847597952	-1.328	0.176	5.7	
J043326.34+504330.2	154.3990	1.9412	9.667	± 0.021	8.928	± 0.019	4.123	± 0.014	1.758	± 0.016	14.536	± 0.121	13.820	± 0.110	13.085	± 0.114	SVMClass/II			1.193	
J043327.68+503956.2	154.4450	1.9034	12.780	± 0.032	11.675	± 0.023	8.959	± 0.028	6.432	± 0.057	17.124	± 0.206	15.963	± 0.166	14.982	± 0.116	Class I			0.071	
J043405.39+511024.6	154.4389	3.2028	14.518	± 0.035	14.053	± 0.045	11.939	± 0.273	8.790	± 0.509	16.635	± 0.142	15.637	± 0.129	15.161	± 0.127	svmgaia	270974159631952128	-1.115		
J043543.73+520129.5	153.6823	3.0834	9.106	± 0.022	7.581	± 0.021	4.540	± 0.015	1.876	± 0.018	15.302	± 0.092	13.225	± 0.050	11.269	± 0.028	Class I			0.653	
J043547.75+501107.0	155.0506	1.8523	12.784	± 0.025	12.017	± 0.022	9.802	± 0.050	7.981	± 0.228	16.361	± 0.099	14.905	± 0.065	14.022	± 0.048	Class II			-0.547	
J043555.05+510435.1	154.4043	2.4667	15.347	± 0.045	15.376	± 0.107	11.509	± 0.443	8.328	± 0.309	16.620	± 0.130	15.705	± 0.137	15.297	svmgaia	258953920558623872	0.024			
J043556.56+510557.7	154.3900	2.4851	15.086	± 0.074	13.023	± 0.033	8.748	± 0.056	6.153	± 0.076						Class I			1.329		
J043600.40+505727.6	154.5159	2.4127	11.975	± 0.024	10.534	± 0.021	6.967	± 0.016	4.217	± 0.023	16.788	± 0.191	15.400	± 0.127	14.135	± 0.079	Class I			0.846	
J043615.46+511338.8	154.3284	2.6077	13.869	± 0.026	13.611	± 0.032	8.785	± 0.025	4.032	± 0.028	15.584	± 0.062	14.874	± 0.062	14.511	± 0.089	SVMClass/II			1.783	
J043615.56+511357.2	154.3248	2.6114	14.727	± 0.034	14.758	± 0.064	9.036	± 0.033	6.512	± 0.114	16.019	± 0.085	15.144	± 0.091	15.177	± 0.129	SVMClass/II			1.317	
J043619.44+510635.6	154.4225	2.5364	11.900	± 0.023	10.695	± 0.021	8.773	± 0.032	6.518	± 0.081	18.119	± 0.249	13.843	± 0.049	13.843	± 0.049	Class II			-0.177	
J043619.99+511400.2	154.3320	2.6205	12.692	± 0.025	12.244	± 0.023	7.988	± 0.025	3.939	± 0.033	15.889	± 0.069	14.324	± 0.048	13.679	± 0.042	svmgaia	270967081525874048	1.095		
J043620.88+511222.4	154.3537	2.6040	8.8																		

Table 9 (continued)

allwise	l	b	$W1$ (3.4 μm)	$W2$ (4.6 μm)	$W3$ (12 μm)	$W4$ (22 μm)	J (1.25 μm)	H (1.65 μm)	K_s (2.16 μm)	FROM \hat{d}	GAIA_SOURCE_ID	ALPHA	pl_x	distance					
	($^{\circ}$)	($^{\circ}$)	(mag)	(mag)	(mag)	(mag)	(mag)	(mag)	(mag)	(mag)	(11)	(12)	(13)	(13)					
	(1)	(2)	(3)	(4)	(5)	(6)	(7)	(8)	(9)	(10)	(11)	(12)	(13)	(13)					
J043623.17+511404.8	154.3366	2.6275	13.554	± 0.026	13.041	± 0.028	8.236	± 0.024	4.541	± 0.033	15.320	± 0.061	14.646	± 0.072	14.606	± 0.104	SVMClass/II	1.495	
J043623.59+511223.1	154.3583	2.6093	12.423	± 0.021	11.348	± 0.017	6.568	± 0.015	2.333	± 0.012	16.500	± 0.118	14.853	± 0.073	14.144	± 0.062	SVMClass/II	2.124	
J043629.12+510412.7	154.4690	2.5285	10.821	± 0.023	9.961	± 0.021	8.079	± 0.026	6.378	± 0.073	15.710	± 0.076	13.714	± 0.038	12.279	± 0.026	svmgaia	258954779553725824	-0.601
J043631.8+511220.1	154.3734	2.6248	12.531	± 0.023	11.808	± 0.022	10.000	± 0.066	5.186	± 0.056	16.984	± 0.190	14.848	± 0.084	13.806	± 0.043	ClassI	0.233	
J043632.11+511353.4	154.3546	2.6426	11.042	± 0.023	9.697	± 0.019	6.984	± 0.017	4.757	± 0.029	16.587	± 0.135	14.138	± 0.048	12.573	± 0.025	ClassI	0.151	
J043635.21+505205.3	154.6296	2.4047	12.892	± 0.029	12.532	± 0.030	7.938	± 0.020	5.112	± 0.035	15.848	± 0.070	14.335	± 0.056	13.834	± 0.043	SVMClass/II	0.840	
J043639.99+505841.0	154.5565	2.4878	12.969	± 0.025	11.638	± 0.022	9.084	± 0.040	6.543	± 0.070	17.626	15.841	14.883	± 0.103	ClassI	0.114			
J043642.72+505436.7	154.6117	2.4475	13.133	± 0.037	12.432	± 0.031	7.721	± 0.024	5.384	± 0.048	15.643	± 0.061	14.639	± 0.062	14.500	± 0.081	SVMClass/II	1.138	
J043642.82+505142.3	154.6478	2.4152	11.996	± 0.031	11.529	± 0.027	6.108	± 0.018	3.140	± 0.030	15.717	± 0.054	14.813	± 0.071	14.624	± 0.079	SVMClass/II	1.751	
J043645.28+505116.6	154.6574	2.4152	12.422	± 0.025	12.182	± 0.027	7.139	± 0.020	3.888	± 0.028	16.310	± 0.100	15.030	± 0.123	14.780	± 0.094	SVMClass/II	1.440	
J043649.54+505242.8	154.6472	2.4396	9.599	± 0.029	9.374	± 0.036	6.563	± 0.098	6.688	± 0.024	10.755	± 0.038	10.343	± 0.042	10.076	± 0.036	SVMClass/II	1.197	
J043650.47+505421.4	154.6285	2.4598	12.347	± 0.026	11.780	± 0.024	6.779	± 0.017	4.314	± 0.032	16.229	± 0.086	15.130	± 0.074	14.251	± 0.052	SVMClass/II	1.313	
J043658.60+505047.6	154.6869	2.4358	12.726	± 0.026	12.400	± 0.026	12.012	7.285	± 0.125	13.938	± 0.032	13.391	± 0.031	13.198	± 0.032	svmgaia	258933961848686720	-1.196	
J043707.18+510255.1	154.5519	2.5880	14.705	± 0.036	14.787	± 0.066	11.418	± 0.220	8.670	± 0.134	15.800	± 0.155	15.091	± 0.132	svmgaia	258951034342246400	-1.491		
J043712.87+504643.8	154.7624	2.4183	13.503	± 0.028	11.451	± 0.022	8.905	± 0.037	4.579	± 0.032	15.942	± 0.077	15.224	± 0.098	15.228	± 0.160	SVMClass/II	1.104	
J043718.27+504745.3	154.7593	2.4403	11.514	± 0.023	10.372	± 0.021	9.031	± 0.036	7.006	± 0.101	16.821	± 0.156	14.654	± 0.069	13.148	± 0.045	SVMClass/II	-0.650	
J043721.46+512007.2	154.3638	2.8077	11.870	± 0.023	10.464	± 0.021	7.632	± 0.019	5.126	± 0.034	17.236	± 0.232	15.244	± 0.097	13.683	± 0.035	ClassI	0.316	
J043721.62+511701.6	154.4024	2.7735	14.655	± 0.034	14.813	± 0.073	10.585	± 0.084	7.608	± 0.142	16.000	± 0.079	15.317	± 0.092	14.910	± 0.118	svmgaia	260458430423463424	0.136
J043722.68+510503.0	154.5528	2.6419	11.460	± 0.021	10.662	± 0.018	8.244	± 0.022	5.692	± 0.038	15.242	± 0.058	14.164	± 0.067	13.095	± 0.051	SVMClass/II	-0.221	
J043725.71+511641.0	154.4138	2.7776	12.516	± 0.029	11.592	± 0.025	7.101	± 0.015	4.439	± 0.025	14.934	± 0.048	14.189	± 0.059	13.806	± 0.066	SVMClass/II	1.144	
J043727.34+504356.3	154.8226	2.4154	12.451	± 0.037	11.109	± 0.024	8.658	± 0.030	5.969	± 0.050	16.756	± 0.151	15.120	± 0.091	14.101	± 0.054	ClassI	0.081	
J043728.18+511423.2	154.4466	2.7567	12.199	± 0.023	12.124	± 0.023	11.080	± 0.170	6.915	± 0.097	13.485	± 0.029	12.729	± 0.032	12.441	± 0.029	svmgaia	260457335208452096	-1.462
J043728.90+504524.8	154.7609	2.4684	13.299	± 0.026	12.338	± 0.025	9.596	± 0.052	8.125	± 0.269	16.339	± 0.107	15.276	± 0.085	14.492	± 0.077	SVMClass/II	258886334954881664	-0.134
J043729.45+511825.5	154.4607	2.7484	12.897	± 0.025	11.370	± 0.022	8.583	± 0.025	5.456	± 0.038	18.582	± 15.883	± 0.177	14.782	± 0.109	ClassI	0.480		
J043729.45+510934.5	154.5085	2.7055	13.095	± 0.024	12.089	± 0.023	9.620	± 0.046	7.526	± 0.164	16.918	± 0.187	15.477	± 0.108	14.564	± 0.091	SVMClass/II	-0.220	
J043730.89+511303.8	154.4678	2.7472	12.968	± 0.025	12.170	± 0.023	10.311	± 0.082	7.322	± 0.148	16.970	± 0.189	15.196	± 0.102	14.113	± 0.069	ClassII	-0.535	
J043732.59+504945.2	154.7597	2.4905	11.858	± 0.023	10.437	± 0.020	8.351	± 0.026	5.856	± 0.052	17.817	± 15.775	± 0.168	14.262	± 0.078	ClassI	-0.167		
J043732.95+511134.2	154.4899	2.7346	12.953	± 0.024	11.618	± 0.021	9.183	± 0.032	6.786	± 0.090	17.938	± 15.409	14.680	± 0.091	ClassI	-0.042			
J043753.28+504449.7	154.8220	2.4370	11.442	± 0.024	9.793	± 0.020	7.367	± 0.018	4.471	± 0.029	17.020	± 15.258	± 0.100	13.644	± 0.043	ClassI	0.322		
J043754.73+511839.1	154.4244	2.8383	12.935	± 0.025	12.030	± 0.024	9.596	± 0.044	7.068	± 0.108	17.857	± 15.412	± 0.117	14.288	± 0.063	ClassII	-0.246		
J043745.91+495141.3	155.5032	1.8694	13.083	± 0.024	11.919	± 0.021	7.921	± 0.018	4.463	± 0.025	16.006	± 0.097	14.729	± 0.091	13.948	± 0.065	ClassI	1.176	
J043746.66+501148.0	155.2552	2.0951	14.600	± 0.033	14.699	± 0.059	11.627	± 0.262	8.832	± 0.441	16.205	± 0.108	15.357	± 0.088	14.993	± 0.123	svmgaia	258667978817459584	-1.483
J043748.97+500740.2	155.3106	2.0536	12.575	± 0.024	11.257	± 0.022	8.263	± 0.023	5.595	± 0.036	16.352	± 0.131	15.134	± 0.095	14.049	± 0.060	ClassI	0.384	
J043800.32+511819.5	154.4538	2.8629	12.988	± 0.026	11.722	± 0.023	9.097	± 0.033	6.539	± 0.071	17.970	± 16.574	15.075	± 0.135	ClassI	0.083			
J043808.79+505744.8	154.7243	2.6504	12.189	± 0.026	10.372	± 0.020	7.121	± 0.019	4.408	± 0.033	16.981	± 16.038	14.646	± 0.086	ClassI	0.759			
J043820.98+505934.8	154.7228	2.6946	12.026	± 0.023	11.255	± 0.020	9.077	± 0.037	6.546	± 0.079	15.394	± 14.383	± 0.071	13.332	± 0.045	ClassII	-0.455		
J043857.55+502517.0	155.2138	2.3855	12.833	± 0.030	11.620	± 0.025	8.641	± 0.031	6.244	± 0.089	16.769	± 16.108	± 0.234	14.965	± 0.134	ClassI	0.257		
J043859.57+504541.1	154.9634	2.6159	12.897	± 0.025	12.136	± 0.025	10.911	± 0.125	8.486	± 16.535	± 0.167	15.039	± 0.106	13.913	± 0.061	ClassII	-0.898		
J043909.62+510341.1	154.7567	2.8353	12.520	± 0.027	11.735	± 0.025	8.386	± 0.026	5.821	± 0.048	15.524	± 0.065	14.455	± 0.059	13.728	± 0.042	svmgaia	260396548534294400	0.267
J043919.89+501558.9	155.3690	3.3266	14.317	± 0.029	13.761	± 0.034	11.085	± 0.345	8.617	± 16.599	± 0.152	15.659	± 0.141	14.984	± 0.120	svmgaia	260158091951714176	-1.238	
J043927.41+513944.6	154.3379	3.2692	13.050	± 0.025	12.122	± 0.023	10.557	± 0.058	7.828	± 0.174	16.770	± 0.158	15.294	± 0.105	14.341	± 0.070	svmgaia	273479734648021248	-0.482
J043928.46+513913.6	154.3461	3.2656	11.592	± 0.023	10.591	± 0.022	7.962	± 0.020	5.847	± 0.038	16.734	± 0.148	14.631	± 0.054	13.306	± 0.029	ClassII	-0.027	
J043935.07+501122.5	155.4535	3.3059	14.279																

Table 9 (continued)

allwise	l	b	$W1$ (3.4 μm)	$W2$ (4.6 μm)	$W3$ (12 μm)	$W4$ (22 μm)	J (1.25 μm)	H (1.65 μm)	K_s (2.16 μm)	FROM \hat{d}	GAIA_SOURCE_ID ALPHA	pl_x distance
	($^{\circ}$)	($^{\circ}$)	(mag)	(mag)	(mag)	(mag)	(mag)	(mag)	(mag)	(11)	(12)	(13)
(1)	(2)	(3)	(4)	(5)	(6)	(7)	(8)	(9)	(10)	(11)	(12)	(13)
J044012.96+492359.5	156.1122	1.8579	12.715 \pm 0.025	12.332 \pm 0.025	9.870 \pm 0.051	7.588 \pm 0.176	14.501 \pm 0.032	13.628 \pm 0.043	13.183 \pm 0.031	svmgaia	257812116391866112	-1.056
J044014.20+502319.4	155.3736	2.5160	12.637 \pm 0.035	12.681 \pm 0.043	10.098 \pm 0.085	7.269 \pm 0.184	13.070 \pm 0.028	12.935 \pm 0.032	12.782 \pm 0.029	svmgaia	260160604510068480	-1.552
J044027.19+502828.8	155.3320	2.5987	8.664 \pm 0.020	7.854 \pm 0.020	2.230 \pm 0.016	-1.944 \pm 0.002	13.280 \pm 0.051	12.238 \pm 0.050	11.469 \pm 0.052	SVMClass/II		2.557
J044029.19+502736.3	155.3464	2.5931	11.635 \pm 0.027	11.409 \pm 0.034	6.099 \pm 0.031	3.181 \pm 0.035	17.039 \pm 0.199	15.265 \pm 0.102	14.509 \pm 0.091	SVMClass/II		1.446
J044035.03+502710.5	155.3621	2.5999	11.543 \pm 0.024	11.234 \pm 0.023	5.828 \pm 0.026	1.791 \pm 0.023	15.685 \pm 0.078	14.918 \pm 0.079	14.766 \pm 0.104	SVMClass/II		2.088
J044037.27+502740.7	155.3597	2.6099	9.654 \pm 0.022	9.469 \pm 0.021	6.517 \pm 0.024	2.351 \pm 0.049	10.380 \pm 0.024	10.205 \pm 0.030	10.059 \pm 0.021	SVMClassIII		-0.421
J044040.84+502738.5	155.3664	2.6166	10.146 \pm 0.023	10.019 \pm 0.023	5.944 \pm 0.019	2.446 \pm 0.053	11.850 \pm 0.023	11.154 \pm 0.030	10.963 \pm 0.024	SVMClassIII		0.235
J044053.59+502711.6	155.3944	2.6371	10.936 \pm 0.032	11.019 \pm 0.034	6.108 \pm 0.030	4.137 \pm 0.059	12.524 \pm 0.024	11.852 \pm 0.028	11.644 \pm 0.024	SVMClassIII		0.212
J044104.67+502931.3	155.3847	2.6847	12.283 \pm 0.024	11.794 \pm 0.026	7.145 \pm 0.020	5.310 \pm 0.042	14.045 \pm 0.029	13.582 \pm 0.043	13.316 \pm 0.040	SVMClass/II		0.744
J044119.36+502234.7	155.4975	2.6376	11.532 \pm 0.023	10.915 \pm 0.022	7.534 \pm 0.023	4.460 \pm 0.028	12.915 \pm 0.026	12.681 \pm 0.033	12.517 \pm 0.028	SVMClass/II		0.323
J044404.38+502005.2	155.8173	2.9412	12.232 \pm 0.023	11.316 \pm 0.021	8.986 \pm 0.031	6.189 \pm 0.049	16.372 \pm 0.110	14.749 \pm 0.074	13.771 \pm 0.053	ClassII		-0.153
J044405.47+501745.2	155.8487	2.9180	11.414 \pm 0.022	10.566 \pm 0.019	8.316 \pm 0.024	6.066 \pm 0.052	14.966 \pm 0.045	13.679 \pm 0.054	12.871 \pm 0.037	ClassII		-0.388
J044442.25+494014.9	156.3872	2.5846	12.614 \pm 0.023	11.613 \pm 0.021	9.876 \pm 0.050	6.867 \pm 0.091	16.098 \pm 0.136	15.218 \pm 0.136	13.702	ClassII		-0.509

⁶ The marks of Class*, svmgaia, and SVMClass* indicate the candidate YSOs identified through the scheme of Koenig & Leisawitz (2014) and obtained from Marton et al. (2016), and Marton et al. (2019), respectively.